UNIVERSITY OF TWENTE.

Radboudumc

Evaluation of options to improve accurate execution of osteotomies of the lower limb

Anne R.D. Rook

Master Thesis
September 1, 2022

Chair of the committee:
Prof. dr. J.J. Fütterer
Technical supervisor UT:
dr. ir. A. Q. L. Keemink
Medical supervisor Radboudumc:
dr.ing. S.A.W. van de Groes
Daily supervisor Radboudumc:
ir. H. Dunning
Process supervisor UT:
E.M. Walter MSc
External member UT:
dr. F.J. Siepel

Science and Technology - Robotics and Mechatronics
University of Twente
Engineering Technology - Biomechanical Engineering

Department of Orthopedics
Radboudumc, Nijmegen

Document number: 041RaM2022

Preface

Voor u ligt mijn afstudeerverslag 'Evaluation of options to improve the accurate execution of osteotomies of the lower limb' voor de masters van Technische Geneeskunde en Biomedical Engineering. Juist het combineren van beide studies tot één afstudeeropdracht gaf mij de mogelijkheid om dieper op dit onderwerp in te gaan en verschillende kanten te kunnen te onderzoeken. Hiervoor heb ik anderhalf jaar stage gelopen bij de afdeling Orthopedie en het Orthopaedic Research Lab in het Radboudumc in Nijmegen.

Toen ik in 2014 in Enschede begon met Technische Geneeskunde had ik niet voor mogelijk gehouden dat ik in 2022 nog steeds aan het studeren zou zijn. Ondanks dat ik de stages tijdens de masterperiode erg leuk vond, had ik toch het gevoel dat ik iets miste. Ik wilde graag meer leren over de toepassing van robotica in de medische sector. Daarom ben ik in 2019 ook begonnen met de Roboticamaster van Biomedical Engineering en dat beviel mij erg goed.

In de afgelopen 8 jaar heb ik veel nieuwe dingen geleerd, niet alleen over technisch-medisch inhoudelijke dingen, maar ook over mezelf als persoon. Tijdens ben ik er beter achter gekomen waar mijn kwaliteiten liggen en wat ik leuk vind om te doen. Ik kijk terug op een waardevolle periode waarin ik veel mooie dingen heb mogen doen.

Gelukkig heb ik dit niet allemaal alleen hoeven doen. Ik wil iedereen bedanken die mij heeft ondersteund tijdens mijn afstudeerperiode. In het bijzonder wil ik mijn supervisoren bedanken voor voor hun hulp tijdens mijn afstuderen. Bedankt dat jullie altijd de tijd namen om al mijn vragen te beantwoorden en vragen stelden om mij aan het nadenken te zetten. Daarnaast wil ik de mensen van de afdeling Orthopedie en het Orthopaedic Research Lab bedanken voor jullie hulp, en vooral voor de leuke tijd die ik heb gehad op de afdeling. Tot slot wil ik mijn vrienden en familie bedanken voor jullie support en onvoorwaardelijke steun waardoor ik deze studies heb kunnen afronden.

Abstract

Accuracy and precision are important when executing a corrective osteotomy around the knee. However, it can be difficult to achieve a high accuracy without additional tools. Therefore, the aim of this thesis was twofold. The first aim was to map the corrective osteotomy procedure and to identify surgical challenges and needs of an orthopedic surgeon to overcome these challenges in clinical practice. The second aim was to research the feasibility of using Ultrasound (US) to estimate the bone pose during surgery. A corrective osteotomy around the knee was used as a case study here.

First, interviews among orthopedic surgeons were held to gain insight into the difficulties and challenges they experience when executing a corrective osteotomy around the knee or when using additional tools to perform surgery more accurately. These interviews showed that variation exist among surgeons regarding the leg stance that is aimed for, the execution procedure of a correction osteotomy around the knee and the importance of a surgical plan within this process. Hence, it was decided to focus on improving the registration procedure (which is the alignment of a surgical plan to the anatomy of a patient) to make a preoperative plan more easily available and usable within the operation room. A trade-off was made between different registration techniques. It was decided to further investigate the possibility of using US as a registration technique in a surgical setting.

Therefore, first computer simulations that mimicked the registration procedure were performed to evaluate whether either A-mode or a combination of A- and B-mode US sensors should be used. Different Monte-Carlo simulations using a sensor model to mimic realistic US measurements were performed to determine the number of sensors that were needed to obtain a desired accuracy of 1 mm and 1°, and to determine the effect of the sensor positioning and measurement inaccuracy on the registration accuracy.

Second, an experiment was conducted to determine how accurate US could detect the bone surface. Therefore, US images of a cadaver were made inside a CT scanner to acquire simultaneous imaging of both US and CT (ground truth). In total, the bone localization error between CT and US was determined in 11 static measurements made on a human femoral bone cadaver.

The simulation findings suggested that at least 22 A-modes or 6 A-modes and 7 B-modes were needed to obtain a registration accuracy of 1 mm and 1°. A combination of A- and B-mode sensors was more robust to measurement inaccuracy compared to using only A-mode sensors. Still, all US measurements depended heavily on the amount of measurement inaccuracy present in the data. Verification of the bone localization error via an experiment revealed that the mean absolute difference in bone surface depth between CT and US was -0.47 $\pm$ 0.90 mm. This accuracy was within the voxel range of the CT scan. When repeating the Monte Carlo simulation with this B-mode inaccuracy level, the registration accuracy worsened: using 6 A-modes and 7 B-modes resulted in a registration accuracy of around 4 mm and 4°.

This thesis shows that theoretically, it is possible to use US as a bone localization tool to align a surgical plan with the anatomy of the patient, although the number of sensors that are needed to obtain the set accuracy of 1 mm and 1° is not clinically feasible yet. This thesis provides the next step towards an accurate execution of a surgical plan within orthopedics, providing

more predictable outcomes in the future. For the application of US as a registration technique in clinical practice for corrective osteotomies, the usability of this system as a whole should be tested in a surgical setting. Indeed, the interviews showed good usability is one of the most important factors in the adoption of this technique in clinical practice. Before that time, first, some technical aspects of this system should be improved to increase its accuracy. Therefore, more research regarding a more sufficient registration algorithm, accurate, real-time, automatic bone detection in US images, and US sensor positioning and localization should be performed. With this information, a predictive sensor model can be made more realistic by identifying the magnitude of the different sources of inaccuracy more accurately, and by evaluating the effect of combining multiple sources of errors.

Table of Contents

Acronyms

CORA Center Of Rotation of Angulation

GSP Geometric Shape Preservation

HKA Hip-Knee-Ankle

ICP Iterative Closest Point

KNN K-nearest neighbor

MAD Mechanical Axis Deviation

PST Patient-Specific Templates

RMSE Root Mean Square Error

TRE Target Registration Error

US Ultrasound

Part I

General introduction

Chapter 1

Introduction

Performing orthopedic surgery by following a surgical plan can be of added value within orthopedic surgery but is often not used in everyday practice. This chapter discusses the added value of such a surgical plan and the challenges orthopedic surgeons face when using supporting tools to execute a surgical plan more accurately. A corrective osteotomy around the knee is used as a case study here to discuss this topic.

1.1 Surgical planning within orthopedic surgery

Nowadays, a preoperative surgical plan becomes increasingly important in orthopedic surgery. This precise surgical plan is often a three-dimensional visualization of the intended bone positioning and configuration obtained after surgery. The plan defines the surgical steps needed to obtain the planned bone repositioning and configuration [1]. It provides the orthopedic surgeon with a good understanding of the patient's anatomy. This empowers the surgeon to prepare for the surgery with the necessary equipment, and, through that, avoid possible postoperative complications [2]–[5]. Moreover, the development of supportive tools such as robotic tools to execute surgery more accurately require a precise surgical plan. Using these tools for a more predictable result is expected to become increasingly important in future surgery [6]. The application of these technologies starts with an accurate surgical plan.

Linking this plan to the anatomy of the patient perioperatively is crucial for using a surgical plan in the operation room [7]. Often, imaging modalities such as X-ray, CT scans, or ultrasound imaging in combination with navigation tools are used for this coupling. For example, navigation technologies have been developed for spinal [8], knee [9], and hip surgery [10]. Overall, studies evaluating these technologies show that a surgical plan contributes to a more accurate execution and more predictable surgical results [3], [4]. Especially in complex orthopedic surgeries, tools that support executing a surgical plan accurately are needed for proper execution [11].

A corrective osteotomy around the knee is an example of a surgery that may be complex to execute. Without computer-assisted tools, this procedure can be considered difficult and high risk, discouraging surgeons to perform a corrective osteotomy [12]. A precise surgical plan can be helpful to execute these corrective osteotomies.

To understand why lower limb malalignment causes problems, especially in the knee joint, the anatomy of the knee is explained in the next subsection.

1.1.1 Anatomy of the knee

The osseous parts of the knee are the femur, tibia, and patella. The distal part of the femur exists of the medial and the lateral condyle, which shape fits into the proximal end of the tibia.

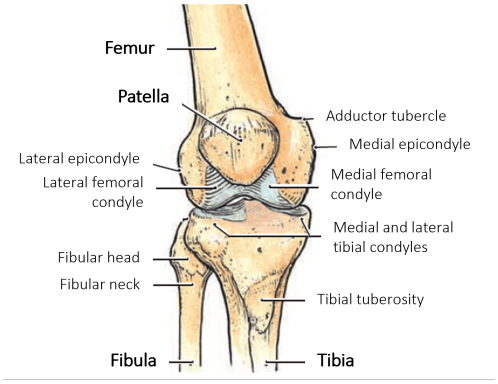

Figure 1.1: Bones of the knee in bold, with characteristic bony landmarks. Adapted from [13].

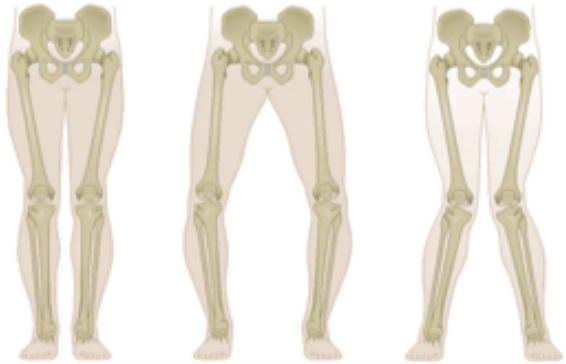

Figure 1.2: Schematic overview of a normal lower limb alignment (left), varus malalignment (middle), and valgus malalignment (right) [19].

The tibia is a relatively flat articular surface with a tibial spine located in the middle; the intercondylar notch of the femur fits into this spine and provides bony stability. The menisci on the tibial plateau are oval-shaped such that the femoral condyles fit better into the tibial plateau. These femoral condyles articulate with the menisci and tibial condyles: during flexion, the menisci and tibial condyles glide towards the posterior side of the femoral condyles, during extension this movement is reversed. The hyaline cartilage on the trochlea provides a smooth joint surface. The menisci contain predominantly collagen type I ordered in a compact network, to resist push- and pull forces while providing damping [13]–[16]. A schematic overview of the knee joint is given in Figure 1.1.

All bones have a dense outer layer called the cortical or compact bone, covered by the periosteum. This layer forms the hard cortex of the bone. Deeper inside the bone, the structure is more open and porous, this is the trabecular or cancellous bone. The trabeculae are aligned such that they can withstand the mechanical load applied to the bone [16].

1.2 Lower limb malalignment

A corrective osteotomy may be needed in patients in case of lower limb malalignment, which is a deformity in the lower limb. This malalignment can be congenital, caused by trauma, or degenerative. In general, three groups of malalignment are differentiated: varus, valgus, and rotational malalignment (see Figure 1.2). Being bow-legged (called genu varum or varus alignment) in the frontal plane is more common compared to being knock-kneed (called genu valgum or valgus alignment) [17]. Most patients having a lower limb deformity experience pain during walking and have a feeling of instability in their knee. This is because the malalignment affects proper articulation of the femoral condyles with the menisci and tibial condyles and proper tracking of the patella during flexion and extension. The forces through the knee are imbalanced, therefore one side of the knee can become overloaded. In addition, adjacent ligaments and muscles can become affected, which influences the knee motion and stability. As a result, these patients have a higher risk of developing osteoarthrosis in their knee joints [18]. Moreover, due to an affected gait pattern, a patient may experience pain in other areas such as the ankle, the hip, or the lower back.

The gold standard for determining varus or valgus lower limb alignment that is often used in clinical practice is determining the Hip-Knee-Ankle (HKA) in a weight-bearing whole leg radiograph [20]. The HKA angle is the angle between the mechanical axes of the femur and the tibia. As a rule of thumb, a varus alignment between 1 and 3° (HKA angle of 177–189°) is considered normal. A valgus alignment or varus alignment greater than 3° is considered

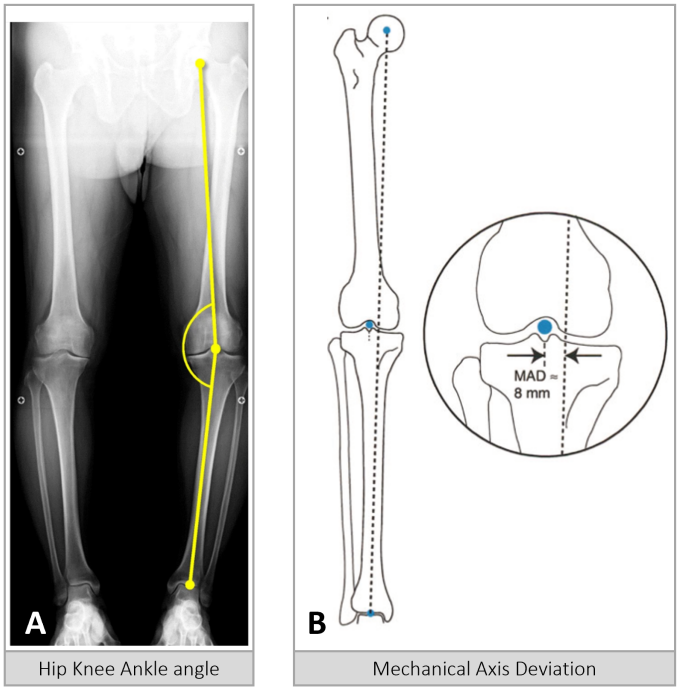

Figure 1.3: A) Mechanical axes of the femur and tibia between which the HKA angle is calculated [23]. **B)** Mechanical axis of the lower limb, with the center of the knee joint indicated with a black dot. With these two measures, the MAD can be determined, for example indicating whether the leg has a varus [21].

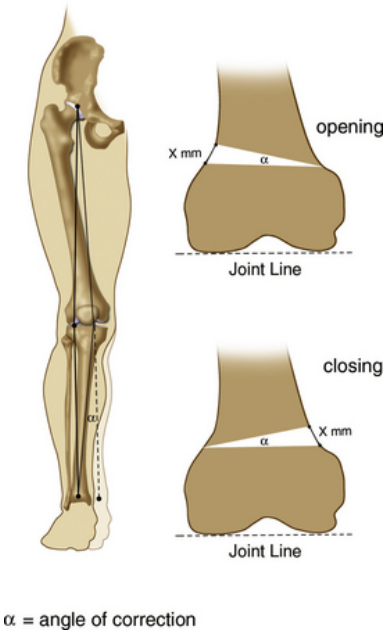

Figure 1.4: Schematic image of a distal femoral osteotomy. Here, the angle α indicates the amount of correction that is calculated to correct the mechanical axis of the lower limb [24].

pathological [21]. The left image of Figure 1.3 shows a weight-bearing whole leg radiograph where the HKA is determined as well.

Another option to evaluate the knee alignment is using the Mechanical Axis Deviation (MAD), which is the perpendicular distance between the mechanical axis of the lower limb and the center of the knee joint. If the mechanical axis is laterally (meaning the MAD ≥ 0 mm) or too medially (such that MAD$\geq$15 mm) located from the center of the knee, it is considered to be valgus or varus, respectively. The calculation of the MAD on a weight-bearing whole leg radiograph is shown at the right sight of Figure 1.3.

Rotational deformities in the lower limb on the other hand are usually quantified on a CT scan. For example, femoral anteversion is determined on a CT scan by measuring the position of the femoral condyles relative to the femoral neck. Tibial torsion is determined by measuring the amount of twist of the tibia from proximal to distal [21], [22].

1.2.1 Treatment of lower limb malalignment: corrective osteotomies

Not all patients with lower limb alignment need a surgical correction. A corrective osteotomy is only considered when a patient has a symptomatic deformation [22]. In general, patient groups that usually qualify for an osteotomy, are patients with single compartment osteoarthrosis, joint malalignment associated with ligamental laxity and instability, and patients with bone recurvatum [18].

If an orthopedic surgeon indicates a corrective osteotomy after clinical and radiological evaluation, multiple options exist. The most common options are performing a derotation osteotomy, a varus correction osteotomy, or a valgus correction osteotomy. It depends on the type of deformity in which osteotomy or a combination of osteotomies is needed to correct the lower limb axis. In general, a varus deformity is almost always caused by a deformity in the tibia, whereas

a valgus deformity often arises from a deformity on the femoral side (hypoplasia of the lateral condyle) or the tibial side (e.g. lateral tibial plateau fractures) [18]. However, this does not always apply.

Usually, the goal is to perform the correction in the bone where the deformity is present. To determine where the deformity is located in the lower limb, the method described by Paley et al. [21] is often used. This method uses the anatomical axes of both femur and tibia, which are the mid-diaphyseal lines of the bones. In the case of a deformed bone, both the proximal and distal anatomical axis intersect. This intersection point is called the Center Of Rotation of Angulation (CORA).

However, if the deformity is too large, or is present in both femur and tibia, a combination of osteotomies can be performed. These type of procedures is often executed by an orthopedic surgeon who is specialized in these types of osteotomies [18]. As a rule of thumb, a double-level osteotomy is indicated if the correction is more than 20° (or an opening wedge more than 17.5 mm), because of the increased soft tissue tension on the osteotomy site [25].

Types of corrections

The choice for an opening or a closing wedge osteotomy in the bone of interest usually depends on the patient-specific situation (for example, a patient already has had surgery before in that area), or surgical preferences. In most cases, opening wedge procedures are used for height restoration; however bone grafting of the opening gap may be needed. Moreover, an increased risk of a hinge fracture exists, which may result in a collapse of the osteotomy site eventually. Closing wedge osteotomies on the other hand usually heal faster with shorter rehabilitation times and have a possible lower risk of hinge fractures and nonunion or delayed union [26]. In contrast, closing wedge osteotomies are seen as more difficult procedures as two cuts are needed to perform the procedure; the perfect alignment of these cuts without any additional tools can be challenging [27]. Figure 1.4 shows locations where the sawing cuts for a lateral opening wedge or a medial closing wedge osteotomy can be made in the femur. In every patient, the orthopedic surgeon has to decide which type of osteotomy is most suitable.

One of the most important steps during the osteotomy procedure to obtain the desired bone correction is the placement of the saw cut for the opening wedge or the two cuts needed for the closing wedge osteotomy. In the latter case, the distance between the two cuts will determine the amount of correction that is achieved. The cuts must be made parallel to the joint line to prevent introducing an additional deformity in the bone. Moreover, the depth of the cuts is important as well. Cuts that are made too deep may result in a hinge fracture, whereas too superficial cuts may result in a hinge that is too stiff which makes it difficult to obtain the desired amount of correction. Making a surgical plan before the procedure seems to benefit the goal to obtain the desired amount of correction [28].

Outcomes after a corrective osteotomy procedure

The reported outcomes after a corrective osteotomy procedure vary. Reported survival rates before requiring a total knee prosthesis vary from 75 to 96.5% after 5 years; reported success rates of correction osteotomies are often lower.

In addition, intra- and postoperative complications occur after a corrective osteotomy. Apart from general surgery-related risks of complications (such as infection, thromboembolic complications, wound healing issues), complications such as compartment syndrome, infraction of the lateral tibial head (in case of tibial osteotomies) vascular damage, hematomas, nerve damage, fixation failure, loss of correction, or plate removal because of irritation or pain, occur in these procedures [29]–[32]. Reported complication risks vary between 3.5% [30], [31] and 31% [29].

1.3 Ongoing discussions regarding the execution of corrective osteotomies

A correction osteotomy around the knee is an example of a surgical procedure within orthopedics on which no consensus exists on the alignment targets of the lower limb. Therefore, it is still unclear how a certain correction is related to patient outcomes [18], [33]. The osteotomy correction targets are mainly based on a few studies. The first fundamental study was done by Fujisawa et al. in 1979 where they presented histological evidence of fibrocartilage regeneration in a study with 54 patients who underwent a valgus high tibial osteotomy for osteoarthritis [34]. In this study, the mechanical axes were corrected to a point that was 30%–40% lateral to the midpoint of the tibial plateau. Work built on this research described pre-operative planning methods [35], or introduced slight alternations such as the modified Fujisawa point which takes the degree of medial articular damage into account as well [36]. Others such as Paley bundled the information about the principles of deformity osteotomy corrections and further defined nomenclature and normal values for bone alignment parameters derived from small groups of healthy participants [21]. Nevertheless, determining patient-specific osteotomy targets and predicting osteotomy outcomes remains a challenge, as well as defining indications for an osteotomy, as no surgical standards are still defined [12], [18], [37], [38].

Interestingly, the abovementioned methods to determine the needed amount of correction (by Fujisawa or Paley) are all based on the lower limb alignment on a weight-bearing whole leg radiograph, which is a two-dimensional image. However, lower limb malalignment is a three-dimensional problem. A pre-operative planning is prone to error if it is made on a two-dimensional weight-bearing image. This is because it difficult to accurately determine the HKA angle that is used to determine the amount of correction. The HKA angle on weight-bearing whole leg images can vary up to 2° compared to CT HKA angle measurements [39]. Additionally, the surgical accuracy that an orthopedic surgeon can achieve when not using any additional tools adds to this variation. This makes it difficult to achieve the intended amount of correction.

Due to the variation in surgical options and difficulty to perform the surgery accurately, it is difficult to predict the outcome after a corrective osteotomy. In multiple articles reviewing corrective osteotomies, patient outcomes are not related to the execution procedure, as this is currently impossible to do due to the heterogeneity in execution options [18]. However, accurate surgical execution leading to better predicting outcomes is desired to prevent complications that arise from unintended leg stance over- or under-corrections or intended leg stance corrections that do not have the desired patient outcome.

To gain more insight in how a certain stance correction is related to patient outcomes, executing a surgical plan accurately is crucial. Therefore, a surgeon needs additional tools. In the field, two options are mentioned to support accurate surgery. First, literature reports that optical navigation has been used to perform corrective osteotomies accurately [40]–[43]. Overall, good results were obtained with these optical navigation systems, with the option to intraoperatively evaluate the results. In addition, this technique avoids inadvertent change in tibial posterior slope angle and may support the execution of complex osteotomies. Although its additional accuracy is proven in some studies, clinical benefits remain unclear [40], [41]. Pitfalls of the system are mentioned as well, such as the technical difficulties experienced while working with this system. Other pitfalls include the additional reference frames that are needed to know where the femur and tibia are located, and the tedious calibration methods that have to be executed before the system can be used.

Second, patient-specific cutting guides or Patient-Specific Templates (PST) are mentioned in literature as well as an option to accurately execute a preoperative surgical plan periopera-

tively [18], [38], [44], [45]. Accurate execution and easy usage are the main advantages that are mentioned in literature. Still, perioperative jig fitting problems, weakness of the jigs, and the time-consuming process of developing a PST are mentioned pitfalls of these guides.

However, the abovementioned tools are not used on a large scale for the execution of corrective osteotomies. Therefore, the problems still exist of having no insight into how the execution of corrective osteotomies are related to patient outcomes on one hand, and preventing over- or under-corrections on the other. Hence, there is a need for another way of accurately executing a surgical plan.

1.4 Aims and objectives

The goal of this thesis is twofold. The first goal is to identify how surgeons deal with the above-mentioned challenges and discussions regarding the execution of corrective osteotomies, and whether surgeons would benefit from techniques to make a surgical planning more easily available within the operation room. The second goal is to investigate whether US is a good alternative to use in the process of accurate osteotomy surgery. The thesis is divided into two parts where both these clinical and technical aspects will be discussed.

Part II focuses on further identifying the execution of a corrective osteotomy in clinical practice with its challenges and hurdles through interviews with orthopedic surgeons. These interviews showed that improvement of the registration procedure is essential for the clinical adoption of more accurate surgical tools. Hence, multiple registration options were compared for further investigation, and it was decided to further explore using ultrasound for the registration procedure.

Part III focuses on the technical feasibility of using US for the registration procedure by evaluating several parameters that influence the registration accuracy (see chapter 4). These simulations showed that the amount of noise present in the US measurement data had a large influence on the overall registration accuracy. Therefore, an additional experiment was conducted where the measurement accuracy of an US transducer regarding the detection of the bone surface was determined (see chapter 5) to see how large the contribution from the sensor to the overall registration accuracy was. The found measurement inaccuracy was used to perform a final round of simulations with more accurate results.

This thesis concludes with chapter 6, where the found results will be discussed, and some perspectives will be given on the feasibility of this registration technique in osteotomy cases.

Part II

Identification of the clinical challenges regarding corrective osteotomies around the knee

Chapter 2

Surgical experiences regarding osteotomies around the knee

In this chapter, orthopedic surgeons are interviewed to obtain insight into the osteotomy procedure and the possible challenges they face when executing a corrective osteotomy.

2.1 Introduction

An osteotomy around the knee is a procedure that realigns the lower limb [42]. Most of the patients who undergo a corrective osteotomy of the lower limb have osteoarthritis, but this procedure was executed in patients with trauma, congenital deformities, or chondrocyte defects as well [21], [31]. The overall goals of an osteotomy are to improve function, decrease pain if present, and slow down knee deterioration in case of osteoarthritis while preserving the original knee joint as long as possible [46].

However, the outcome measures reported in literature after a corrective osteotomy vary, regardless of the precise location or surgical technique of the osteotomy. Reported survival rates before requiring conversion to a total knee replacement vary from 75%–96.8% after 5 years or 51%–95% after 10 years for a high tibial osteotomy [47], [48], and reported success rates of correction osteotomies are often lower [18], [49].

Furthermore, intra- and postoperative complications occur after an osteotomy, regardless of the type or the location of the osteotomy [49]. Smaller and older case studies reported complication rates of up to 57% [50]. Although surgical techniques have improved over the last years, recently reported overall complication rates still vary between 3.5% [30], [31] and 31% [29].

To date, it is poorly understood why a correction osteotomy of the lower limb fails or why complications occur nowadays. Therefore, this chapter aims to gain more insight into the execution procedure of a correction osteotomy and to identify possible challenges an orthopedic surgeon experiences during this type of surgery that might explain the above-mentioned variation in reported numbers.

2.2 Methods

In total, 14 participants who worked in four hospitals in the Netherlands or France were interviewed. The experience regarding the execution of osteotomies varied from assisting in these procedures to decades of experience. Semi-structured interviews were held to allow the participants to elaborate more on a certain topic or question if the opportunity emerged. A questionnaire was designed to discern the perceptions of orthopedic surgeons and trainee orthopedic surgeons towards the execution of correction osteotomies around the knee. For this questionnaire, the osteotomy process was divided into seven different stages. Per stage, questions were created to gain insight into the different stages an orthopedic surgeon executes within this

stage to cover the complete osteotomy procedure. Moreover, interviewees were asked about challenges that may be experienced within each operation stage. In addition, questions were asked about the use of currently available techniques supporting the surgeon during surgery as well as promising future techniques to stimulate interviewees to think about alternative approaches within the osteotomy procedure. Questions regarding the advantages and disadvantages of using optical tracking during surgery were asked to several neurosurgeons as well since they used optical navigation daily.

One interviewer conducted all of these interviews face-to-face or via an online meeting. Notes were made during and after each conducted interview. The answers of each participant were summarized and noted in a table. After the interviews were conducted and summarized, overlapping answers were used to prioritize the given answers. For the analysis, labels were introduced based on these answers to find coherence between the given answers.

2.3 Results

The questions that were asked were categorized per stage and can be found in Table 2.1. A summary of the given answers per stage of the osteotomy process is described below.

Stage 1 - Positioning and sterile covering of the patient

Interviewees stated that this stage had to be functional and was assumed to be the basis for the rest of the surgery. It was mentioned that usually this stage is executed following a standard procedure according to hospital guidelines and consistent practice.

When asked about using a preoperative planning, all interviewees stated that a global planning was made in terms of the amount of correction in degrees in one plane, type of osteotomy, and the surgical approach, but without further details on the exact cutting locations in the bone. Such a planning was based on CT scans in case of rotation deformations, or on x-rays of both legs in all other cases. The majority stated that the planned amount of correction was based on 'an assumed normal limb alignment', or on 'an educated guess'. Within this context, some participants mentioned that it is still unclear what the optimal limb alignment is to strive for, and how this alignment is related to patient outcomes.

Stage 2 – Incision and reaching the bone surface

Generally, participants agreed that practice and experience contributed to a faster and more precise reaching of the bone surface. The interviewees used retractors to maintain good visibility of the surgical area while using sharp and blunt instruments to separate the surrounding soft tissues (mainly muscles and fat tissue) such that the bone surface could be reached. The presence of more soft tissues and fibrotic tissue were mentioned as factors that could hinder this process. For most participants, the size of the incision was less important within this process.

Stage 3 - Positioning of the osteotomy device on the bone

Interviewees stated here that experience was important in the determination of the exact position of the osteotomy device on the bone. K-wires and fluorescence imaging techniques were used by the majority of interviewees to verify and improve this position.

When asked about desired support (visual, audio, haptic, or other types of support) during the positioning of the saw, the majority stated that those types of support could be of added value. Some mentioned the use of augmented reality as a possibility to guide an orthopedic surgeon to a preplanned cut position, although some mentioned that at the moment this technique is too inaccurate to use perioperatively. Almost no interviewee was enthusiastic about using infrared navigated techniques in this process. Arguments were the extra time it takes to calibrate, the line-of-sight occlusion during use, the non-intuitive workflow when looking at the

screen instead of looking at the patient when operating, and the inaccuracy of the navigation system during the procedure. In addition, the lacking robustness and compatibility of the currently used infrared navigation systems with other imaging systems in the operation room were seen as pitfalls as well.

Moreover, some mentioned the use of PST as a positive development, as they found this a fast and easy-to-use tool to accurately execute preplanned cuts. However, others disagreed and mentioned negative experiences with PST. For example, they mentioned that the PST did not

Table 2.1: Overview of the questions that could be asked during the semi-structured interviews. The surgical procedure around an osteotomy was broken down into seven stages to map the complete osteotomy process. The questions were categorized per stage.

Stage 1 - Positioning and sterile covering of the patient
• How do you determine how the patient is positioned in the operation room? What factors do you take into account when deciding this?
• Do you make a surgical plan before the operation? If so, how detailed is this planning and how is this planning made? Why do you choose to (not) use a surgical plan?
Stage 2 – Incision and reaching the bone surface
• How do you determine the size of the incision and how important is this size to you?
• How do you make sure that you reach the intended location at the bone surface through the soft tissue?
• How do you ensure to maintain enough visibility within the operation area? Which anatomical landmarks limit the visibility onto the bon the most?
• Do you always manage to reach the bone surface in the intended way? If not, what caused this? What are potential factors that impede this process of reaching the bone surface?
• Are there any other surgical options to reach the bone that you currently do not use because of current (surgical, anatomical, or other) limitations? And if you could work more accurately as an orthopedic surgeon, would that change the way you would perform the operation? If so, what would change and why?
Stage 3 – Positioning of the osteotomy device onto the bone
• How do you make sure that the osteotomy device is positioned onto the bone as desired?

• If you would want to use some form of support during the positioning of the device you want to perform your osteotomy with, what kind of support would have your preference and why:
  • Visual support
  • Audio support
  • Support for positioning the osteotomy device
  • Other option, being….

Stage 4 – Performing the osteotomy
• What kind of osteotomy device(s) do you use or prefer? What do you like about this/these device(s)? What are the disadvantages of using this/these device(s)?
• Which considerations do you take into account when performing an osteotomy?
• How accurate do you think you are when performing an osteotomy compared to the exact location you want the osteotomy to be?
• What matters create inaccuracies during the osteotomy?
• How do you make sure that no other surrounding structures are damaged during the osteotomy?
• If you did not have to worry about damaging surrounding structures, would you use a different approach for the osteotomy?
Stage 5a – Repositioning of the bone parts
• How do you determine when the bone parts are in their intended position (before the actual fixation)? Do you use any additional tools to determine this?
• How much time does it take to reposition the bone parts relative to each other?
• Which factors can hamper this repositioning process?
Stage 5b – Refixation of the bone parts
• How do you make sure that the bone parts are refixed in their new intended position?
• What materials do you use for the refixation of the bone parts? What are pros and cons of this fixation material? Could you think of another way of bone fixation that may be more beneficial compared to current method(s) you use?
Stage 6 – Perioperative evaluation of the obtained result
• How do you evaluate perioperatively whether the intended result is obtained after repositioning and refixation of the bone parts? Do you miss anything in terms of evaluation tools to evaluate this? And if so, what is currently lacking or what kind of method would you desire instead?
• According to you, is there any type of osteotomy that gives the most unsatisfied with the obtained results? If so, what are the causes of not obtaining the intended result?
Stage 7 – Closing the fasci and skin
• What are factors that could hamper closing the fasci?
• How important is the way of closing the fasci and incision in obtaining the intended result?

have a unique fit on the bone, or that it did not fit at all perioperatively. Others mentioned that the guided cuts were still too inaccurate due to the minimum diameter sizes of the slots in the PST causing the saw to still move within the slots and the flexibility of the used saws during cutting. No interviewee currently used surgical navigation or augmented reality during current procedures, and only one interviewee used PST for guided osteotomy cuts regularly.

Stage 4 – Performing the osteotomy

All interviewees used some type of oscillating saw, sometimes in combination with osteotomes, to make the required bone cuts. K-wires and fluorescence imaging techniques were used by the majority of interviewees to guide the cuts within the bone.

All participants agreed that it was challenging to control the saw in three directions at the same time and to precisely create the bone cut as planned, since maintaining the desired orientation and positioning of the saw in 3D without any guidance remained difficult, even with a large amount of experience. Some mentioned that additional instrumentation to protect the surrounding soft tissues did not always prevent damage to the surrounding structures.

Stage 5 – Repositioning and refixation of the bone parts

Most interviewees mentioned that this was the most difficult stage in the operation procedure. They emphasized that it was difficult to maintain the intended repositioning configuration without breaking the hinge while fixating the bone parts with plates and screws. The new bone configurations were determined using tools such as a protractor or osteotomes with a known length, or by "eyeballing" and using their experience. Refixation of the bone parts via screw and plate positioning was not preplanned in 3D in most procedures. Drilling holes and plate localization were determined while the bone parts were held in their new position by hand or by a retractor (in case of an open wedge osteotomy). Almost all interviewees saw room for improvement within this stage.

Table 2.2: Brief overview of the given answers during the semi-structured interviews regarding the surgical procedure around a correction osteotomy.

Stage 1 - Positioning and sterile covering of the patient
• Global planning is made (type of osteotomy, surgical approach), but not in detail. Planning is generally based on educated guess and experience, importance of planning differs per interviewee
Stage 2 – Incision and reaching the bone surface
• Size of incision is nontrivial
Stage 3 – Positioning of the osteotomy device onto the bone
• Based on eyeballing and experience, general feeling that this 'often goes well'
• Currently available support techniques (navigation, PSI) barely used as it 'does not fit into the current workflow', 'too complex to use for this procedure', or is 'unnecessary'
Stage 4 – Performing the osteotomy
• Difficult to saw perfectly in three directions ('saw slips away', 'difficult to control the depth of cut', 'sometimes challenging to prevent soft tissue damage'), experience is important within this process
• Expressed need for visual (3D) support during this stage
Stage 5 – Repositioning and refixation of bone parts
• Mixed feelings ranging from 'inaccurate stage in the process' and experiencing 'difficulty controlling the bone parts' to experiencing 'no difficulty at all'
• Accurate correction in 2 or 3 planes without tools not possible
• Room for improvement
Stage 6 – Perioperative evaluation of the obtained result
• Via eyeballing, feels inaccurate to some interviewees
• Room for improvement
Stage 7 – Closing the fasci and skin
• Seen as a standard procedure and does not get special attention

Stage 6 – Perioperative evaluation of the lower limb stance

Most interviewees reported that perioperative evaluation of the correction was based on experience and the human eye in addition to X-ray imaging to evaluate plate and screw localization. Only one participant mentioned having used electric wiring or a mechanical axis system to evaluate the mechanical axis alignment on X-ray imaging within the operation room, but experienced these methods to be inaccurate and did not use these techniques any more. Another respondent had used infrared navigation in the past to evaluate the mechanical axis of the lower limb as well, but experienced inaccuracies with this system and did not use this system anymore. Participants saw room for improvement within this stage as well.

Stage 7 – Closure of fasci and wound

Most participants did not experience any difficulties in this stage. Some interviewees mentioned that the soft tissue coverage of the fixation plate at the tibia was a problem in some cases. They mentioned that some patients had pain at the plate location resulting in the removal of the plate and screws after a while, or an increased risk of infection in case the wound could not be closed properly.

The most important outcomes of the semi-structured interviews are summarized in Table 2.2.

2.4 Discussion and Conclusion

With the semi-structured interviews, it was aimed to obtain insight into the execution of a correction osteotomy. Moreover, it was tried to identify challenges that an orthopedic surgeon experiences during this type of surgery that may explain why postoperative osteotomy outcomes vary. The semi-structured interviews showed that variation exists among surgeons regarding the leg stance that is aimed for, the execution of a correction osteotomy around the knee, and the importance of a surgical plan within this process. The positioning of the osteotomy device on the bone and performing the osteotomy is often based on eyeballing and experience. It is difficult to control the osteotomy device in three directions while not damaging surrounding soft tissues. Commercially available techniques that could provide more control are not widely used. Controlling the created bone parts during repositioning and refixation was difficult. The perioperative evaluation of the obtained results was based on eyeballing.

No similar literature was found where individual surgeons were asked about their experiences with correction osteotomies around the knee, operation techniques they use, and obstacles they observe when executing this procedure. Most of the mentioned challenges resulting in a complication have been mentioned in literature, particularly in studies that investigated complication rates after a correction osteotomy [29]–[31], [51]. Mentioned planning and operation techniques have been described in several theory books as well. They illustrate the fact that there is still no consensus on the used techniques within these procedures [18], [21], [35], [36], [52].

The semi-structured interviews were not exhaustive, due to the relatively small number of participants. The recruitment of these interviewees from a limited number of hospitals (n=4) may have resulted in selection bias. However, the answers during the semi-structured interviews do provide insight into the correction osteotomy process and highlight some challenges the interviewees had to deal with that are shown in Table 2.2.

The interviews illustrate that an accurate and controlled execution of a corrective osteotomy around the knee remains difficult, and that experience plays an important role in this process. Tools meant to support the surgeon in a more accurate and controlled execution such as patient-specific instrumentation and navigation systems are not widely used.

In addition, the interviews showed that it remains unclear what the optimal patient-specific correction is to strive for since the correlation between a certain osteotomy correction and patient outcomes afterward is still poorly understood. As a result, no guidelines exist on what a patient-specific plan should look like or how accurate a corrective osteotomy around the knee should be executed. Consequently, different opinions on the importance of a surgical plan were observed during the interviews [12], [53].

Recommendations and further outline of the thesis

As long as an accurate and controlled way of executing a surgical plan for a corrective osteotomy remains difficult, it is complex to predict what an optimal stance correction will be. Thus, only if surgical plans are made and accurately executed, improved predictions of individual patient outcomes can be made that determine what the optimal stance correction for a patient is. In this way, data is produced of stance corrections that are accurately executed according to a surgical plan, which can be used as input for predictive models to adjust surgical plans accordingly based on previous experience. Therefore, detailed surgical planning should get more attention within the surgical process.

Adopting new techniques to execute surgical plans with high accuracy seems unavoidable since the semi-structured interviews showed that currently available techniques to execute a preoperative plan have their weak points. These hamper their usability in the operation room. The process of accurately aligning a preoperative plan to the patient's anatomy (for example the registration procedure) remains difficult with the currently available techniques.

Therefore, the next step focused on finding techniques to simplify and improve the registration procedure within this context. Appendix A provides more context around this subject and insight into the decision process of choosing a suitable registration technique. Based on this analysis, it was chosen to focus the rest of the thesis on investigating the feasibility of using US as registration technique for corrective osteotomies of the femur. In part III, first some background information on US will be given, followed by two chapters where the technical feasibility of using US for aligning a surgical plan to the anatomy of the patient is investigated.

Part III

Feasibility of using ultrasound as non-invasive bone registration tool

Chapter 3

Brief background information on ultrasound

Diagnostic ultrasound (US) techniques can be used to visualize the bone surface in a non-invasive and non-radiative way without the need for manual pinpointing landmarks. This technique uses transducers that produce sound waves with frequencies usually ranging from 2 MHz up to 18 MHz to characterize different types of subcutaneous tissue by measuring the reflection of these sound waves. The amount of reflection depends on the density of the tissue and the speed of the sound wave traveling through that tissue. Therefore, this reflection is an indicator of the type of tissue. The transition between soft tissue and bone is visualized with US since ultrasound cannot travel through bone and all signal is reflected at this transition area.

Bone can be visualized using either A-mode US or B-mode US. A-mode US or Amplitude Modulation uses the information of one sound wave to determine the bone surface location at one point. B-mode US or Brightness Modulation uses multiple sound waves to determine the bone surface in one plane [55], [56].

Apart from the non-invasive and non-radiative way of imaging, an additional advantage of using an US system is that it may be used as a tracking system as well. Then, a new registration can be performed continuously instead of only at the beginning of the procedure, making the registration and tracking procedure more robust [57]. Continuous registration enables tracking

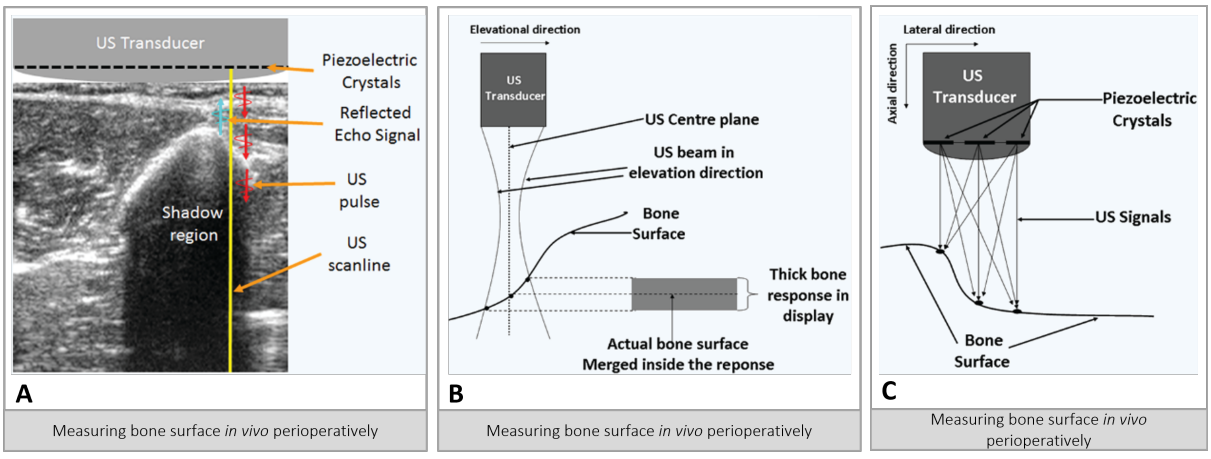

Figure 3.1: A) Overview of how an US image is created. Sound waves (red arrows) propagate perpendicular to the piezoelectric crystals at the top, in the direction of the yellow line. At the interface between soft tissue and bone, the signal is reflected (light blue arrow) and travels back to the transducer, where it is measured. **B)** Transducer seen from the lateral side. When the beam diameter in the elevational direction increases, the bone surface variation in that direction merges and is displayed as a thicker appearing line. **C)** Transducer seen from the front side. A rougher surface geometry results in a thicker appearing bone response since the received echoes from different directions cause blurriness around the echoes from the main direct line of sight [54].

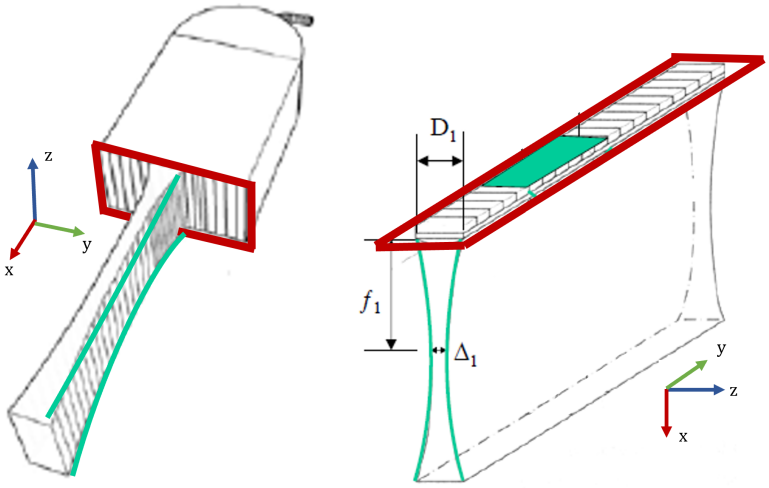

Figure 3.2: Figure showing the three-dimensional volume that is imaged with an US transducer. The transducer is constructed of piezoelectric crystals. The left figure shows the image volume of one piezo-electric crystal, the right image shows the complete image volume from another angle. The more piezo-electric crystals, the more detailed the image will be in the lateral direction (the y-direction). The size of the piezoelectric crystals in the elevational direction (D_1) determines the elevational thickness of the image volume (the z-direction). At the focus position (position f_1) the thickness will be smallest (Δ_1). Adapted from [56] and [59].

of lower limb kinematics with US during surgery. Moreover, it potentially enables accurate perioperative evaluation of the surgical lower limb stance correction, which may have added benefit for the execution of the procedure.

3.1 Bone appearance in ultrasound images

US uses transducers that produce sound waves with frequencies usually ranging from 2 MHz up to 18 MHz to characterize different types of subcutaneous tissue by measuring the reflection of these sound waves. The amount of reflection depends on the density of the tissue and the speed of the sound wave traveling through that tissue. This is expressed as the acoustic impedance of a tissue. If these acoustic impedance values are different between neighboring tissues, a high acoustic impedance mismatch occurs, and a large portion of the sound waves will be reflected. This happens, for example, at the interface between air and skin, or between soft tissue and bone. Therefore, the transition between soft tissue and bone can be clearly distinguished with US: almost all signals are reflected at this transition as the bone has a high acoustic impedance compared to other soft tissues such as muscle, fat, liver, or water [54]. The resulting high-intensity pixel appearance indicates there is a strong likelihood of a boundary being present there, such as the interface between soft tissue and bone. This region is followed by a low-intensity region, also called the 'shadow region', which is the deeper surfaces of the bone that cannot be imaged with US imaging [55], [58].

One of the biggest challenges of segmenting the bone surface in US images is that the bone surface can appear in different ways. The soft tissue-bone surface interface is not a sharp transition region but appears as a bright thick line with a diameter of up to 4 mm in certain cases [54]. The thickness of this line is affected by two factors. First, the inclination angle between the US transducer and the bone surface is of importance: the greater this inclination angle, the greater the thickness of the bone surface on US images. Second, the thickness of this bone response is affected by the transducer beam thickness in the elevational direction (see Figure 3.1B). This causes a thick response in a 2D US image, especially when the surface geometry of the underly-

ing bone is not flat (as shown in Figure 3.1) [60]. Both phenomena result in a thick appearing high-contrast line on the US image. As a result, determining where the actual bone surface begins is challenging.

The quality of the US image is related to the type of US transducer. The transducer images a three-dimensional volume that is shown in a two-dimensional plane. This principle is shown in Figure 3.2. The size of this total three-dimensional volume differs per transducer. The smaller this volume, the more detailed the image will be. Especially the size of the piezoelectric crystals in the elevational direction (z-direction in Figure 3.2) determines how thick the white-appearing bone line is in US images. The size of the piezoelectric crystals in the elevational direction is estimated to be around 3 mm around the focus (indicated with f_1 in Figure 3.2). This means that 3 mm of bone is projected onto a plane, resulting in a bone line that is smeared out in the US image. Because of this phenomenon, logically the angle between the bone and the transducer affects the thickness of the white appearing bone line as well [54], [61].

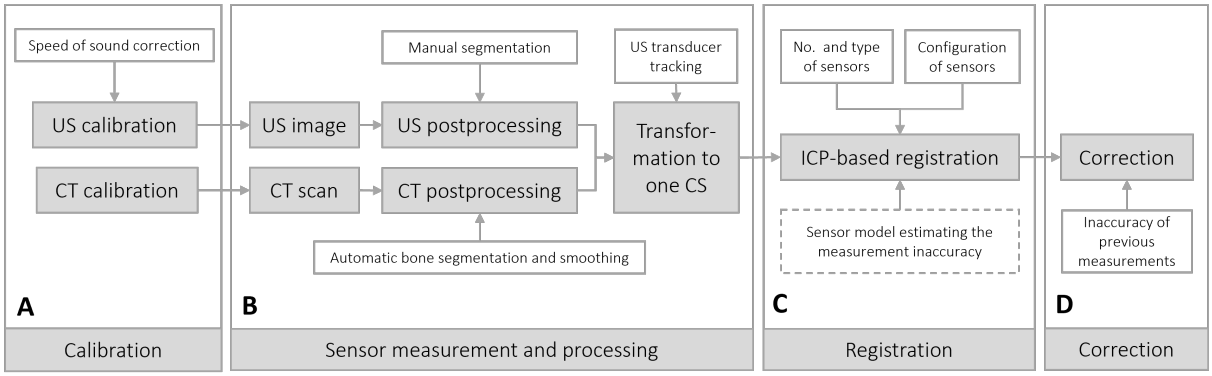

Figure 3.3: Global overview of the signal processing steps of the ultrasound (US) sensor (in grey blocks), where multiple sources of inaccuracy (white blocks) are pointed out. **A)** In the calibration phase, initial parameters are set (the speed of sound is in this case the most important factor for US calibration). When using a diagnostic US device or CT scan, the calibration parameters are already initialized within the device or scanner itself by the manufacturer. **B)** In the sensor measurement and processing phase, data are collected (US image and CT scan) and processed such that the bone surface is extracted from both imaging modalities. These bone surfaces are transformed such that they are expressed in the same coordinate system. **C)** In the registration phase, the extracted bone surface data from the CT scan is used to register the US bone surface points onto the CT segmentation using the Iterative Closest Point (ICP)-based registration method as described in chapter 4. Factors that influence this registration, are the number and type of US sensors used, the configuration of the US sensors, and the amount of measurement inaccuracy of the previous steps (calibration and sensor and processing). In chapter 4 a sensor model that estimated the measurement inaccuracy (block with dashed lines) was made to predict the measurement inaccuracy of the prior phases (**A** and **B**). **D)** Additional correction, for example based on previous measurements, can be performed to obtain a more accurate overall registration accuracy.

3.2 Further outline of part III

In part III of the thesis, multiple factors of measurement inaccuracy will be evaluated. An overview of how these factors influence the registration accuracy at different stages of the registration process is shown in Figure 3.3. Chapter 4 will further focus on the technical feasibility of using US as a registration tool by investigating the registration accuracy under different circumstances. In this chapter, the effect of measurement inaccuracy on this accuracy will be evaluated using computer simulations. A sensor model is used to estimate this measurement inaccuracy. Hence, chapter 4 focuses on the registration part shown in Figure 3.3C.

Still, as Figure 3.3 shows, more factors influence the accuracy of the complete pipeline. The dashed block with the sensor model in Figure 3.3C is an estimation of the accuracy of both the

'calibration' part (Figure 3.3A) and the 'sensor measurement and processing' part (Figure 3.3B). Therefore, it is important to have a sensor model that estimates the measurement inaccuracy as a realistic representation of the real measurement inaccuracy. Hence, chapter 5 will further focus on further improving the sensor model by quantifying the measurement inaccuracy caused by the US sensor when measuring bone.

Chapter 4

Evaluation of using ultrasound sensors for an accurate registration of the femur with an ICP-based algorithm

The biggest technical challenge when using ultrasound (US) as bone registration tool is the limited amount of bone surface information that is available for the registration. To determine whether it is technically possible to use US for an accurate alignment, it is crucial to evaluate which information of the bone surface from US is needed for this accurate registration. Therefore, this chapter focuses on evaluating the technical feasibility of using US information for this registration using computer models. Multiple conditions regarding the type of US sensor, sensor positioning, and effect of measurement inaccuracies are evaluated.

4.1 Introduction

A fundamental property in performing surgery according to a surgical plan is to project the surgical plan to the anatomical situation in the operation room. This procedure is known as the registration procedure [57], [62]. Generally, registration is done via intraoperative identification of preoperatively defined landmarks by the surgeon. Although this manual point-to-point matching principle is often used as a registration method, it is suboptimal since the accuracy of this technique is highly dependent on the user's landmark identification skills [63]. Moreover, it increases surgery time and requires larger bone exposure [64], [65]. Therefore, it is important to find a registration method that is less prone to human error, easy to use, and ideally less invasive.

US has the potential to be used as an efficient modality in an intraoperative setting. US can provide preoperative information to the intraoperative setting in a non-invasive and non-radiative way, without the need for manually pinpointing landmarks [60], [61], [66]. Figure 4.1 shows an overview of how US can be used for the alignment of the patient anatomy and the surgical plan.

An accurate registration is crucial for the application of US-based registration method in clinical practice. Available navigation systems have translational and rotational errors of 1 mm and 1° or higher, respectively [67]. Therefore, the translational and rotational error of a registration method using US should be around 1 mm 1° as well, respectively.

Different US modes are suitable for imaging bony structures, the most relevant modes being the A- and B-mode. A schematic overview of A- and B-mode sensors is shown in Figure 4.1A.

With an A-mode sensor, the distance between skin and bone is determined in a single direction, whereas a B-mode sensor enables measuring the distance between bone and skin in two dimensions [54].

Both A-mode and B-mode have their advantages and disadvantages. A-mode on one hand requires small sensors and less data post-processing for detecting the bone surface. However, the bone-skin distance is measured at only one position on the bone surface. Moreover, the A-mode beam direction must be perpendicular to the bone surface during a measurement, which limits A-mode applications. On the other hand, B-mode allows more flexible image acquisition regarding positioning and provides bone surface imaging in two directions. However, the larger-sized

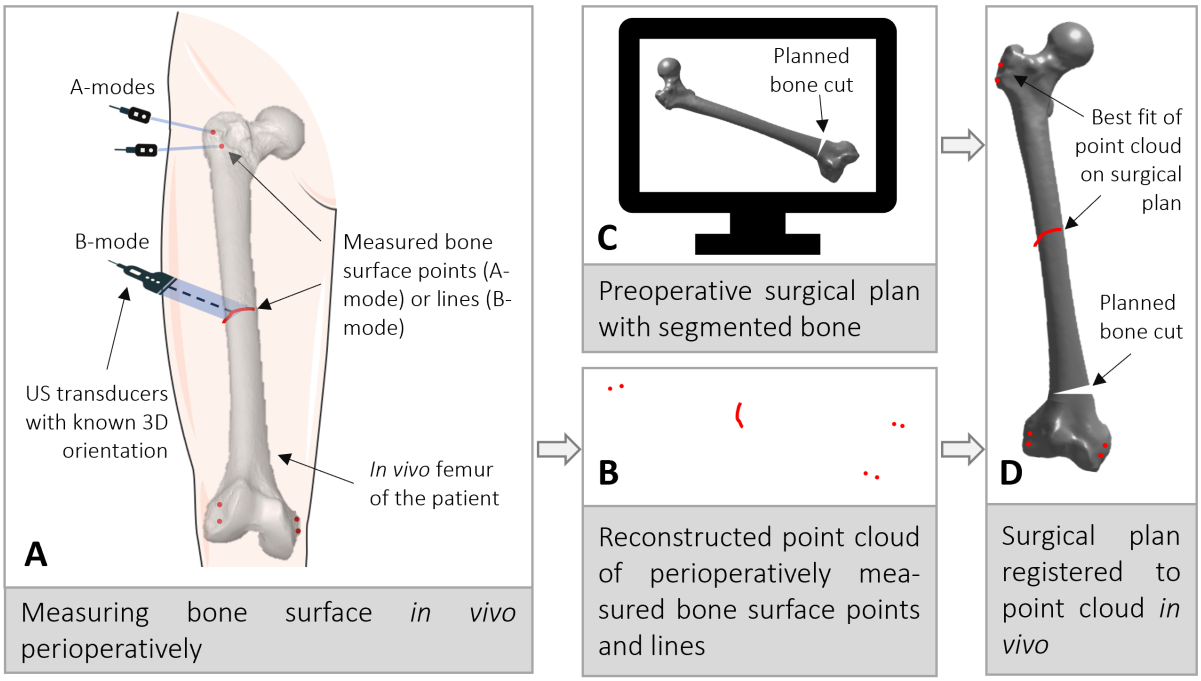

The added value of using US for this registration over other pinpointing landmarks-based registration methods is the US sensors do not have to be placed at predetermined positions that are specified in the surgical plan (as shown in C) as well. Therefore, this method provides automatic registration and may be more accurate compared to registration methods based on pinpointing landmarks.

The added value of using US for this registration over other pinpointing landmarks-based registration methods is the US sensors do not have to be placed at predetermined positions that are specified in the surgical plan (as shown in C) as well. Therefore, this method provides automatic registration and may be more accurate compared to registration methods based on pinpointing landmarks.

Figure 4.1: Overview of the proposed registration technique with US (US). In this example, a combination of A- and B-mode US sensors is used for the registration procedure. **A)** Different bone surface points (A-mode) and lines (B-mode) are measured on a patient's femur with US sensors. The 3D position and orientation of the US sensors are known. **B)** The measured bone surface points and lines are constructed into a 3D point cloud. **C)** The surgical plan made before the surgery contains the exact locations of the bone cut(s), in this example a distal femoral medial closing wedge osteotomy. This plan can be made for example from the data of a preoperative CT scan. **D)** The bone segmentation of the surgical plan (as shown in C) is registered to the bone surface point cloud (as shown in B). In this way, the surgical plan is aligned to the anatomy of the patient in the operation room. Due to a limited number of US measurements, this alignment is not perfect.
The added value of using US for this registration over other pinpointing landmarks-based registration methods is the US sensors do not have to be placed at predetermined positions that are specified in the surgical plan (as shown in C) as well. Therefore, this method provides automatic registration and may be more accurate compared to registration methods based on pinpointing landmarks.

B-mode sensor is more difficult to attach to the skin and B-mode requires computationally more expensive signal post-processing [57], [61].

When using US for a bone-registration procedure, multiple aspects are currently unclear regarding the technical feasibility. First, it remains unclear which type of US sensor achieves the set requirements for intraoperative registration procedures of the femur. Registration procedures between femoral segmentations from CT scans and either A-mode [68], [69] or B-mode [70]–[72] have been described in the literature, however varying registration and tracking accuracies were reported among these studies. Moreover, no research has been published where A-mode and B-mode input for registration procedures have been compared.

Second, it is unclear where US sensors have to be positioned for an accurate femur bone registration. Since US sensor positioning influences the accuracy of this registration, optimizing this US sensor placement for both A- and B-mode is important. However, only a limited number of previously published studies take US sensor positioning into account when investigating registration accuracies. Their results do not provide a definite answer on where to position the sensors on the femur or how many sensors are needed for an accurate registration [73]–[75].

Therefore, this chapter aims to investigate whether a femoral registration using a combination of either A, or A- and B-mode US sensors can achieve the requirements of 1 mm and 1° of translational and rotational error. The performance of A-mode and a combination of A- and B-mode sensors will be compared by answering the following questions:

1. *How many sensors are needed to perform a registration with an accuracy of 1 mm and 1°?*
2. *How does the sensor positioning affect the registration performance?*
3. *What is the effect of measurement inaccuracy on the registration performance?*

These three criteria were chosen since they determine for a large part the user-friendliness of this registration system and its potential future use.

4.2 Methods

Monte Carlo analyses were performed to evaluate the registration performance of different modeled A- and B-mode US input combinations. For these simulations, the model described by Niu et al. [76] was taken as a starting point and further extended. They performed simulations to determine the number of A-mode sensors needed for femur alignment.

The general idea behind the simulations is that it is investigated which bone information from US is needed to obtain a good overlay between the measurements and the virtual bone model. The US sensor data is virtually modeled in different ways and used as input for the registration to determine which input data results in registrations that meet the set accuracy requirements.

The methods section is constructed as follows. First, the modeling of the virtual US sensor data is described. Then, the registration process is further explained. The last part describes how the registration results are evaluated in terms of translational and rotational accuracies. An overview of the methods section is given in Figure 4.2.

4.2.1 Virtual model for ultrasound measurements

First, a virtual model of the US measurements was created. This model provided bone surface measurements that could have been obtained with an A- or B-mode US sensor. Multiple

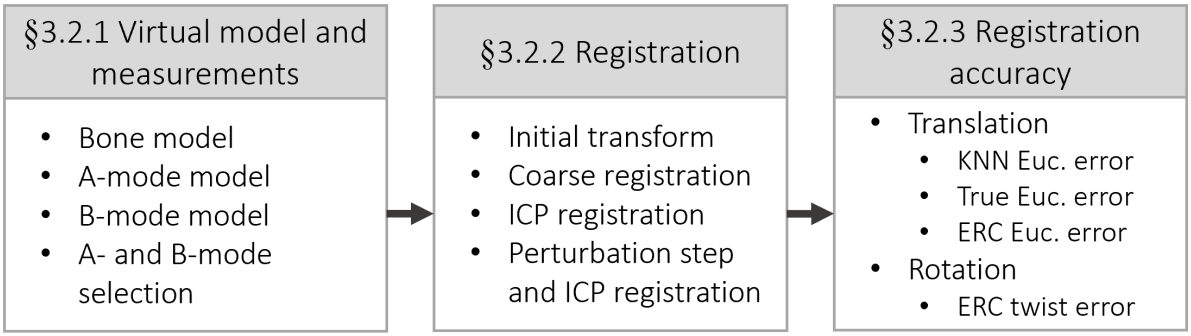

Figure 4.2: Global overview of the simulation setup. The paragraphs indicate where the corresponding information is described in this chapter.

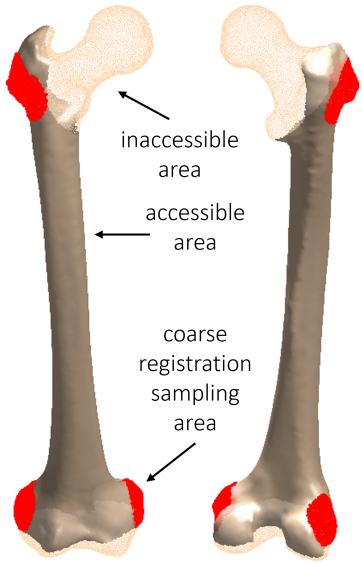

Figure 4.3: Figure showing the virtual bone model, seen from frontal (left) and distal (right) side. The three areas used for the coarse registration (first registration step) are shown in red; the solid bone area and the red area together were used to model US measurements. The bone surfaces that cannot be measured with US (femoral head, distal condyles) are shown in dots.

assumptions were made to generate this model, which will be explained in the next paragraphs.

Bone model

A virtual bone measurement model was made, containing the bone areas that could be measured with US. For this model, it was assumed that no measurements could be obtained from the femoral head, the distal part of both condyles, and the area between both condyles. Moreover, three coarse registration areas were defined at the greater trochanter, the lateral and medial epicondyle. These regions were used for sampling the US A-mode measurements that were used in the first registration step for a robust registration. Figures 4.3 show what the virtual bone measurement model looks like.

A-mode model

A measurement model of the A-mode sensor was made. This model modeled A-mode measurements of the bone surface as single three-dimensional coordinates located on the virtual bone

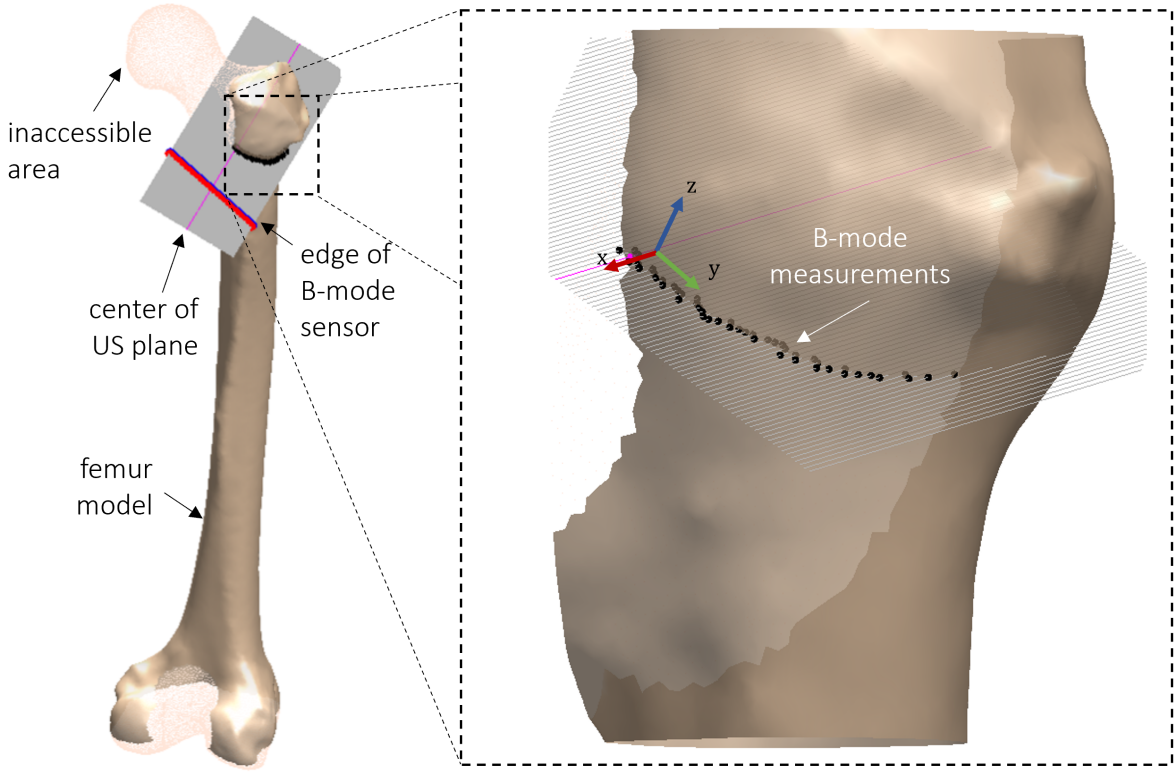

Figure 4.4: Example of B-mode measurements produced by the virtual B-mode model. The US plane (in grey) was modeled as multiple lines with the same orientation. At the center of the US plane (the magenta line), the plane was oriented perpendicular to the femoral bone mesh. B-mode measurements were found by determining the intersection between the modeled US plane lines and the accessible areas of the femoral bone mesh. In-plane B-mode measurement inaccuracy was modeled as uniformly additive noise in the x-direction of the local coordinate system (as indicated).

measurement model in case no measurement inaccuracy was present. Measurement inaccuracy was modeled as uniformly distributed additive noise in all directions. The size of this inaccuracy varied within the simulations.

B-mode model

A measurement model of a linear B-mode sensor was made. B-mode measurements were modeled as multiple three-dimensional dots lying in a three-dimensional plane (the US image plane) located on the virtual bone measurement model in case no measurement inaccuracy was present. It was assumed that this US image plane had a width of 56.1 mm (in azimuth direction). The center of this plane was oriented perpendicular to the virtual bone measurement model.

For B-mode measurements, two types of measurement inaccuracy were modeled, being in-plane measurement inaccuracy (in the B-mode image plane) and inaccuracy in determining the correct orientation and positioning of the B-mode sensor. The in-plane measurement inaccuracy was modeled as normally distributed additive noise with a mean value of 0 mm and a standard deviation of 1 mm in the axial direction of the plane. The second measurement inaccuracy source was modeled as uniformly distributed additive noise in all directions. The size of this inaccuracy varied within the simulations. Figure 4.4 shows an example of measurements that this B-mode measurement model could produce.

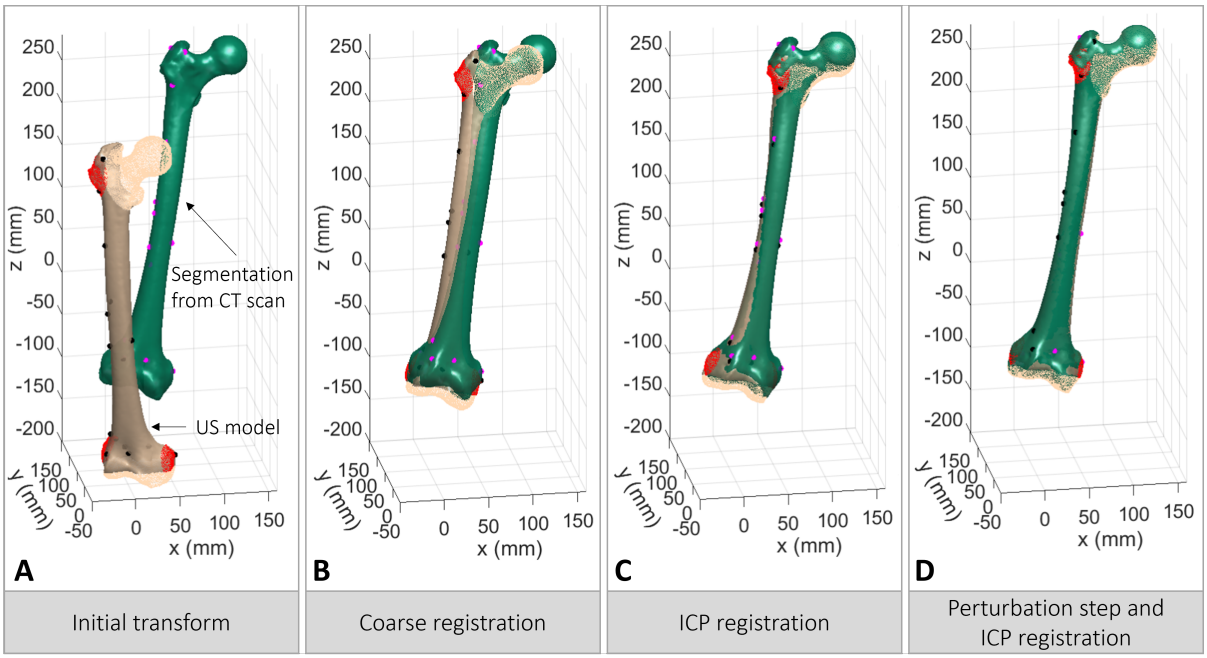

Figure 4.5: Overview of different registration steps. Here, the black dots represent the US measurements, the US model is the point cloud from which these US measurements are sampled. The green femur represents the CT segmentation of the femur (ground truth), with corresponding ground truth US measurements in magenta. The aim is to register the black US measurements to the green US model after an initial transform of the CT segmentation (as shown in **A**). The registration itself is performed via three registration steps. First, the six coarse registration points from the coarse registration areas are used to perform a rigid SVD registration with the three centers of the coarse registration areas on the CT segmentation model. This results in a global overlay as shown in **B**. Subsequently, an ICP registration is performed with all US measurements for a more accurate registration shown in **C**. Finally, a perturbation step and ICP registration are performed to avoid ending up in a local minimum. The result after this final registration is shown in **D**. The perturbation and ICP registration can change the found registration slightly, but this is not always the case.

Measurement selection

A virtual model of the US measurements was created in MATLAB. Therefore, a segmentation of a femoral bone of a healthy subject from a CT scan from Pellikaan et al. [77] was used. Only the parts of the femur that are visible with US were included in the mesh, meaning that the femoral head and the distal part of the femur were removed from the mesh. The remaining mesh contained 25784 vertices (points) and 51140 faces (surfaces connecting the vertices); the vertices are referred to as the accessible CT data points hereafter.

US data points were sampled from this mesh to create the virtual model of the US measurements. In the case of A-mode simulations, bone surface points were selected from the accessible area as shown in Figure 4.3. In the case of B-mode simulations, bone surface lines were selected from the accessible area as well, as shown in Figure 4.4 A.

4.2.2 Registration of ultrasound measurements to CT segmentation

The work of Niu et al. [76] was used as a basis for the registration algorithm. The global idea of the registration simulations was to find alignment between the simulated US measurements and the segmentation from the CT scan. Therefore, the CT segmentation is first transformed to a known arbitrary location. Then, the US measurements are aligned with the segmentation from the CT scan using a registration algorithm containing multiple steps. This principle is shown in figure 4.5. These steps are further explained below.

1. First, the CT segmentation was randomly transformed to a new location. This process is called the **Initial transform**. For this random transform, the CT segmentation could be rotated maximally 45° degrees and translated maximally 100 mm relative to its initial position.

2. A **coarse registration** was performed to obtain a global overlay between the US measurements and the CT segmentation. Two points from the coarse registration areas as indicated in Figure 4.3, meaning in total $2 \cdot 3$ points were selected as US measurements. These points were registered to the centers of the corresponding coarse registration areas to obtain the global overlay. Hence, in total six points were used for the coarse registration.

3. An **ICP** registration was performed next to obtain a more accurate registration [78], [79]. This registration was performed with the six points from the coarse registration and additionally selected points (as explained later in this section). The ICP optimization was stopped in case a maximum of 100 iterations was reached, or the subsequent transformation did not differ more than 0.05 mm and 0.01° for translation and rotation from the previous transformation, respectively.

4. A rotational **perturbation** of the US measurements as described by Niu et al. [76] was applied along the longitudinal axis next. This was done to find a more accurate registration by systematically searching for better fits to escape possible local minima of the registration method. The **ICP registration** of step 3 was repeated in case the perturbation step provided a lower K-nearest neighbor (KNN) Euclidean error (see section Determining the registration accuracy) than the KNN Euclidean error obtained after step 3.

4.2.3 Registration accuracy

Four measures were used to quantify the residual localization error after the registration procedure. Two measures were based on the Euclidean distance between the CT segmentation

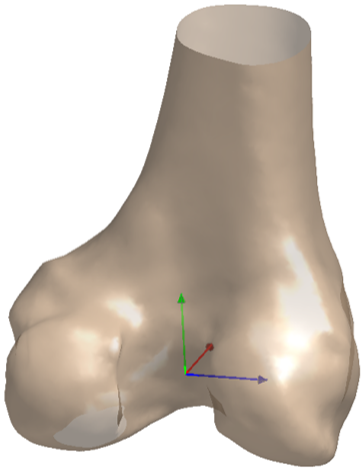

Figure 4.6: Figure showing the position and orientation of the anatomical coordinate system in the femur (ERC reference frame) by Miranda et al. [80].

Figure 4.7: Figure showing the three different regions in which the femur was divided for B-mode position analysis: the greater trochanter region, the midfemoral region, and the distal femoral region.

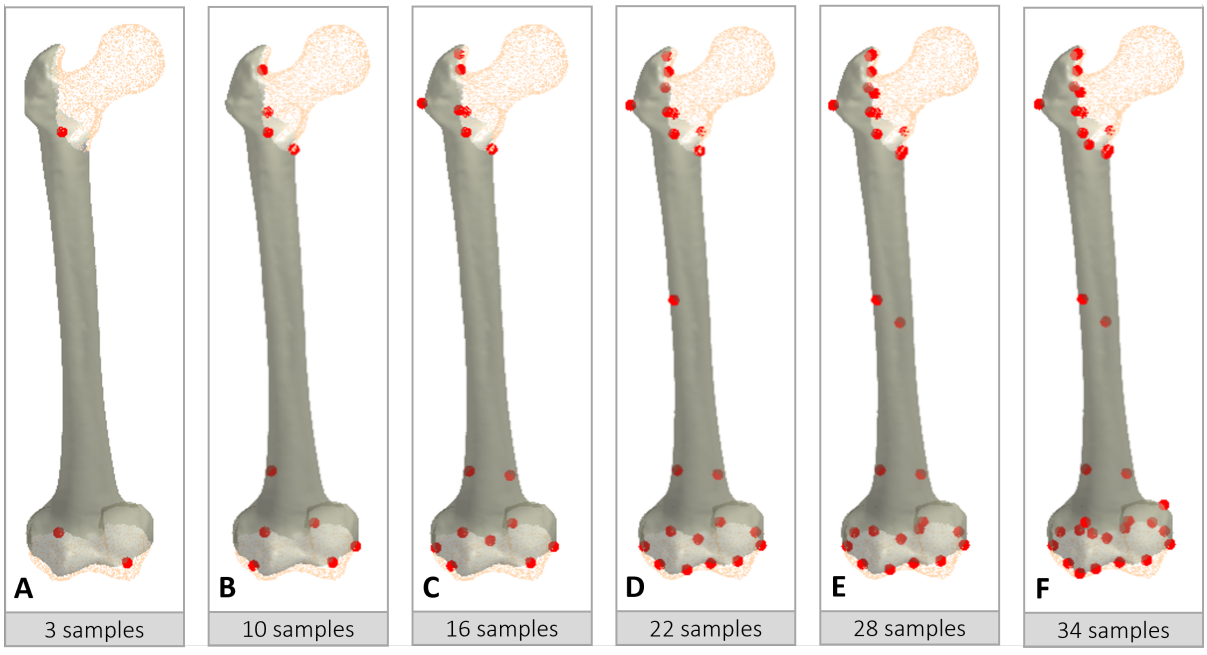

Figure 4.8: Sensor locations (indicated in red) chosen with respect to the geometric shape of the femur.

and the US measurements, and two measures were based on the alignment of the anatomical coordinate system described by Miranda et al. [80]. The latter two measures provide more insight into the actual alignment of the planning and the patient's anatomy in a clinical setting, hence they are more relevant to an orthopedic surgeon. The position and orientation of the femoral anatomical coordinate system are shown in Figure 4.6. This coordinate system is referred to as the ERC reference frame hereafter. The calculations of the four localization error metrics are explained below.

1. **KNN Euclidean error:** was calculated by:

$$\epsilon_{KNN} = \sqrt{\frac{\sum_{n=1}^{N} \left(\mathbf{p}_n - {}_n\right)^2}{N}}$$

   where $\mathbf{p}_n$ is the location of one of the US measurements, ${}_n$ is the closest neighbor point of the CT segmentation, and N is the total number of US measurements. This localization error is measurable during a real-life surgical procedure.

2. **True Euclidean error:** was calculated by:

$$\epsilon_{true} = \sqrt{\frac{\sum_{n=1}^{N} (\mathbf{p}_n - \mathbf{q}_n)^2}{N}}$$

   The only difference to the KNN Euclidean error calculation is $\mathbf{q}_n$ instead of ${}_n$, resembling the true corresponding points of $\mathbf{p}_n$. Hence, this parameter can only be calculated within a simulation setting and provides information about the true localization error.

3. **ERC Euclidean error:** was calculated by

$$\epsilon_{ERC,\ true} = \sqrt{(q_x - p_x)^2 + (q_y - p_y)^2 + (q_z - p_z)^2}$$

   where $\mathbf{p}$ is the 3D position of the origin of the ERC reference frame of the US data points, and $\mathbf{q}$ is the origin of the ERC reference frame of the CT data points. This localization error measures the registration accuracy at the distal femur.

4. **ERC twist error:** was calculated by:

$$\epsilon_{ERC,\ twist} = \arccos\left(\frac{\mathrm{tr}(\mathbf{R}) - 1}{2}\right)$$

   where $\mathbf{R}$ is the residual rotation matrix between the ERC reference frames of the US data points and the CT data points. Hence, this is a measure for the residual rotation between these two ERC reference frames and is a measure for the residual rotational error.

In the simulations, a maximum registration error of 1 mm of translation and 1° of rotation was used as guidelines to determine the number of sensors needed to obtain an accurate registration. These thresholds were chosen to have an accuracy similar to the currently available navigation systems, which is around 1° and 1 mm [67]. The ERC Euclidean error and the ERC twist error were chosen to report as the main outcomes for all simulations.

4.2.4 Setup of the Monte Carlo analysis

Multiple Monte Carlo analyses were performed to determine whether A-mode or B-mode sensors achieved the requirements of 1 mm and 1° registration difference. Details of both analyses are explained below.

A-mode evaluation

Number of sensors and their position

For determining the most suitable A-mode sensor positions, two different sensor placement methods were compared and are explained below: the random sensor placement and Geometric Shape Preservation (GSP) placement.

1. **Random sensor placement:** a uniformly sampled random combination of point locations was selected from the accessible areas of Figure 4.3 to serve as US measurements.

2. **GSP placement:** sensor locations were selected such that the overall shape of the original bone was preserved as much as possible. This was done by finding a determined number of mainly protruding landmark locations via an iterative process such that the volume of the resulting mesh is reduced the least. Figure 4.8 shows some examples of sensor locations that were used for these simulations. These were calculated using a special function in MATLAB [81].

To evaluate the influence of the number of sensors, each of these sensor placement methods was executed for 6 to 40 sensors. A minimum of 6 sensors was required to ensure a relatively accurate coarse registration with a mean ERC error of around 10 mm.

For each amount of sensors, 1000 iterations were performed in which sensor locations were changed in every iteration, meaning in total $34 \cdot 1000 = 34000$ iterations. The mean localization error and variability over all 1000 iterations per number of included sensors were calculated to determine the mean accuracy per number of included sensors.

Effect of measurement inaccuracy on the registration accuracy

To evaluate the effect of measurement inaccuracy, the abovementioned simulations with 34000 iterations in total were repeated with two levels of simulated added measurement inaccuracy. This measurement inaccuracy was modeled as uniformly distributed additive noise between -1 and 1 mm (first level) or between -2 and 2 mm (second level) over the sensor positions with isotropic distribution in all directions. The initial transforms were kept the same among different noise levels for a fair comparison between the performances of the simulations.

Combined A- and B-mode evaluation

Number of sensors needed and their positions

The analysis to determine where B-modes could be placed for the most accurate registration differed slightly from the A-mode analysis, since B-mode images a two-dimensional plane of the bone. It was chosen to divide the femoral bone into three segments to determine which combination of segments provided the lowest localization error. This choice was made since it was assumed that the registration accuracy using B-modes was less sensitive to B-mode positioning compared to A-mode positioning. These three segments were the proximal femur, mid-femur, and distal femur, as Figure 4.7 shows. In each segment, one B-mode sensor was placed 1000 times at an arbitrary location within these regions. The mean localization error per segment was calculated over these 1000 iterations. The B-modes were positioned with different orientations such that none of the image planes were parallel to each other.

Similar to the A-mode procedure, six points were positioned at the greater trochanter, the lateral, and the medial condyle. These points were kept constant during the iterations, meaning that the coarse registration step was the same for all iterations. Only steps 3 (ICP registration) and 4 (perturbation and ICP registration) were different during the iterations. Thus, both the B-mode sensor information together with these six points were used for registration steps 3 and 4.

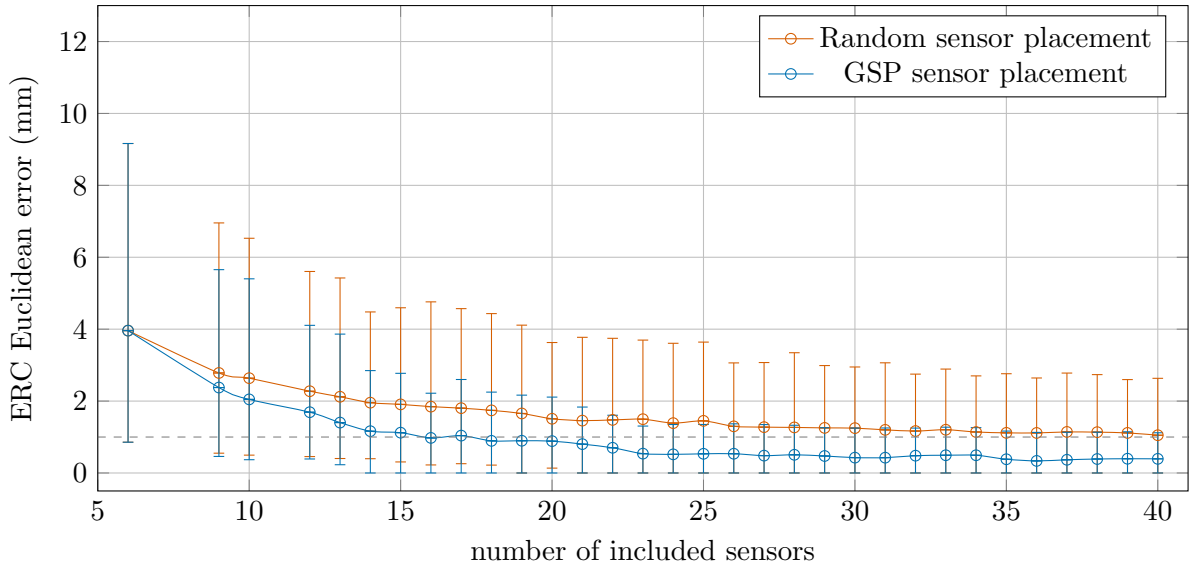

Figure 4.9: Figure showing the ERC Euclidean error after registration without added noise for random A-mode sensor placement (orange) and when placing the A-mode sensors such that the geometric shape is preserved as much as possible (GSP sensor placement, in blue). The error bars contain the 90% variation of the data.

Effect of measurement inaccuracy on the registration accuracy

The first simulation was performed assuming no measurement inaccuracy was present to evaluate the registration algorithm under optimal conditions. To determine the effect of additional measurement inaccuracies within the simulation two types of measurement inaccuracy (on B-mode positioning and in-plane inaccuracy) were modeled as described earlier in this chapter. The additive measurement inaccuracy on the B-mode positioning laid between -1 an 1 mm (first level) or -2 and 2 mm (second level). In both cases, the mean of this inaccuracy was 0 mm. For both levels, the added normally distributed in-plane B-mode measurement inaccuracy had a mean of 0 mm and a standard deviation of 1 mm.

4.3 Results

4.3.1 A-mode sensors

Number of sensors needed and their positioning

In the first part of the simulations, the most suitable sensor placement was evaluated. The results show that overall, the GSP placement provides more accurate registration results compared to random sensor placement. When only looking at the performance of the registration algorithm without considering measurement inaccuracy, 22 sensors or more sensors were needed and placed at the GSP locations for a registration accuracy of 1 mm and 1°.

These results are visualized in Figures 4.9 and 4.10, where the localization errors per method are shown. Both figures show that the mean ERC Euclidean error (Figure 4.9) and ERC twist error (Figure 4.10) are systematically lower when using the GSP sensor placement compared to random sensor placement. These plots indicate that at 16 (Figure 4.9) and 22 (Figure 4.10) sensors, a mean accuracy of 1 mm and 1° is reached, respectively.

Notably, the distribution of the ERC twist error values for GSP placement drops considerably when 13 or more sensors are included, as the right sub-figure shows. It is important to note that when 13 or more sensors are included, the shape of especially the lateral condyle is more accurately reflected by the GSP sensor points, as Figure 4.8B and C show.

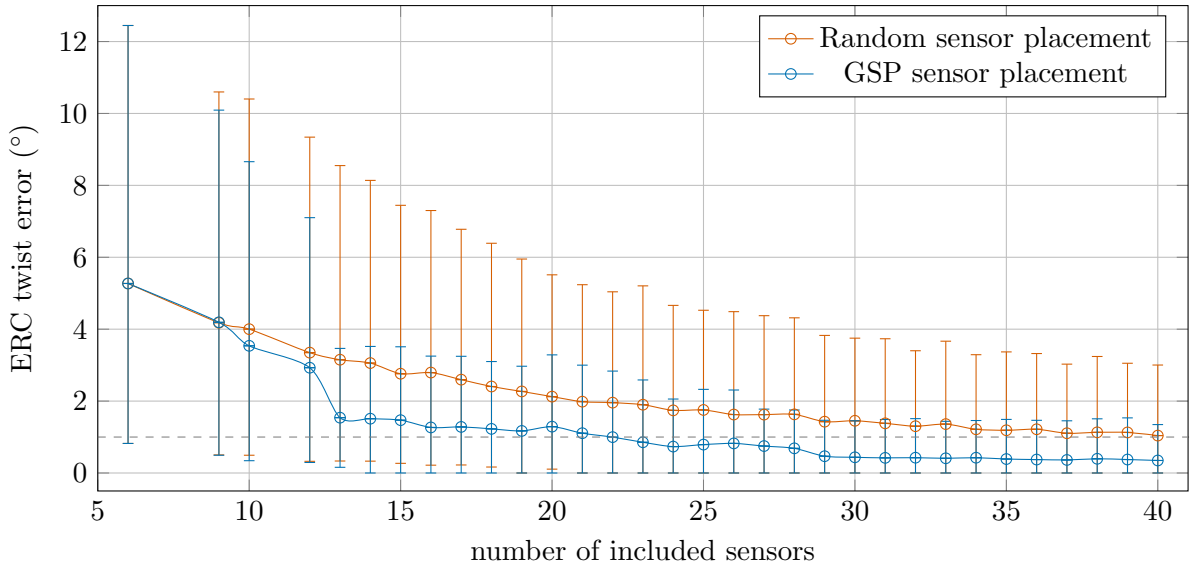

Figure 4.10: Figure showing the ERC twist error after registration without added noise for random A-mode sensor placement (orange) and GSP sensor placement (blue). The error bars contain the 90% variation of the data.

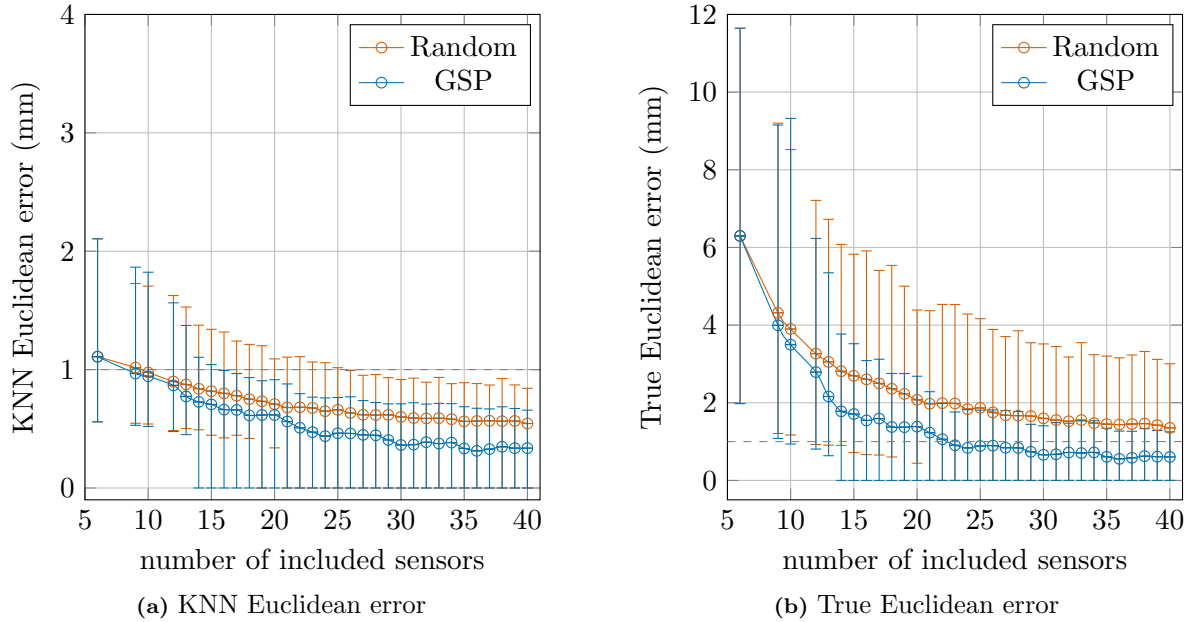

(a) KNN Euclidean error

(b) True Euclidean error

Figure 4.11: Figure showing the KNN and true Euclidean error after registration without added noise for random A-mode sensor placement (orange) and GSP sensor placement (blue). The error bars contain the 90% variation of the data.

Effect of measurement inaccuracy on the registration accuracy

Moreover, the simulations evaluated the effect of the measurement inaccuracies on the registration accuracy. In general, the findings show a registration performance decrease when measurement inaccuracy levels increase. Overall, the registration performance becomes increasingly worse when increasing the measurement inaccuracy. This can be seen in Figure 4.12, where different levels of measurement inaccuracy are added to the A-mode GSP sensor positions. Only adding noise to GSP sensor positions is shown here since these locations provided the most accurate registration results when not adding measurement inaccuracy.

When regarding the different error metrics in Figure 4.12, the KNN Euclidean error does not seem to be a reliable error metric for displaying the registration accuracy. The graphs show that the registration performance decreases when measurement inaccuracy increases. Moreover, the graphs reveal that the trend and the rate of decline shown by the KNN Euclidean error metric differs from that of the other localization error metrics. Especially when more simulated measurement inaccuracy is present within the simulation, the KNN Euclidean error does not seem to benefit from including more sensors. Other localization error parameters on the other hand decrease when more sensors are included.

4.3.2 Combined A- and B-mode sensors

Number of sensors needed and their positioning

The results reveal that in the case of random B-mode placement, at least two B-mode sensors or more (in addition to six A-mode sensors) are needed to obtain a mean registration accuracy of approximately 1 mm (true Euclidean error) or less. These findings are visualized in Figure 4.13. Figure 4.13 shows the influence of both the number of included B-mode sensors and different measurement inaccuracy levels on the registration accuracy. As mentioned before, six A-modes were included for the coarse registration, and the number of additionally added B-modes varied between one and seven.

Notably, the variability in measurement error was less compared to only including A-mode sensors (as shown in Figure 4.12), especially when the level of measurement inaccuracy is low.

Analysis of the best positioning of B-mode sensors showed that in the case of positioning one B-mode sensor, it was best to position it at the mid femoral region transversely. This area gave the lowest mean true Euclidean error of 3.6 mm of all evaluated regions. B-mode US measurements in the longitudinal direction of the femoral bone resulted in worse registration performances.

In the case of using two B-mode US sensors, the most accurate registrations were obtained when one B-mode US sensor was placed in the proximal femoral region and one in the mid femoral region, with a mutual distance of 100 to 200 mm. Results showed that the mean true Euclidean error was around 1.5 mm.

When using three B-mode US sensors, the simulations did not show a sensor placement strategy that provided more accurate registrations. All combinations of sensor positioning in different femoral segments resulted in mean true Euclidean error values of around 0.8 mm and mean ERC twist errors of around 1°. Using more B-modes did not result in a superior positioning strategy as well.

Effect of measurement inaccuracy on the registration accuracy

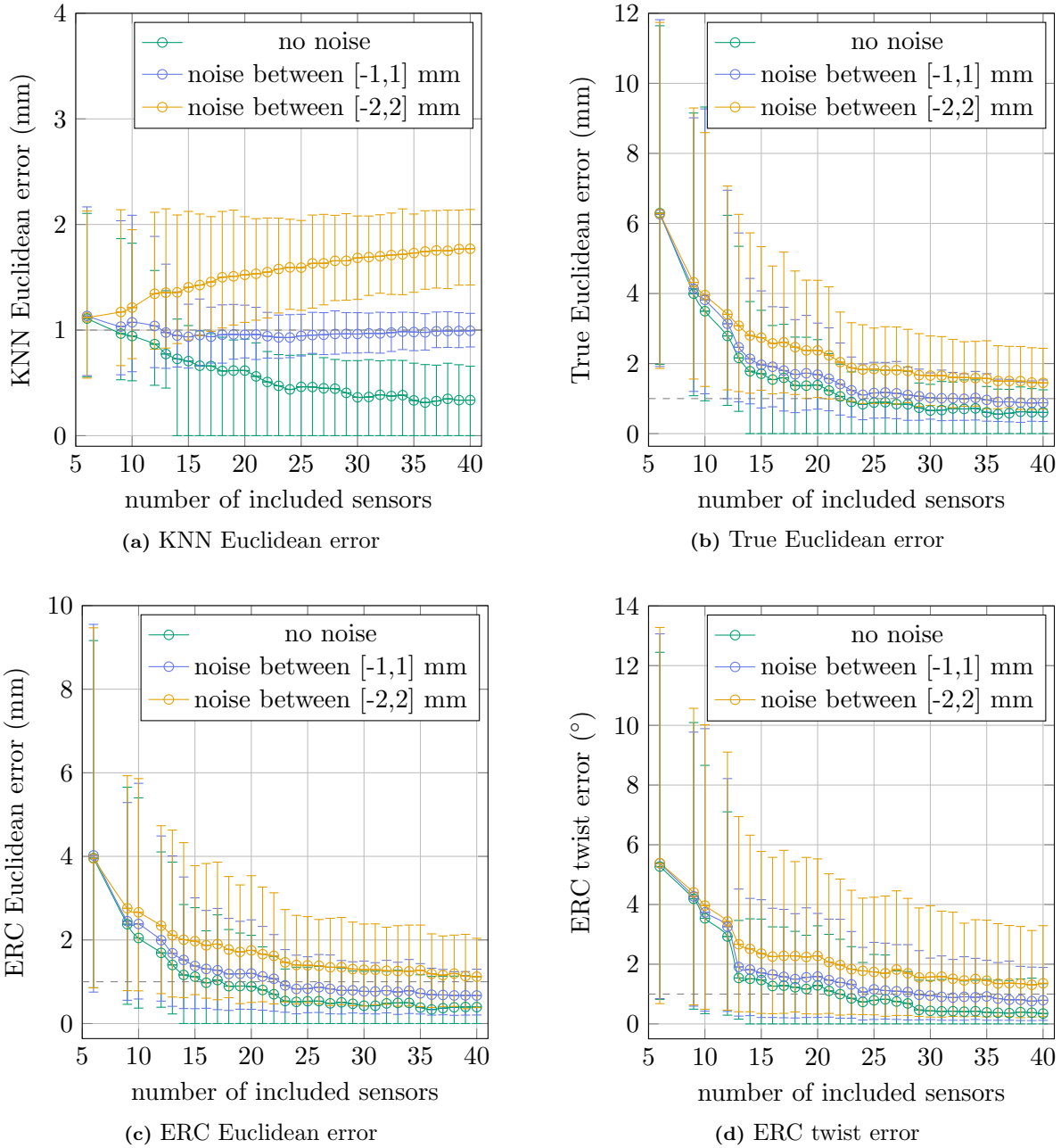

(a) KNN Euclidean error

(b) True Euclidean error

(c) ERC Euclidean error

(d) ERC twist error

Figure 4.12: Figure showing different localization errors of A-mode simulations after registration under different noise levels for GSP sensor placement. The error bars contain the 90% variation of the data.

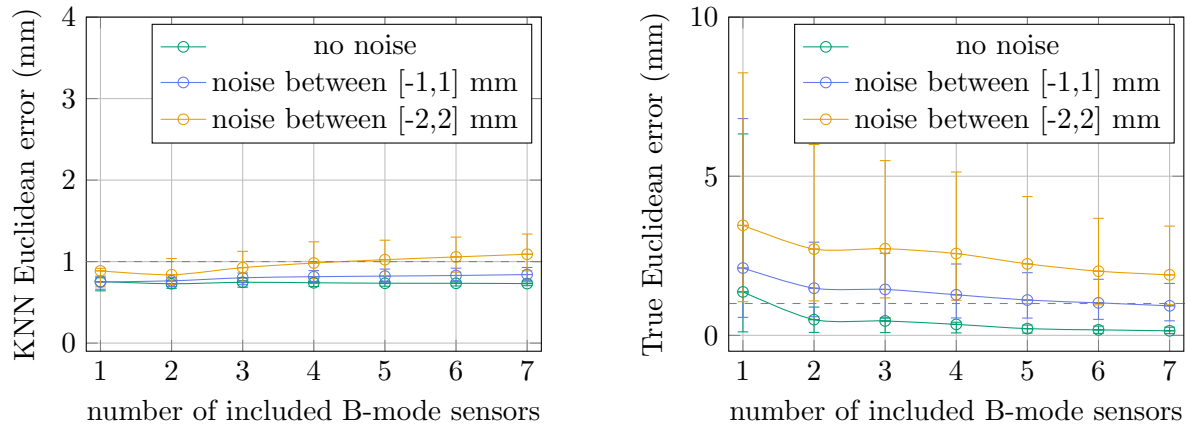

(a) KNN Euclidean error

(b) True Euclidean error

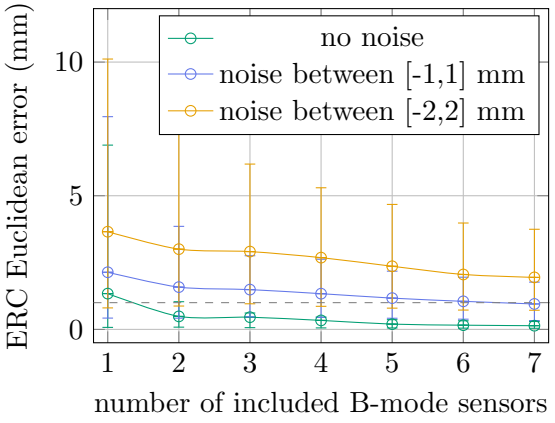

(c) ERC Euclidean error

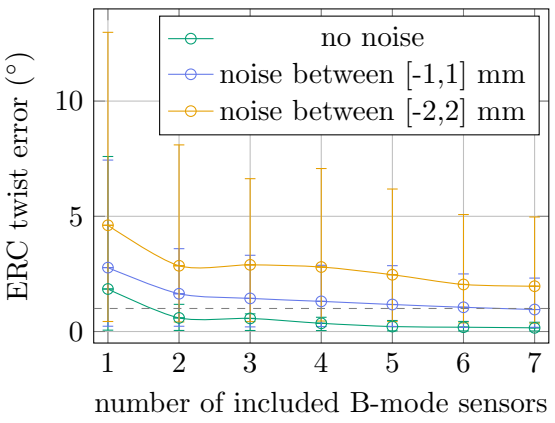

(d) ERC twist error

Figure 4.13: Registration accuracy results of combined A- and B-mode simulations. Different levels of measurement inaccuracies (no inaccuracy, inaccuracy between -1 and 1 mm, and inaccuracy between -2 and 2 mm) were used. The lines show the mean values of the localization error per number of included sensors. The error bars contain 90% of the data.

When regarding the effect of measurement inaccuracy, the results showed that a combination of A- and B-mode sensors was less sensitive to measurement inaccuracies compared to a combination of only A-mode sensors. This is shown in Figure 4.13, where different levels of measurement inaccuracy were used during the registrations. Similar to A-mode simulations, this figure shows that adding more measurement inaccuracy results in a less accurate registration, even when more sensors are included.

4.4 Discussion and Conclusion

In this chapter, the aim was to investigate which US modality is most suitable to use for intraoperative registration of the femoral bone when taking both accuracy and clinical feasibility into account by answering the following questions:

1. *How many sensors are needed to perform a registration with an accuracy of 1 mm and 1°?*
   The findings suggest that to obtain an accuracy of 1 mm and 1°, at least 22 A-modes or six A-modes and seven B-modes need to be included when assuming that the measurement inaccuracy is uniformly distributed between -1 and 1 mm.

2. *How does the sensor positioning affect the registration performance?*
   Especially A-mode sensor registrations are relatively sensitive to measurement inaccuracy and dependent on sensor placement. Therefore, A-mode registration seems to be less suitable for clinical applications since more sensors are needed to obtain an overall more accurate registration. The results indicate that performing a registration with a combination of A- and B-mode sensors is more robust to measurement inaccuracy and sensor placement. This combination provides a more accurate registration with fewer sensors needed.

3. *What is the effect of measurement inaccuracy on the registration performance?*
   When using only A-mode sensors for the registration, measurement inaccuracy has a large influence on the registration performance. When using a combination of A- and B-mode sensors, this effect is smaller. Still, this sensor combination depends on the amount of measurement inaccuracy present in the data as well. Therefore, it is recommended to quantify this measurement inaccuracy more accurately for a more definite answer.

The simulation results of Figure 4.12 showed 22 or more A-mode sensors positioned at GSP positions are needed to achieve the accuracy requirements. Under the assumption that the measurement inaccuracy is small, the mean ERC Euclidean error is less than 1 mm and a mean ERC twist error is less than 1° in that case. Still, the robustness of the GSP points is questionable since the registration performance still decreases when measurement noise is added. Indeed, when additive uniformly distributed noise with values either between -1 and 1 mm, or between -2 and 2 mm is added, respectively 30 and more than 40 sensors placed at GSP positions are needed to achieve similar registration accuracies, as Figure 4.12 shows. Moreover, A-mode registration seems to be sensitive to sensor positioning, since GSP positioning resulted in better registrations compared to random sensor placement as Figures 4.9 and 4.10 visualize. This limits its clinical application since it is unlikely that the A-mode sensors can be placed at the GSP positions with a high precision.

In the case of using a combination of A- and B-mode sensors, seven randomly placed B-mode sensors and six A-mode sensors were needed to obtain the required accuracy level of 1 and 1°. The results in Figures 4.12 and 4.13 suggest that adding both position and in-plane measurement inaccuracy to the B-mode sensor data affected the registration accuracy less compared to

the A-mode registration accuracy. If more than two B-mode sensors are included, their sensor positions do not considerably influence the registration accuracy.

The simulations showed that positioning sensors at tactical places reduces the number of sensors needed to obtain higher accuracy, but never beyond a certain registration limit associated with the amount of measurement inaccuracy present within the data. Therefore, improving the registration accuracy by placing sensors at protruding bony landmarks in case of A-mode, or at geometrically uniquely shaped surfaces in case of B-mode, only helps up to a certain degree.

An explanation for this registration limit can be the performance of the used ICP-based registration algorithm. One of the limitations of this algorithm is that it only used points for registration and does not consider the complete mesh to which these points belong. As a result, measurement inaccuracies introduced to these points directly influence the registration accuracy, especially when only a limited number of data points (sensors) are included. Therefore, with the current registration setup, a more accurate registration can only be achieved when the level of measurement inaccuracy is lower.

Moreover, ICP-based algorithms are prone to get stuck in a local minimum during optimization. An ICP algorithm tries to minimize the overall distance between two point clouds by aligning the point clouds as perfectly as possible with decreasing manipulations. Due to these decreasing manipulations, an ICP-based algorithm is prone to get stuck in a local minimum that may result in a decreased registration accuracy. The extra perturbation and repeated ICP registration were implemented to obviate this to a certain degree. A brute force method would completely counteract this effect, though that is computationally expensive and therefore not desired.

When comparing these results to literature, the accuracy levels found in the simulations seem to be in line with accuracy levels found in other studies regarding A-mode [68], [76] and B-mode [70] registration. However, the results are difficult to compare due to differences in reported outcome measures. For example, Gonçalves et al. [70] reported the Hausdorff distance as a measure of their registration performance. Other studies report Target Registration Error (TRE), with a minimum mean TRE of 1 mm and minimum variations of ± 0.3 mm [71], [72]. However, TRE is not an accurate measure to determine whether the registration is performed accurately [66]. The localization error measures used in this chapter provide a better understanding of the actual registration error and show that it is difficult to accurately evaluate a registration error in clinical practice, where only measures such as a TRE can be measured.

Only a limited number of previously published studies take US sensor positioning into account when investigating registration accuracies. Some papers recommend to use uniform sampling of the registration object for a potentially more accurate registration over a larger area [73], [74]. Vicini et al. found that positioning A-mode sensors on protruding landmarks provided the best registration accuracies of the scapula [75]. The results found here are consistent with these findings: especially A-mode sensor registration performs better when GSP sensor placement, where sensors are placed more on more protruding bone areas. In the case of using a combination of A- and B-modes, a more uniform sensor positioning results in higher accuracies. The results showed that suitable mutual distance between placement of three B-modes was around 100 and 200 mm.

Regarding the effect of measurement inaccuracy, Niu et al. reported that the ICP registration algorithm could handle small measurement inaccuracies between 0 and 1 mm. However, they had difficulty when these errors increased to levels between 1 and 2 mm [76]. Although the measurement inaccuracies were implemented differently in the simulations, a similar trend

was observed where increased measurement inaccuracies progressively worsened the registration performance.

The reported error metrics in this chapter together provide more insight into possible causes of registration inaccuracies. For example, the different error metrics showed that it is relatively more difficult to decrease the rotational error compared to the translational error. As mentioned, in case of no measurement inaccuracies at least 16 A-mode sensors should be included for a translational error of less than 1 mm, as Figure 4.9 shows. However, for a rotational error of 1° or less, the bottom right plot of Figure 4.10 shows that 22 or more A-mode sensors are needed. This is possibly due to the rather cylindrical shape of the femur, therefore having rotational symmetry. As a result, multiple registration configurations will result in similar error values, making it more prone to rotational errors. The extra perturbation and ICP step intended to decrease the rotational error, in fact only decreased the translational error.

B-mode measurements on the other hand seem to be less sensitive to rotational measurement errors. When comparing Figure 4.13C and D, both the mean ERC Euclidean error and the ERC twist error are around 1 mm and 1° when 13 sensors (six A-mode sensors and seven B-mode sensors) are included. This seems logical since naturally B-mode sensors capture more three-dimensional information about the bone, making it less prone to rotational errors. This is in line with literature [75].

Limitations

Several limitations of this study should be noted. First, the simulations that were used here differ in several aspects from the real-world situation, such as how measurement inaccuracies were simulated. In both A- and B-mode simulations, the measurement inaccuracy was simplified by using a normal noise distribution that was isotropic in all directions. However, in a real-life setting, the visibility of the bone is influenced by the presence of the surrounding structures of the bone. These surrounding structures (such as tendons, or fat) influence how accurate the exact bone position can be determined and is location-dependent. This factor was not considered within the simulations. Therefore, it should be further investigated what the influence of the location-dependent varying measurement inaccuracies is on the most suitable sensor positioning in an experimental setup.

Second, only a limited number of options were simulated for determining the most suitable B-mode locations. For example, only for three different starting configurations the most suitable B-mode locations were determined. This may have influenced the locations that were found. More starting configurations must be evaluated before the found most suitable B-mode placement locations can be fully evaluated.

Third, only one implementation of the ICP-based algorithm was used during the simulations. Although ICP-based registration methods are widely used for this type of application, it may not be the most suitable registration algorithm for registering sparse and noisy measurement data compared to data that are less sparse. The optimization function of the ICP algorithm that was implemented, tried to minimize the distance between points. When a lot of measurement inaccuracy is present, optimizing the distance between points does not necessarily result in a more accurate registration. Other optimization functions that minimize the distance between two point clouds by considering additional information, such as the mesh normals or point-to-plane distances, will possibly perform better in terms of accuracy and robustness, especially in the case of B-mode measurements [82]. Indeed, an accurate and robust registration algorithm is essential for this registration method to make its way into clinical practice, therefore more

research must be done to further optimize the registration algorithm.

Finally, with the current registration setup, a more accurate registration can only be achieved when the level of measurement inaccuracy in the measurements is relatively low. Currently, no additional filtering step is added to filter out this measurement inaccuracy. Filtering algorithms such as Kalman filtering may help to improve an accurate registration. Appendix C provides more information on this topic. Alternatively, when the data is made less sparse virtually, this problem may be obviated. For example, statistical shape models can be constructed from B-mode US data (as Barratt et al. [71] showed), which might make the registration procedure more accurate as more (virtually created) data points can be used within the registration.

Implications for clinical practice

Still, the simulations provide insight into the working mechanism of the registration algorithm with sparse data and allow for analyzing the effects of individual parameters such as sensor positioning or the influence of measurement inaccuracy without the interference of other factors. The results imply that theoretically, an accurate registration of a known bone shape can be made with only a limited number of US measurements. These findings highlight the potential of US to provide accurate preoperative information to the surgeon perioperatively. The simulations show that using a combination of A- and B-mode sensors can provide an accurate registration. Nevertheless, as the registration accuracy when using a combination of A- and B-mode sensors depends heavily on the amount of measurement inaccuracy present in the data, quantification of the measurement inaccuracy via an experiment is crucial for its potential application in clinical practice.

In conclusion, a combination of six A-modes and seven B-mode US sensors seem to provide a desirable accuracy. This combination is more robust to measurement inaccuracy and less dependent on sensor positioning compared to using only A-mode sensors. However, the registration accuracy that this combination of sensors can obtain is predominantly dependent on the amount of measurement inaccuracy present in the data. Hence, further quantification of the measurement accuracy is important for further evaluation of the technical feasibility of this registration method.

Chapter 5

Quantitative analysis of measurement inaccuracy of bone imaging with linear ultrasound: comparison between ultrasound and CT bone segmentations

The simulations in chapter 4 showed that measurement inaccuracy affects the registration accuracy between ultrasound measurements and the CT bone model. A realistic estimation of the measurement inaccuracy produced by the US transducer is important in the overall consideration of whether US is a good alternative for the registration of a surgical plan. In this chapter, this factor of measurement inaccuracy is further evaluated.

5.1 Introduction

Using a surgical plan in clinical practice implies that this plan must be projected to the anatomical situation in the operation room. Ultrasound (US) is an imaging modality that can visualize and locate the bone surface. Hence, US holds the potential to form a coupling modality between this surgical plan and the intraoperative setting. However, US images suffer from high levels of noise, imaging artifacts, bone surfaces appearing blurred and several millimeters in thickness, and a restricted field of view, which limits its application possibilities in clinical practice [54], [60], [61], [66]. These measurement inaccuracy factors can affect the registration accuracy between the bone segmentation and the surgical plan. Therefore, measurement inaccuracy was taken into account in the simulations described in chapter 4.

Still, it is unclear whether the measurement inaccuracy distributions used in chapter 4 are representative of real US measurements. Elaborate research on the characterization of the bone surface localization error on US images has not been reported in literature [54]. Since there are no agreed standards on how US bone segmentation should be evaluated, different ground truth modalities have been used to evaluate the accuracy of the bone surface localization error of US [66], [83], [84]. This research does not characterize the US in-plane measurement inaccuracy distribution and does not provide a definitive answer to how this inaccuracy can be modeled in simulations. Therefore, this chapter aims to further identify the bone surface localization error and its distribution on US images. With this information, the simulations of chapter 4 will be more realistic.

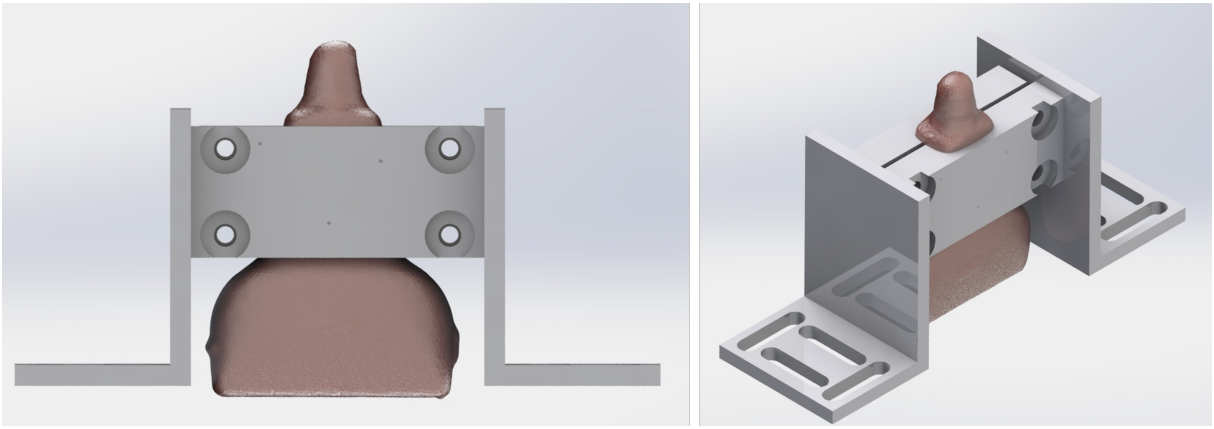

Figure 5.1: 3D printed holder with the US transducer. The three dots at the front of the holder are three positions where three fiducials (tantalum metal spheres with a diameter of 1 mm) were added to the holder. In addition, two extra tantalum metal spheres were attached at the back of the design (not visible here). Two plastic screws were used to clamp the US holder in between the two holder parts.

5.2 Methods

The global idea behind the measurements was to compare US images made of bone to bone images made with CT to determine the measurement inaccuracy of a B-mode US transducer. Since CT is considered as the gold standard for imaging bone, CT was chosen as modality to compare the US images with [66]. Although the image resolution of US is usually better compared to CT, this comparison does provide insight into whether US images contain a bias or a large variation in the bone depth compared to CT. US measurements were made inside the CT scanner, and both measurements were taken at approximately the same moment. In this way, the US transducer position and orientation were shown on the CT scan and could be used for reconstruction of the US image plane from the CT scan. The bone depth in this reconstructed plane, seen as the ground truth, was compared to the bone depth determined from the corresponding US image. The calculated mean measurement inaccuracy levels were used to repeat the simulations of chapter 4 with these more accurate measurement inaccuracy levels. More detailed information on the execution of the experiment is given below.

In total, 11 combined US-CT measurements were made. Figure 5.2 shows the experimental setup used for these combined US-CT measurements. The high-resolution CT scans were made with a spiral CT scanner (Aquilion ONE CT scanner, Canon Medical Systems Europe B.V.) with voxel sizes of $0.625 \cdot 0.625 \cdot 0.30$ mm, meaning that in the slice-direction the voxel size was smallest. The 11 US images were made with a linear transducer (14L5 transducer, maximal axial depth range of 7 cm), and a diagnostic US scanner (Aplio i800 System, Canon Medical Systems Europe B.V.). These images had a pixel resolution varying between $0.0507 \cdot 0.0507$ and $0.109 \cdot 0.109$ mm.

The US transducer was attached to the cadaver using a custom-made 3D printed holder (see Figure 5.1). This US holder was designed by a technician of the Orthopedic Research Department of the Radboudumc, Nijmegen. A surface mesh made of a 3D photo of the US transducer (3dMDhead^{TM} system, 3dMD Limited) was used to create a cavity in the custom-made holder. This re-ensured a tight and unique fit between the holder and the US transducer. Five tantalum fiducials were added to the custom-made holder as a double check for determining the orientation and positioning of the US transducer within the CT scan.

Consent was retrieved from the manufacturer of the US device (Canon) and the head of the Radiology Department at the Radboudumc in Nijmegen, the Netherlands, for conducting these measurements.

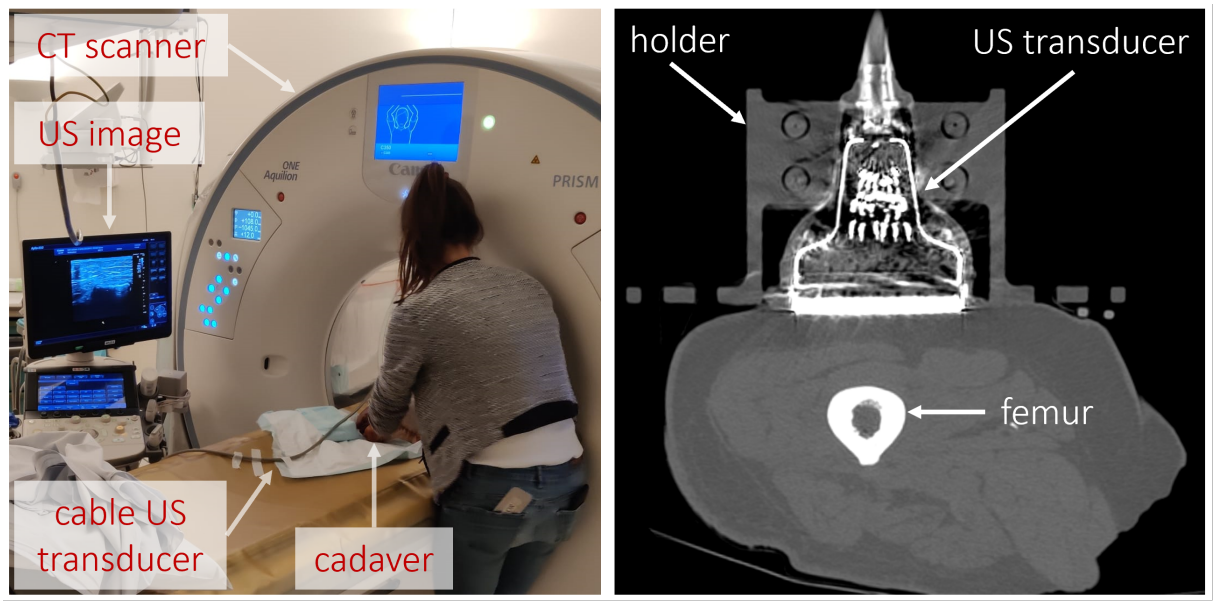

Figure 5.2: Setup of the experiment. The US device stood next to the CT scanner, and CT scans were made of the complete cadaver including the US transducer. In this way, simultaneous measurements could be made. The image on the right shows how the holder with the US transducer was attached to the human cadaver and the corresponding CT scan.

In between the measurements, the position and orientation of the US transducer were varied to investigate the influence of different geometries of the bone surface on its appearance in the US images. Therefore, measurements were taken around the femoral midshaft, the lateral, and the medial epicondyle. In eight measurements, the inclination angle between the skin and the US transducer was around 90°. In three measurements, this inclination angle was varied to evaluate its effect on the bone thickness appearing in the US images.

After positioning the holder and the linear US transducer, a radiologist specialized in musculoskeletal imaging optimized the US image settings. With the US scanner, a video of 30 seconds was recorded while the CT scan was made. The first and last image of this 30-second video were compared to see if the US transducer did not move during the CT scan. If this was not the case, the first image was used for analysis. An overview of this analysis is given in Figure 5.3.

5.2.1 Analysis

Both US and CT images could be compared since the CT scan showed the orientation and translation of the US transducer. For comparison of CT and US images, all measured information from the CT scan and the US transducer were expressed in one global coordinate system, as Figure 5.3 shows. The following paragraphs explain how this was done. MATLAB was used for this post-processing procedure.

First, the usable information of the CT scan was converted to the global coordinate system. Therefore, the femur was automatically segmented in the CT scans using a trained convolutional neural network [85]. Manual adjustments were made at the distal femur to ensure accurate bone surface segmentations. This segmentation was interpolated and smoothened in 3 iterations using Laplacian smoothing (which takes the inverse distances as weights for smoothing the mesh surface [86]).

In addition, the US transducer orientation and position from the CT scan was transformed to the global coordinate system. Therefore, the five fiducials placed on the custom-made holder

were segmented from the CT scan data and converted to the global coordinate system as well, as Figure 5.3B shows.

Second, the US transducer scan plane was transformed to the global coordinate system. The scan plane orientation and positioning relative to the US transducer were determined based on the geometry of the US transducer. It was assumed that this scan plane was oriented parallel to the long axis of the US transducer and started at the tip of the US transducer. The 3D image of the US transducer was used to make a mesh containing the exact geometry of the US transducer (accuracy was around 0.1 mm, see appendix D.1.2). A plane constructed of lines was fitted parallel to the long axis of the US transducer mesh in MATLAB. The median of the top surface of the US transducer was taken to determine where the scan plane started. This is shown in Figure 5.3C.

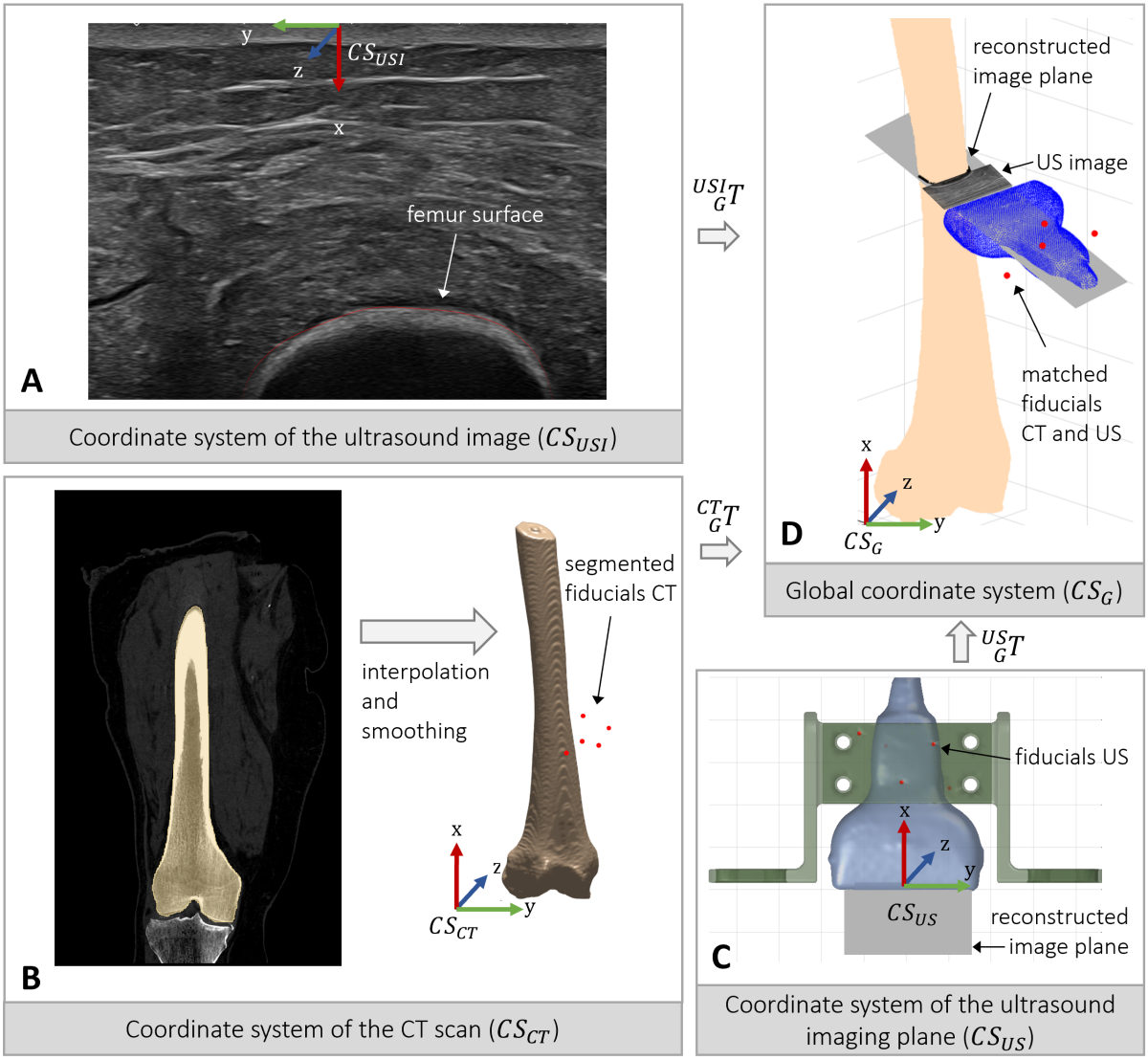

Figure 5.3: Overview of the different transformation steps needed to compare the CT and US bone images. **A)** US image expressed in the image plane coordinate system CS_{IP}. **B)** CT scan in which segmentation of the femur and the five fiducials of the US holder were made, expressed in the CT coordinate system CS_{CT}. **C)** 3D image of the US transducer and the custom-made holder with five fiducials expressed in coordinate system CS_{US}. The US image plane position was determined based on the geometry of the US transducer. **D)** Global coordinate system in which the CT and US images could be compared. All individual coordinate systems were expressed in the same coordinate system using three different transforms.

Since the configuration between the transducer scan plane and the custom-made holder was now known, the five fiducials of the custom-made holder were used to convert the US transducer scan plane to the global coordinate system. This was done via a least-squares fitting between the converted fiducials segmented from the CT scan and these fiducials. With this reconstructed scan plane, it could be determined in the global coordinate system which part of the bone was visualized with US. This was done by determining the intersection locations between the reconstructed image plane and the segmented femur [87].

Third, the US image was converted to the global coordinate system. The bone surfaces in the US images were manually segmented by one person. For these segmentations, it was assumed that the bone surface started at the top of the white appearing line, or, in case this line was absent, right above the transition between the shadow artifact and the above-positioned structures [88]. The US bone segmentation was converted to the global coordinate system by assuming that the US image plane was located at the same position as the reconstructed image plane.

After both the CT and US bone segmentations were converted to the global coordinate system, the bone segmentations made on the CT scan and the US image could be compared to one another. Therefore, the surface registration error was calculated. This is the distance error along the axial axis of the US image or the depth between the skin and the bone surface of both imaging modalities. This error was calculated between the manually segmented US bone segmentations and the smoothened CT segmentations. The difference between both CT and US depths were determined for all 11 measurements and expressed as a median value with a standard deviation for each measurement. The mean measurement inaccuracy error and mean standard deviation of these measurements were used to repeat the combined A- and B-mode simulations of chapter 4 for more representative results.

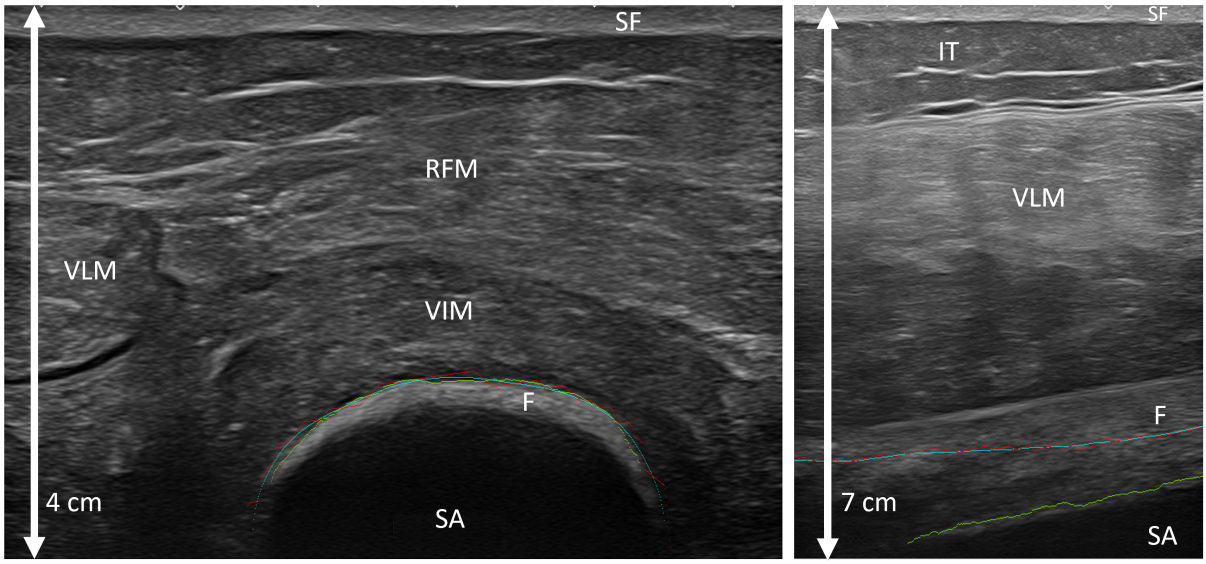

Figure 5.4: Best (left) and worst (right) results shown on US images, being measurement 3 and 7, respectively. In both images, the original CT segmentation is indicated in red, the smoothened CT bone segmentation is indicated in blue, and the US bone segmentation is indicated in green. The total imaging depths are 3 and 7 cm, respectively. Abbreviations: SF: subcutaneous fat, SA: Shadow artifact, VLM: vastus lateralis muscle, VIM: vastus intermedius muscle, RFM: rectus femoris muscle, IT: iliotibial tract, F: femur. All measurement results can be seen in appendix D.

Table 5.1: Table showing the bone surface difference between US and CT bone segmentations. A negative value means that the skin-bone distance determined by US was smaller compared to the skin-bone distance determined by the CT scan. In addition, the Root Mean Square Error (RMSE) of the registration between the fiducials is given in the last column. Abbreviations: ant.: anterior, midfem: mid femoral shaft, dist.: distal, lat.: lateral, incl. angle: inclination angle.

Measurement no.	**Scanned area**	**Scan plane**	**Median ± std**	**RMSE registration (mm)**
1	ant. midfem.	transverse	-0.46 ± 1.36	0.934
2		transverse, smaller incl. angle than 2	0.10 ± 0.40	0.337
3		transverse, smaller incl. angle than 3	0.00 ± 0.34	0.450
4	ant. midfem.	transverse oblique	-0.46 ± 0.25	0.241
5		transverse oblique, smaller incl. angle than 4	-0.58 ± 0.74	0.113
6	ant. dist. fem.	transverse oblique	-0.78 ± 0.36	0.323
7	lat. midfem.	coronal	-8.04 ± 1.47	0.256
8	lat. epicondyle	coronal	-0.46 ± 0.97	0.284
9		coronal, different position than 8	-0.64 ± 1.68	0.236
10	med. epicondyle	coronal	-0.13 ± 1.20	0.165
11		coronal, different position than 10	1.37 ± 1.68	0.160
Mean			***-1.17 ± 0.95***	***0.318 ± 0.051***
Mean without no. 7			*-0.47 ± 0.90*	*0.324 ± 0.056*

5.3 Results

In general, the mean surface registration error between CT and US was -1.17 ± 0.95 mm over the 11 measurements. Measurement 7 was seen as an outlier since the US image was not of good quality according to the radiologist. Excluding measurement 7 gave a mean surface registration error of -0.47 ± 0.90 mm. A negative value here means that the distance between the skin and the bone surface measured with US was smaller compared to the skin and the bone surface determined by CT. Notably, the distance between the skin and bone surface estimated in the US images was larger in almost all measurements compared to the CT scans, as Table 5.1 shows. Moreover, the inclination angle did not seem to have a large influence on the bone surface localization angle. Bone surface geometry, conversely, did seem to largely influence the bone surface localization error.

When comparing the actual segmentation shapes of the bone surface, this amount of overlap was seen in most of the measurements, except for measurement 7. The left image of Figure 5.4 shows that the smoothened CT bone segmentation (blue line) has a lot of overlap with the US segmentation (green line). The right image of Figure 5.4 displays measurement 7, where the least amount of overlap was seen. This measurement was excluded because of the bad US imaging quality.

Moreover, both images display that in US the bone appears as a thick white line, but the thickness of this line differs per measurement location. This is visualized in Figure 5.4 as well.

The thickness of the apparent femoral bone line (indicated with an 'F') has a larger diameter in the right figure (which is the anterior mid femoral shaft, transverse scan plane) compared to the left figure (which is the lateral mid femoral shaft, coronal scan plane). Thus, although measurement 7 was seen as an outlier, it provided information regarding the bone appearance differences in US images.

In addition, the reconstructed CT scan planes were visually compared to the US images. Overall, a lot of overlap between the visualized structures (different muscles, or bone location and shape) and the image planes was seen. The measurement with the most amount of overlap is shown in Figures 5.5 and 5.6. This is measurement 3 in Table 5.1. These figures show that the bone surface is visualized around the same depth in both the US image and the reconstructed CT scan plane image. The checkerboard image shown in Figure 5.5 further highlights the overlaying femoral bone areas visualized with both imaging modalities. The reported RMSE values in Table 5.1 were the mean Euclidean distances between the fiducial holder points and the corresponding points identified in the CT scan images. These RMSE values indicate the registration accuracy between the five fiducials of the custom-made holder in the converted AutoCAD file and the CT scans.

5.3.1 Repeated simulations with found measurement inaccuracy levels

The simulations of chapter 4 with the in-plane measurement inaccuracy of -0.47 ± 0.90 mm were repeated. The results show that the mean measurement inaccuracy is no longer under the required 1 mm and 1°. More than 7 B-modes are no longer sufficient, even if no measurement inaccuracy is present in the position determination of the US transducers. Figure 5.7 show the accuracy results of the simulations.

5.4 Conclusion and Discussion

This chapter aimed to determine the bone surface localization error on US images. This was done by comparing the bone surface segmentations of simultaneously made CT and US images. The results show that overall, a mean bone surface localization error of -0.47 ± 0.90 mm was found when outliers were excluded. This means that the bone surface determined by US imaging was on average located 0.47 mm further away from the US transducer compared to the bone surface depth based on CT imaging. The curvatures of both bone segmentations appear rather similar in both imaging modalities. However, it was challenging to manually estimate the exact bone surface location in the US images, especially since the bone appearance on US

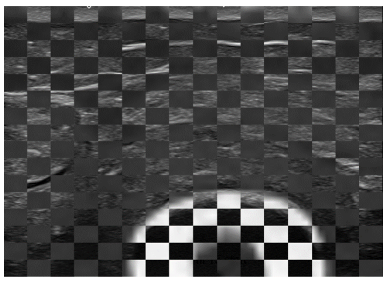

Figure 5.5: Checkerboard image of US and CT images corresponding with measurement 3 from Table 5.1. Good overlap is seen between the bone surface edge between both CT and US images.

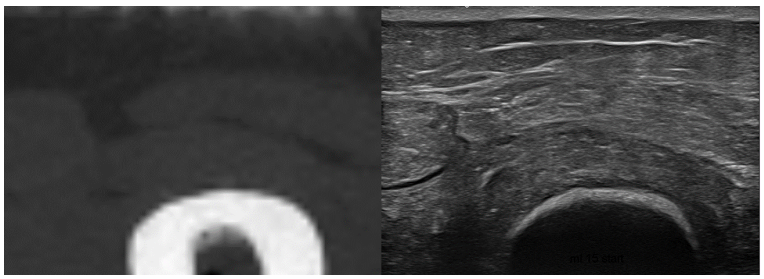

Figure 5.6: Montage of US and CT images corresponding with measurement 3 from Table 5.1. In both images, the quadriceps muscle and the vastus lateralis muscle (indicated in the left image of Figure 5.4) can be distinguished in both images, further indicating the CT scan plane is correctly reconstructed.

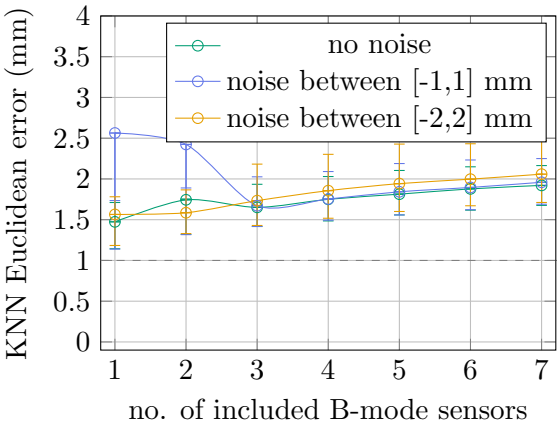

(a) KNN Euclidean error

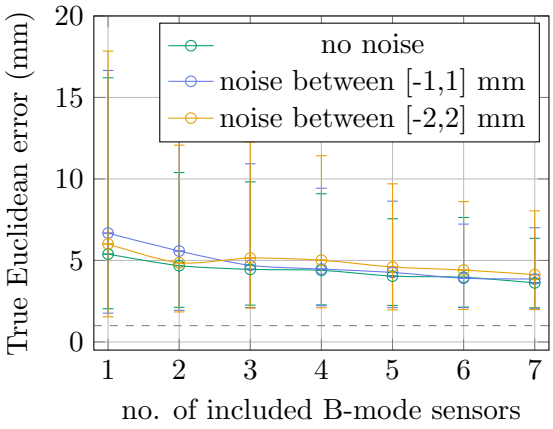

(b) True Euclidean error

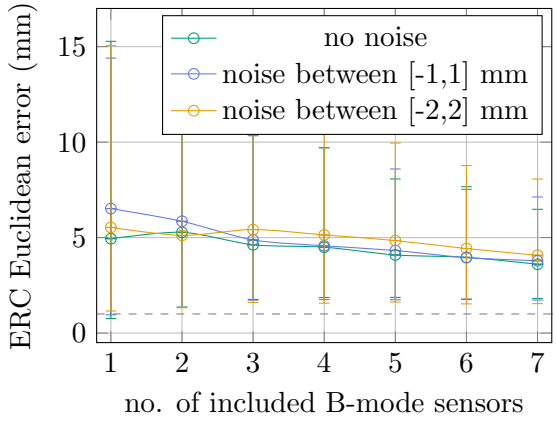

(c) ERC Euclidean error

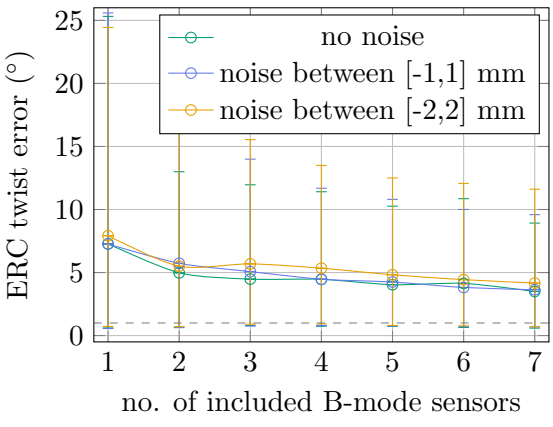

(d) ERC twist error

Figure 5.7: noise levels for B-mode simulations with more accurate B-mode noise levels.

images varies among US images. Therefore, the found mean bone localization error is subject to variability and largely depends on the geometric characteristics of the bone surface that is visualized. Future research should focus on developing algorithms to compensate for the existing surface localization error and the development of a standardized method for determining the bone surface in US images.

Overall, US images taken from the same bone surface under slightly different inclination angles showed similar error results and similar bone appearances on the US images. For example, measurements 1, 2, and 3 shown in Table 5.1 were made under the same conditions, only the inclination angle of the US transducer was varied. Table 5.1 shows that these measurements differed by 0.5 mm, which is within the range of the CT voxel dimensions ($0.625 \cdot 0.625$ mm in the image plane, 0.30 mm in the elevational direction). Similarly, measurements 4 and 5 were taken at the same position as well and differed 0.12 mm.

However, larger variations in the bone surface localization error were introduced when the transducer position changed and different bone surface geometries were imaged. This error seemed to increase specifically when the bone surface became more curved in the elevational direction (see the middle image in Figure 3.1). As an illustration, the right image in Figure 5.4 shows a thick femoral bone response. this is an over-projection of the three-dimensional volume that is imaged by the US transducer and displayed as a two-dimensional image. This effect was described by Jain et al. in 2004 [60].

Quantification of the actual bone surface locations on US images in these cases is a difficult and challenging process. It is something multiple papers researching automatic bone segmentations reported to struggle with [88]. Some articles assumed that the bone surface was always located at the top of the thick white appearing line in the US images [88], [89]. However, according to the theory of Jain et al. [60], in the case of a flat underlying bone surface, the bone surface is most likely located at the top of the white appearing line. The more the bone surface is tilted in the elevational direction of the US transducer (as visualized in Figure 3.1 of Appendix), the bone surface is more likely to be located towards the middle of the thick white appearing line. Therefore, they used a Bayesian probabilistic framework to estimate the bone surface localization.

This theory may explain the large bone surface localization error that was found in measurement 7. Although this measurement was seen as an outlier since the rest of the US image was too blurry and of bad quality, it does reveal an interesting perspective regarding the bone surface location within the US images. In measurement 7, the assumption of the bone surface being located at the top of the white appearing line was incorrect. Further analysis of the CT scan for this particular measurement revealed that the bone surface in the elevational direction of the US transducer was steep, seemingly causing a thicker bone layer appearance in the US image. According to the theory of Jain et al. [60], it would more logical to assume the bone surface is located in the middle of this thick white line in case of a steep bone surface. This is what the CT segmentations in the right image of Figure 5.4 indicate as well. The other measurement locations did not have such a large bone surface slope in the elevational direction of the US transducer. Therefore, the assumption of the bone surface being located at the top of the white appearing bone lines was more accurate. This assumption resulted in smaller bone surface localization errors.

In literature, multiple distance metrics are used to validate the accuracy of the US bone segmentation, making fair comparisons between the found bone surface localization errors difficult [66]. Moreover, in literature US images are registered to the CT images using optical tracking and a point-to-point registration method to determine the transformation between CT and US images. It remains challenging to take the inaccuracy caused by using the optical tracking and

point-to-point registration method into account when comparing both imaging modalities [88]. The added value of the measurement setup presented in this chapter is that the CT scan exactly shows where the US transducer was located during the measurement and that measurements are taken simultaneously under the same circumstances. Therefore, the registration error may not have affected the bone surface localization error as much compared to when a fiducial-based registration technique in combination with a tracking technique was used.

Limitations

Still, there are limitations of this study that should be considered. First, a limited number of measurements were performed during the experiment. These measurements provide valuable insight into the bone surface visualization differences among US images. However, more measurements at different positions are needed to evaluate whether the thick appearing bone line is caused by the inclination angle and/or the bone surface geometry.

Second, a human cadaver was used for these measurements. This cadaver was at least five years old and was at least three times frozen and thawed again. This meant that soft tissue structures were slightly different and the water percentage in the cadaver was lower compared to the water percentage in a normal human lower limb. This could be an explanation for the found underestimation of bone distance by US. Since water has a lower speed of sound, logically this would result in a higher speed of sound in the cadaver tissue than expected by the US device, and therefore an underestimation of the bone distance. In this experiment, an average speed of sound of 1540 m/s was assumed. No corrections were made for each measurement. In case of an underestimation of US of 0.47 mm for a bone that is 30 mm underneath the skin, the corrected speed of sound would be 1564 m/s (see Appendix D.1.1). However, correcting this speed of sound accurately in clinical practice is difficult.

Third, although the US transducer was scanned by the CT scan, determination of the exact positioning and orientation of the US image plane remained somewhat challenging. During the analysis, it was assumed that the US scan plane was oriented parallel to the long axis of the US transducer and started at the tip of the US transducer. However, in reality, each US transducer may have a slightly differently oriented scan plane. This means that the actual scan plane and the reconstructed scan plane may differ slightly. It is estimated that the corresponding error is around half a voxel (0.3125 mm).

Moreover, the orientation and positioning of the reconstructed US image plane were determined by the locations of the five fiducials in the US holder. These locations were manually identified in each CT scan. The mean RMSE values for each measurement given in Table 5.1 indicate that the registration between the fiducials was not perfect in all cases. In combination with the voxel sizes, some unforeseen error could have been introduced here. It is estimated that this error is around half a voxel (0.3125 mm).

Fourth, the accuracy of the bone segmentation from the CT scan is limited by the voxel dimensions ($0.625 \cdot 0.625$ mm in pixel direction, and 0.30 mm in slice direction). Laplacian smoothing was applied to the bone segmentations to correct the segmentation and create a more smoothened bone surface. However, a side effect of this type of filtering is that valuable bone surface information may be removed as well. Although the smoothing provided more overlap between the bone segmentations, it would have been preferred to use the voxel values of the CT scan to make a smoothened bone segmentation. Theoretically, the filtered bone segmentation may miss some local surface texture because of this smoothing. However, it is estimated that this effect is negligible concerning the above-mentioned limitation errors.

In addition, although the automatic segmentation network that was used to segment the

femur gave accurate segmentation results, still some manual adjustments had to be made at irregular parts of the femur. Even though all automatic segmentations were visually checked, it cannot be ruled out that small inaccuracies were still present.

Due to the diameter of bone appearance on the US images, this error is estimated to be around 1 mm. This means that the total estimated error caused by the limitations is around 1.5 mm. This is in the order of magnitude of the mean standard deviation of the measurements.

Implications and recommendations

The results presented in this chapter provide insight into how CT images and US images are related to one another concerning the visualization of the bone surface. This workflow has not been described in any other articles. The added value of the presented workflow is a more accurate comparison between US and CT images since no additional tracking system was used to align both imaging modalities to one another. Therefore, the presented results may give a more accurate estimation of the true bone surface localization error. The reported corrected mean segmentation difference of 0.47 mm lies within the resolution of the voxel sizes and seems promising for using US transducers for bone registration within an intraoperative setting. In addition, the found standard deviation lies within the range of the total estimated error caused by the limitations of the study design.

The presented results seem to indicate that the B-mode in-plane measurement inaccuracy does not have a mean value of 0 mm (as assumed for the sensor model in chapter 4), but has a mean offset of around half a millimeter. A more accurate estimation would be a sensor model assuming normally distributed noise with an offset of 0.47 mm and a standard deviation of 0.90 mm for in-plane measurement inaccuracy. The repeated Monte Carlo simulations show that this offset and standard deviation have a large influence on the overall registration accuracy, and result in a mean ERC Euclidean error of around 4 to 5 mm (see Figure 5.7). This indicates that an assumed mean in-plane measurement inaccuracy of 0 mm used for the simulations in chapter 4 may have provided too optimistic results. Therefore, it is recommended to primarily compensate for the bias. A comparison between Figure 5.7 and 4.13 shows that this effect is larger than the different levels of measurement inaccuracy added to the position of the sensors. Calibrating the measurements and adjusting the speed of sound to a specific measurement location could compensate for this offset. Another option is to use the Bayesian probabilistic framework instead of the described method here for segmenting the bone surface from the US images. Moreover, prior measurements can be used to estimate the measurement location in a Kalman-based filtering approach.

Moreover, the measurements here showed that bone appears as a thick high-intensity line on an US image. As Figure 3.1A showed, the bone response is mainly caused by the fact that a 3D plane is imaged with US. Hence, a more realistic model for the reconstruction of the actual US image plane can be created using a 3D volume instead of a 2D volume for this reconstruction. In this way, the model could better predict where the actual bone surface line lies within the US image.

Before using US for registration of bone in an intraoperative setting, it is recommended to evaluate the bone surface localization error in a dynamic setting. Indeed, it is important to look at the accuracy during tracking. This is needed to keep track of the accurate bone positions after the registration. Preferably, measurements should be made on living humans instead of cadavers to evaluate a more realistic setting.

Moreover, it is recommended to use a Bayesian-based approach for creating a more accurate segmentation of the US images. This approach uses a prior estimate to increase the accuracy of the estimated bone surface. An option to implement this approach is by using a Kalman-based

filter to estimate an accurate weighing between the prior estimate and the current measurement.

The results provide a new way of comparing bone surface detection in US images to CT images. The results show general overlap between both CT and US bone segmentations. This indicates that the used US transducer may be suitable for accurate bone surface identification. More varying measurements and an automatic and accurate segmentation of the bone surface in US images are needed before this technique can be used for intraoperative image registration and tracking.

Part IV

General Conclusion and Discussion

Chapter 6

Conclusion and Discussion

6.1 Conclusion and summary

This thesis focused on finding a new way of aligning a preoperative plan to a patient's anatomy that has more potential to be used by orthopedic surgeons. The introduction of this thesis showed the different views existing in the orthopedic surgery field regarding the execution of a corrective osteotomy, as well as the importance of following a surgical plan within this context. These views show that the potential of such a plan cannot be fully utilized if no suitable tools are available to align the preoperative plan to the patient-specific anatomy. Using a preoperative plan is the first step towards a more accurate way of performing surgery and predicting surgery outcomes better. Current devices such as optical navigation tracking systems or patient-specific saw jigs are available to support using a preoperative plan. However, they are not widely used in orthopedic surgery. A corrective osteotomy around the knee was used as a case study to investigate what is needed to accurately execute this plan in the operation room.

The interviews in chapter 2 of this thesis revealed that corrective osteotomy procedures of the lower limb can be challenging for orthopedic surgeons to perform accurately without the help of an accurate navigation tool that supports executing the surgical plan. During these interviews, lessons were learned about the added value of the registration procedure for using a surgical plan within the operation procedure. Insight was obtained in the requirements a registration technique should meet to make a surgical plan available for the orthopedic surgeon during surgery.

The expected accuracy of the registration technique concerning the US sensor information was further examined in chapter 4. Simulations were performed to determine which type of US sensors were most suitable to use for intraoperative registration of the femoral bone. The results suggest that a combination of A- and B-mode sensors were more robust to measurement inaccuracy and sensor placement. When assuming noise between -1 and 1 mm and no bias present in the in-plane measurement inaccuracy, 6 A-modes and 7 B-mode sensors are needed to meet the set accuracy requirements of 1 mm and 1°. Still, registration accuracy heavily depends on the amount of measurement inaccuracy in the data.

Therefore, chapter 5 focused on determining the bone surface localization error in B-mode US images by comparing these to CT images. Overall, good overlap was seen between the US and corresponding CT images, with a mean bone surface localization error of -0.47 $\pm$ 0.90 mm. However, the mean localization error was found to be subject to variability. This error seemed to depend heavily on the geometric characteristics of the bone surface that is visualized, meaning the localization error is location-dependent. Although this error fell within the limited resolution of the CT scanner (0.625$\cdot$ 0.625 $\cdot$ 0.3 mm), no statements can be made about the sub-millimeter US transducer accuracy beyond this resolution.

The results of the repeated Monte Carlo simulations with the found bone surface localization error of chapter 5 showed that an in-plane offset has a large negative influence on the registration

accuracy. The results showed that 6 A-modes and 7 B-mode sensors lead to a registration accuracy of around 4 mm and 4° instead of 1 mm and 1°.

6.2 Challenges of using ultrasound for registration in clinical practice

A few overall challenges of using US as bone localization tool in clinical practice are worth considering. First, the simulations showed that a **considerable number of sensors is needed to perform an accurate registration**. According to the simulations, at least 6 A-mode sensors and 7 B-mode sensors need to be firmly attached around the femur during surgery. Apart from the time it will take to position the sensors, these sensors should not limit the surgeon in performing the surgery. In addition, simultaneous measuring with a lot of sensors can be challenging. Currently, needing at least 13 sensors for an accurate US registration is clinically not favorable and practical.

Second, in the simulations it was assumed that the position of the US transducers was known to a certain accuracy level. However, in clinical practice **a practical solution must be found to track the US sensors**. Multiple tracking options are listed in Table 6.1. Although optical tracking (reflecting markers attached to the transducer) or a robotic arm fixation (passive robotic arm attached to the transducer) have the lowest localization errors, they may not be practical inside the operation room. In this case, Inertial Measurement Unit tracking without connected cables or the need for maintaining a line-of-sight is desirable. However, this developing technique is currently not accurate enough to use for this application [90].

Third, chapter 5 showed that **an offset present in the B-mode images needs correction**. This can be achieved by adjusting the speed of sound of the US device if needed. Although the CT scan provides information about the type and amount of tissue around the femur, in practice it may be challenging to convert this information to an accurate speed of sound correction [91].

Fourth, **it may be difficult to achieve the required accuracy with the proposed setup**. This thesis focused on obtaining an accurate registration of the femur since this shape is more cylindrical and lacks accessibility to unique geometric features compared to the tibia. Therefore, the femur is in this sense a 'worse case scenario' [69]. Chapter 4 and 5 together showed that different factors mentioned in Figure 3.3 all have their contribution to the total measurement accuracy of the process:

- **Calibration (Fig. 3.3A)**: not calibrating the US sensor may have resulted in an offset of around 0.5 mm (in a human cadaver). In a living human, this offset factor is probably smaller.
- **Sensor measurement and processing (Fig. 3.3B)**: The US segmentation accuracy is approximately around 1 mm. The CT segmentation accuracy is approximately half a voxel, which is around 0.3 mm. The US transducer tracking accuracy was not investigated here but does add inaccuracy to the outcome.
- **Registration (Fig. 3.3C)**: The ICP registration has a mean accuracy of 1 mm and 1°, under the assumptions that the calibration and the sensor measurement and processing phases add a uniform measurement inaccuracy between -1 and 1 mm and no in-plane offset. However, it is plausible that in reality this measurement inaccuracy factor is larger. In that case, the registration accuracy worsens, since the ICP registration does not correct for this measurement inaccuracy.

6.3 Recommendations

The approach in part III of this thesis was to investigate the feasibility of US as a bone localization tool. US holds the potential to perform a registration automatically and is non-invasive. Therefore, it was thought that these advantages may encourage surgeons in the future to perform correction osteotomies more accurately by using a preoperative plan and registration. This thesis provides insight into the practical interpretation of using US for this cause. From this practical point of view, it is recommended that at most 3 B-mode sensors are needed for the registration to make the system still useful and manageable within the operation room. These sensors should not be placed within the surgical field, but preferably one B-mode sensor should be as close to the surgical field as possible. The A-mode sensors are only needed for the global registration. Therefore, these points can also be measured once by collecting the US A-mode measurements with one sensor.

To reduce the number of sensors, it is important to investigate in living human beings whether an offset is present and, if so, what the fastest and most effective way is of calibrating the US sensors. Moreover, it is recommended to apply Kalman-based filtering method as a first step to make the system more robust for measurement inaccuracy. In this way, the prior measurements mentioned in Figure 3.3D are used to correct the bone estimation. A proposal of how this could be implemented is shown in Appendix B.

In addition, current research regarding smaller US transducers in the form of wireless US stickers that provide B-mode images is interesting, as it would make the sensors more manageable and easier to position. This development may be useful in the future for this application if the image quality is proven to be sufficient [98].

Furthermore, investigating manageable and useful options for tracking the US sensors accurately is of paramount importance for application in clinical practice. Therefore, the options mentioned in Table 6.1 are a good start for further investigating this aspect that was outside the scope of this thesis.

The execution of the surgical plan was outside the scope of this thesis as well but is crucial for the accurate execution of a surgical plan. Interesting developments in the field of robotics and orthopedics provide new information on how bone sawing procedures can be made more accurate with robotics. In addition, requirements for such systems and user experiences are reported [99]. This information could be used for further research on the design of a complete system for accurate planning, registration, and execution of corrective osteotomies of the lower limb.

Table 6.1: Overview of reported accuracies of available tracking systems to track the US position.

System	Accuracy	Literature reference
Optical navigation tracking	± 0.55–2 mm	[92]–[94]
Robot arm	± 0.5–1 mm	[95], [96]
Visual tracking	around 1.3 mm	[97]
IMU tracker	$\geq$ 2 mm	[90]

Bibliography

Bibliography

[1] G. D. Dockery, "Surgical principles", in *Lower Extremity Soft Tissue & Cutaneous Plastic Surgery: Second Edition*, Elsevier Ltd., Jan. 2012, pp. 23–27, ISBN: 9780702031366. DOI: 10.1016/B978-0-7020-3136-6.00004-7.

[2] J. C. Barrese and J. M. Henderson, "Image-guided surgery", *Current Problems in Surgery*, vol. 52, no. 12, pp. 476–520, 2015. DOI: 10.1067/j.cpsurg.2015.10.001.

[3] L. Wang, Q. Li, H. Zhao, H. Yuan, and R. Song, "Path planning of robot-assisted osteotomy in orthognathic surgery", *2019 4th IEEE International Conference on Advanced Robotics and Mechatronics, ICARM 2019*, pp. 452–457, 2019. DOI: 10.1109/ICARM.2019.8833971.

[4] A. Hodgson, *5) Robotics in orthopaedic surgery*. Woodhead Publishing Limited, 2012, pp. 90–112. DOI: 10.1533/9780857097392.90. [Online]. Available: http://dx.doi.org/10.1533/9780857097392.90.

[5] G. Zheng, W. Tian, X. Zhuang, and G. Wang, *Intelligent Orthopaedics*. 2018, p. 335, ISBN: 9789811313950.

[6] Royal College of Surgeons, "Future of Surgery", Tech. Rep., 2017.

[7] R. H. Taylor, P. Kazanzides, G. S. Fischer, and N. Simaan, *Medical robotics and computer-integrated interventional medicine*. Elsevier Inc., 2020, pp. 617–672, ISBN: 9780128160343. DOI: 10.1016/b978-0-12-816034-3.00019-5. [Online]. Available: http://dx.doi.org/10.1016/B978-0-12-816034-3.00019-5.

[8] N. Masoumi, C. J. Belasso, M. O. Ahmad, H. Benali, Y. Xiao, and H. Rivaz, "Multimodal 3D ultrasound and CT in image-guided spinal surgery: public database and new registration algorithms", *International Journal of Computer Assisted Radiology and Surgery*, vol. 16, no. 4, pp. 555–565, 2021, ISSN: 18616429. DOI: 10.1007/s11548-021-02323-2. [Online]. Available: https://doi.org/10.1007/s11548-021-02323-2.

[9] A. J. Karkenny, J. R. Mendelis, D. S. Geller, and J. A. Gomez, "The Role of Intraoperative Navigation in Orthopaedic Surgery", *Journal of the American Academy of Orthopaedic Surgeons*, vol. 27, no. 19, E849–E858, 2019, ISSN: 1067151X. DOI: 10.5435/JAAOS-D-18-00478.

[10] H. Gao, S. Hongxun, C. Bin, *et al.*, "Computer-Assisted Orthopedic Surgery", in *Digital Orthopedics*, Springer, Dordrecht, 2018, pp. 333–423, ISBN: 9789402410761. DOI: 10.1007/978-94-024-1076-1.

[11] F. Carrillo, S. Roner, M. V. Atzigen, *et al.*, "An automatic genetic algorithm framework for the optimization of three-dimensional surgical plans of forearm corrective osteotomies", *Medical Image Analysis*, vol. 60, no. 101598, pp. 1–18, 2020, ISSN: 1361-8415. DOI: 10.1016/j.media.2019.101598. [Online]. Available: https://doi.org/10.1016/j.media.2019.101598.

[12] S. Clarke, J. Cobb, M. Jaere, *et al.*, "Osteotomies: Advanced and Complex Techniques", in *ESSKA Instructional Course Lecture Book: Glasgow 2018*, 2018, pp. 129–151, ISBN: 9783662561270. DOI: 10.1007/978-3-662-56127-0.

[13] A. M. Agur and A. F. Dalley, *Grant's Atlas of Anatomy*, 13th ed. 2009, ISBN: 978-1608317561.

[14] T. A. Blackburn and E. Craig, "Knee Anatomy - A Brief Review", *Physical Therapy*, vol. 60, no. 12, pp. 1556–1560, 1980, ISSN: 00026417.

[15] K. Moore and A. Dalley, *Clinically Oriented Anatomy*, 8th ed., 15. 2018, vol. 282.

[16] L. Junqueira and J. Carneiro, "Bot", in *Functionele Histologie*, Reed Business, 2009, ch. 8.

[17] L. Sheehy and T. D. V. Cooke, "Radiographic assessment of leg alignment and grading of knee osteoarthritis: A critical review", *World Journal of Rheumatology*, vol. 5, no. 2, p. 69, 2015, ISSN: 2220-3214. DOI: 10.5499/wjr.v5.i2.69.

[18] M. Stuart, D. Backstein, M. Logan, and T. Muellner, *Osteotomy About the Knee*. 2021, pp. 944–951, ISBN: 9783030490546. DOI: 10.1016/b978-1-4377-1503-3.00096-2.

[19] *Valgus vs Varus - Knee Alignment Difference*. [Online]. Available: https://allhealthpost.com/valgus-vs-varus/ (visited on 03/30/2022).

[20] H. C. Nguyen, W. P. Gielis, N. van Egmond, *et al.*, "The need for a standardized whole leg radiograph guideline: The effects of knee flexion, leg rotation, and X-ray beam height", *Journal of Cartilage & Joint Preservation*, vol. 1, no. 3, p. 100 022, 2021, ISSN: 26672545. DOI: 10.1016/j.jcjp.2021.100022. [Online]. Available: https://doi.org/10.1016/j.jcjp.2021.100022.

[21] D. Paley, *Principles of Deformity Correction*, 3rd ed., J. Herzenberg, Ed. Baltimore, Maryland, USA, 2002, pp. 1–806, ISBN: 978-3-642-63953-1. DOI: 10.1007/978-3-642-59373-4.

[22] M. Nelitz, "Femoral Derotational Osteotomies", *Current Reviews in Musculoskeletal Medicine*, vol. 11, no. 2, pp. 272–279, 2018, ISSN: 19359748. DOI: 10.1007/s12178-018-9483-2.

[23] T. Higuchi, H. Koseki, A. Yonekura, *et al.*, "Comparison of radiological features of high tibial osteotomy and tibial condylar valgus osteotomy", *BMC Musculoskeletal Disorders*, vol. 20, no. 1, p. 409, Dec. 2019, ISSN: 1471-2474. DOI: 10.1186/s12891-019-2764-0. [Online]. Available: https://bmcmusculoskeletdisord.biomedcentral.com/articles/10.1186/s12891-019-2764-0.

[24] T. Minas, *Femoral Varus Osteotomy*, 2016. [Online]. Available: https://musculoskeletalkey.com/femoral-varus-osteotomy/.

[25] J. Harrer, *Osteotomy for torsional deformity (congenital)*, 2021.

[26] R. Thein, B. Haviv, S. Bronak, and R. Thein, "Distal femoral osteotomy for valgus arthritic knees", *Journal of Orthopaedic Science*, vol. 17, no. 6, pp. 745–749, 2012, ISSN: 0949-2658. DOI: https://doi.org/10.1007/s00776-012-0273-1. [Online]. Available: https://www.sciencedirect.com/science/article/pii/S0949265815305704.

[27] M. E. Gitelis, A. E. Weber, A. B. Yanke, and B. J. Cole, *Distal femoral osteotomy*, Second Edition. Elsevier Inc., 2018, pp. 144–151, ISBN: 9780323497404. DOI: 10.1016/B978-0-323-46292-1.00016-2. [Online]. Available: http://dx.doi.org/10.1016/B978-0-323-46292-1.00016-2.

[28] R. van Heerwaarden, S. Scröter, R. S. Khakha, A. Wilson, D. Pape, and P. Lobenhoffer, "Osteotomies: The Srgical Details You Want to Know", in *ESSKA Instructional Course Lecture Book: Glasgow 2018*, 2018, pp. 1–361, ISBN: 9783662561270. DOI: 10.1007/978-3-662-56127-0.

[29] T. Woodacre, M. Ricketts, J. T. Evans, *et al.*, "Complications associated with opening wedge high tibial osteotomy - A review of the literature and of 15 years of experience", *Knee*, vol. 23, no. 2, pp. 276–282, 2016, ISSN: 18735800. DOI: 10.1016/j.knee.2015.09.018. [Online]. Available: http://dx.doi.org/10.1016/j.knee.2015.09.018.

[30] F. Ferner, C. Lutter, I. Schubert, M. Schenke, W. Strecker, and J. Dickschas, "Perioperative complications in osteotomies around the knee: a study in 858 cases", *Archives of Orthopaedic and Trauma Surgery*, no. 0123456789, 2020, ISSN: 14343916. DOI: 10.1007/s00402-020-03696-w. [Online]. Available: https://doi.org/10.1007/s00402-020-03696-w.

[31] M. Schenke, J. Dickschas, M. Simon, and W. Strecker, "Corrective osteotomies of the lower limb show a low intra- and perioperative complication rate—an analysis of 1003 patients", *Knee Surgery, Sports Traumatology, Arthroscopy*, vol. 26, no. 6, pp. 1867–1872, 2018, ISSN: 14337347. DOI: 10.1007/s00167-017-4566-y.

[32] G. Spahn, "Complications in high tibial (medial opening wedge) osteotomy", *Archives of orthopaedic and trauma surgery*, vol. 124, no. 10, pp. 649–653, 2004, ISSN: 09368051. DOI: 10.1007/s00402-003-0588-7.

[33] D. W. Elson, M. Dawson, C. Wilson, M. Risebury, and A. Wilson, "The UK Knee Osteotomy Registry (UKKOR)", *Knee*, vol. 22, no. 1, pp. 1–3, 2015, ISSN: 18735800. DOI: 10.1016/j.knee.2014.10.004. [Online]. Available: http://dx.doi.org/10.1016/j.knee.2014.10.004.

[34] Y. Fujisawa, K. Masuhara, and S. Shiomi, "The effect of high tibial osteotomy on osteoarthritis of the knee. An arthroscopic study of 54 knee joints", *Orthopedic Clinics of North America*, vol. 10, no. 3, pp. 585–608, Jul. 1979, ISSN: 00305898. DOI: 10.1016/S0030-5898(20)30753-7.

[35] A. Miniaci, F. T. Ballmer, P. M. Ballmer, and R. P. Jakob, "Proximal tibial osteotomy. A new fixation device", eng, *Clinical orthopaedics and related research*, no. 246, pp. 250–259, 1989, ISSN: 0009-921X. [Online]. Available: http://europepmc.org/abstract/MED/2766613.

[36] S. Murphy and R. Jakob, "Tibial osteotomy for varus gonarthrosis: indication, planning, and operative technique", *Instr Course Lect*, vol. 41, pp. 87–93, 1992.

[37] N. Agarwal, K. To, S. McDonnell, and W. Khan, "Clinical and Radiological Outcomes in Robotic-Assisted Total Knee Arthroplasty: A Systematic Review and Meta-Analysis", *Journal of Arthroplasty*, vol. 35, no. 11, 3393–3409.e2, 2020, ISSN: 15328406. DOI: 10.1016/j.arth.2020.03.005. [Online]. Available: https://doi.org/10.1016/j.arth.2020.03.005.

[38] G. G. Jones, M. Jaere, S. Clarke, and J. Cobb, "3D printing and high tibial osteotomy", *EFORT Open Reviews*, vol. 3, no. 5, pp. 254–259, 2018, ISSN: 20585241. DOI: 10.1302/2058-5241.3.170075.

[39] J. Victor and A. Premanathan, "Virtual 3D planning and patient specific surgical guides for osteotomies around the knee: a feasibility and proof-of-concept study", *The bone & joint journal*, vol. 95-B, no. 11, pp. 153–158, 2013, ISSN: 20494408. DOI: 10.1302/0301-620X.95B11.32950.

[40] T. Neri, D. Myat, and D. Parker, "The Use of Navigation in Osteotomies Around the Knee", *Clinics in Sports Medicine*, vol. 38, no. 3, pp. 451–469, 2019, ISSN: 1556228X. DOI: 10.1016/j.csm.2019.02.009. [Online]. Available: https://doi.org/10.1016/j.csm.2019.02.009.

[41] N. E. Picardo, W. Khan, and D. Johnstone, "Computer-Assisted Navigation in High Tibial Osteotomy: A Systematic Review of the Literature", *The Open Orthopaedics Journal*, vol. 6, no. 1, pp. 305–312, 2012, ISSN: 1874-3250. DOI: 10.2174/1874325001206010305.

[42] S. J. Song and D. K. Bae, "Computer-assisted navigation in high tibial osteotomy", *CiOS Clinics in Orthopedic Surgery*, vol. 8, no. 4, pp. 349–357, 2016, ISSN: 20054408. DOI: 10.4055/cios.2016.8.4.349.

[43] R. Iorio, M. Pagnottelli, A. Vadalà, *et al.*, "Open-wedge high tibial osteotomy: Comparison between manual and computer-assisted techniques", *Knee Surgery, Sports Traumatology, Arthroscopy*, vol. 21, no. 1, pp. 113–119, 2013. DOI: 10.1007/s00167-011-1785-5.

[44] S. F. Fucentese, P. Meier, L. Jud, *et al.*, "Accuracy of 3D-planned patient specific instrumentation in high tibial open wedge valgisation osteotomy", *Journal of Experimental Orthopaedics*, vol. 7, no. 1, 2020, ISSN: 21971153. DOI: 10.1186/s40634-020-00224-y.

[45] M. Donnez, M. Ollivier, M. Munier, *et al.*, "Are three-dimensional patient-specific cutting guides for open wedge high tibial osteotomy accurate? An in vitro study", *Journal of Orthopaedic Surgery and Research*, vol. 13, no. 1, pp. 1–8, 2018, ISSN: 1749799X. DOI: 10.1186/s13018-018-0872-4.

[46] R. W. Brouwer, M. R. Huizinga, T. Duivenvoorden, *et al.*, "Osteotomy for treating knee osteoarthritis", *Cochrane Database of Systematic Reviews*, vol. 2014, no. 12, 2014, ISSN: 1469493X. DOI: 10.1002/14651858.CD004019.pub4.

[47] D. E. Bonasia, G. Governale, S. Spolaore, R. Rossi, and A. Amendola, "High tibial osteotomy", *Current Reviews in Musculoskeletal Medicine*, vol. 7, no. 4, pp. 292–301, 2014, ISSN: 19359748. DOI: 10.1007/s12178-014-9234-y.

[48] C. Jin, E. K. Song, A. Santoso, P. S. Ingale, I. S. Choi, and J. K. Seon, "Survival and Risk Factor Analysis of Medial Open Wedge High Tibial Osteotomy for Unicompartment Knee Osteoarthritis", *Arthroscopy - Journal of Arthroscopic and Related Surgery*, vol. 36, no. 2, pp. 535–543, 2020, ISSN: 15263231. DOI: 10.1016/j.arthro.2019.08.040. [Online]. Available: https://doi.org/10.1016/j.arthro.2019.08.040.

[49] Y. C. Kim, J.-H. Yang, H. J. Kim, *et al.*, "Distal Femoral Varus Osteotomy for Valgus Arthritis of the Knees: Systematic Review of Open versus Closed Wedge Osteotomy", *Knee Surgery and Related Research*, vol. 30, no. 1, pp. 3–16, 2018, ISSN: 2234-0726. DOI: 10.5792/ksrr.16.064.

[50] J. Mathews, A. G. Cob, S. Richardson, and G. Bentley, "Distal Femoral Osteotomy for Lateral Compartment Osteoarthritis of the Knee", *Orthopedics*, 1998. DOI: https://doi.org/10.3928/0147-7447-19980401-08.

[51] T. Duivenvoorden, P. van Diggele, M. Reijman, *et al.*, "Adverse events and survival after closing- and opening-wedge high tibial osteotomy: a comparative study of 412 patients", *Knee Surgery, Sports Traumatology, Arthroscopy*, vol. 25, no. 3, pp. 895–901, 2017, ISSN: 14337347. DOI: 10.1007/s00167-015-3644-2.

[52] P. Lobenhoffer, "The Rationale of Osteotomy around the Knee", *Journal of Knee Surgery*, vol. 30, no. 5, pp. 386–392, 2017, ISSN: 19382480. DOI: 10.1055/s-0037-1603755.

[53] M. W. Allen and D. J. Jacofsky, "Evolution of Robotics in Arthroplasty", in *Robotics in Knee and Hip Arthroplasty*, 2019, ISBN: 9783030165932. DOI: 10.1007/978-3-030-16593-2.

[54] I. Hacihaliloglu, "Ultrasound imaging and segmentation of bone surfaces: A review", *Technology*, vol. 05, no. 02, pp. 74–80, 2017, ISSN: 2339-5478. DOI: 10.1142/s2339547817300049.

[55] A. van Oosterom and T. Oostendorp, "Ultrasound", in *Medische Fysica*, 2014.

[56] R. K. Hobbie and B. J. Roth, *Intermediate physics for medicine and biology*. New York, NY: Springer New York, 2007, ISBN: 978-3-319-12682-1.

[57] Z. Yaniv, "Registration for orthopaedic interventions", in *Computational Radiology for Orthopaedic Interventions*, G. Zheng and S. Li, Eds., Cham: Springer International Publishing, 2016, pp. 41–70, ISBN: 9783319234823. DOI: 10.1007/978-3-319-23482-3_3.

[58] J. L. Prince and J. M. Links, "Ultrasound Imaging", in *Medical Imaging Signals and Systems*, 2nd ed., Upper Saddle River: Pearson Prentice Hall, 2015, ch. 10, pp. 335–397, ISBN: 978-0-13-214518-3.

[59] D. Fontanarosa, S. Van Der Meer, J. Bamber, E. Harris, T. O'Shea, and F. Verhaegen, "Review of ultrasound image guidance in external beam radiotherapy: I. Treatment planning and inter-fraction motion management", *Physics in Medicine and Biology*, vol. 60, no. 3, R77–R114, 2015, ISSN: 13616560. DOI: 10.1088/0031-9155/60/3/R77.

[60] A. K. Jain and R. H. Taylor, "Understanding bone responses in B-mode ultrasound images and automatic bone surface extraction using a Bayesian probabilistic framework", *Medical Imaging 2004: Ultrasonic Imaging and Signal Processing*, vol. 5373, p. 131, 2004, ISSN: 16057422. DOI: 10.1117/12.535984.

[61] S. Schumann, "State of the Art of Ultrasound-Based Registration in Computer Assisted Orthopedic Interventions", in *Computational Radiology for Orthopaedic Interventions*, G. Zheng and S. Li, Eds., vol. 23, Springer International Publishing, 2016, ch. Lecture No, pp. 271–297, ISBN: 9783319234823. DOI: 10.1007/978-3-319-23482-3_14.

[62] R. A. Srivatsan, N. Zevallos, P. Vagdargi, and H. Choset, "Registration with a small number of sparse measurements", *International Journal of Robotics Research*, vol. 38, no. 12-13, pp. 1403–1419, 2019, ISSN: 17413176. DOI: 10.1177/0278364919842324.

[63] F. Langlotz, "Potential pitfalls of computer aided orthopedic surgery", *Injury - International Journal of the Care of the Injured*, vol. 35, pp. 17–23, 2004, ISSN: 00201383. DOI: 10.1016/j.injury.2004.05.006.

[64] M. Oszwald, M. Citak, D. Kendoff, *et al.*, "Accuracy of navigated surgery of the pelvis after surface matching with an a-mode ultrasound probe", *Journal of Orthopaedic Research*, vol. 26, no. 6, pp. 860–864, 2008, ISSN: 07360266. DOI: 10.1002/jor.20551.

[65] J. Liu, G. Singh, S. Al'Aref, *et al.*, "Image Registration in Medical Robotics and Intelligent Systems: Fundamentals and Applications", *Advanced Intelligent Systems*, vol. 1, no. 6, p. 1 900 048, 2019, ISSN: 2640-4567. DOI: 10.1002/aisy.201900048.

[66] P. U. Pandey, N. Quader, P. Guy, R. Garbi, and A. J. Hodgson, "Ultrasound Bone Segmentation: A Scoping Review of Techniques and Validation Practices", *Ultrasound in Medicine and Biology*, vol. 46, no. 4, pp. 921–935, 2020, ISSN: 1879291X. DOI: 10.1016/j.ultrasmedbio.2019.12.014.

[67] M. Casper, R. Mitra, R. Khare, *et al.*, "Accuracy assessment of a novel image-free handheld robot for Total Knee Arthroplasty in a cadaveric study", *Computer Assisted Surgery*, vol. 23, no. 1, pp. 14–20, 2018, ISSN: 24699322. DOI: 10.1080/24699322.2018.1519038. [Online]. Available: https://doi.org/10.1080/24699322.2018.1519038.

[68] S. Heger, F. Portheine, J. A. K. Ohnsorge, E. Schkommodau, and K. Radermacher, "A New Approach and Algorithm for Noninvasive, Transcutaneous Registration User-Interactive Registration of Bone with A-Mode Ultrasound", *IEEE Engineering in Medicine and biology Magazine*, no. March/April, pp. 85–95, 2005.

[69] A. Mozes, T.-C. Chang, L. Arata, and W. Zhao, "Three-dimensional A-mode ultrasound calibration and registration for robtic orthopaedic knee surgery", *The international journal of medical robotics and computer assisted surgery*, vol. 6, pp. 91–101, 2010. DOI: 10.1002/rcs294.

[70] P. J. Gonçalves, P. M. Torres, F. Santos, R. António, N. Catarino, and J. M. Martins, "A Vision System for Robotic Ultrasound Guided Orthopaedic Surgery", *Journal of Intelligent and Robotic Systems: Theory and Applications*, vol. 77, no. 2, pp. 327–339, 2015, ISSN: 15730409. DOI: 10.1007/s10846-013-0012-7.

[71] D. C. Barratt, C. S. Chan, P. J. Edwards, *et al.*, "Instantiation and registration of statistical shape models of the femur and pelvis using 3D ultrasound imaging", *Medical Image Analysis*, vol. 12, no. 3, pp. 358–374, 2008, ISSN: 13618415. DOI: 10.1016/j.media.2007.12.006.

[72] G. P. Penney, D. C. Barratt, C. S. Chan, *et al.*, "Cadaver validation of intensity-based ultrasound to CT registration", *Medical Image Analysis*, vol. 10, no. 3 SPEC. ISS. Pp. 385–395, 2006, ISSN: 13618415. DOI: 10.1016/j.media.2006.01.003.

[73] F. Manni, A. Elmi-terander, G. Burström, *et al.*, "Towards Optical Imaging for Spine Tracking without Markers in Navigated Spine Surgery", *Sensors*, vol. 20, no. 3641, pp. 1–17, 2020. DOI: 10.3390/s20133641.

[74] E. C. Chen, T. M. Peters, and B. Ma, "Guided ultrasound calibration: where, how, and how many calibration fiducials", *International Journal of Computer Assisted Radiology and Surgery*, vol. 11, no. 6, pp. 889–898, 2016, ISSN: 18616429. DOI: 10.1007/s11548-016-1390-7.

[75] A. Vicini and M. B. Sabick, "Determination of number and locations of ultrasound sensors needed to accurately track scapular motion in vivo", *Computer Methods in Biomechanics and Biomedical Engineering: Imaging and Visualization*, vol. 8, no. 1, pp. 24–30, 2020, ISSN: 21681171. DOI: 10.1080/21681163.2018.1544933. [Online]. Available: https://doi.org/10.1080/21681163.2018.1544933.

[76] K. Niu, *Ultrasound Based Skeletal Motion Capture - the Development and Validation of a Non-Invasive Knee Joint Motion Tracking Method - Transducer Focus*. 2018, pp. 131–135, ISBN: 9789036544825.

[77] P. Pellikaan, M. M. van der Krogt, V. Carbone, *et al.*, "Evaluation of a morphing based method to estimate muscle attachment sites of the lower extremity", *Journal of Biomechanics*, vol. 47, no. 5, pp. 1144–1150, 2014, ISSN: 18732380. DOI: 10.1016/j.jbiomech.2013.12.010. [Online]. Available: http://dx.doi.org/10.1016/j.jbiomech.2013.12.010.

[78] Y. Chen and G. Medioni, "Object Modeling by Registration of Multiple Range Images", in *Proceedings - IEEE International Conference on Robotics and Automation*, Los Angeles, 1991, pp. 2724–2729. [Online]. Available: https://graphics.stanford.edu/$%5Csim$smr/ICP/comparison/chen-medioni-align-rob91.pdf.

[79] P. J. Besl and N. D. McKay, "Method for registration of 3-D shapes", in *Sensor Fusion IV: Control Paradigms and Data Structures*, P. S. Schenker, Ed., International Society for Optics and Photonics, vol. 1611, SPIE, 1992, pp. 586–606. DOI: 10.1117/12.57955. [Online]. Available: https://doi.org/10.1117/12.57955.

[80] D. L. Miranda, M. J. Rainbow, E. L. Leventhal, J. J. Crisco, and B. C. Fleming, "Automatic determination of anatomical coordinate systems for three-dimensional bone models of the isolated human knee", *Journal of Biomechanics*, vol. 43, no. 8, pp. 1623–1626, 2010, ISSN: 00219290. DOI: 10.1016/j.jbiomech.2010.01.036. [Online]. Available: http://dx.doi.org/10.1016/j.jbiomech.2010.01.036.

[81] MATLAB, *Reducepatch*, 2022. [Online]. Available: https://nl.mathworks.com/help/matlab/ref/reducepatch.html.

[82] S. Billings, H. J. Kang, A. Cheng, E. Boctor, P. Kazanzides, and R. Taylor, "Minimally invasive registration for computer-assisted orthopedic surgery: combining tracked ultrasound and bone surface points via the P-IMLOP algorithm", *International Journal of Computer Assisted Radiology and Surgery*, vol. 10, no. 6, pp. 761–771, 2015, ISSN: 18616429. DOI: 10.1007/s11548-015-1188-z. [Online]. Available: http://dx.doi.org/10.1007/s11548-015-1188-z.

[83] P. Foroughi, E. Boctor, M. J. Swartz, R. H. Taylor, and G. Fichtinger, "Ultrasound bone segmentation using dynamic programming", *Proceedings - IEEE Ultrasonics Symposium*, pp. 2523–2526, 2007, ISSN: 10510117. DOI: 10.1109/ULTSYM.2007.635.

[84] N. Baka, S. Leenstra, and T. van Walsum, "Machine learning based bone segmentation in ultrasound", *Lecture Notes in Computer Science (including subseries Lecture Notes in Artificial Intelligence and Lecture Notes in Bioinformatics)*, vol. 10182 LNCS, pp. 16–25, 2016, ISSN: 16113349. DOI: 10.1007/978-3-319-55050-3_2.

[85] N. Lessmann, *Femur segmentation in CT - Grand Challenge*, 2021. [Online]. Available: https://grand-challenge.org/algorithms/femur-segmentation-in-ct/ (visited on 05/30/2022).

[86] A. Belyaev, "Mesh Smoothing and enhancing. Curvature Estimation", *Mpi-Inf. Mpg.*, pp. 1–2, 2006.

[87] D. Legland, *geom3d - File Exchange - MATLAB Central*, 2009. [Online]. Available: https://nl.mathworks.com/matlabcentral/fileexchange/24484-geom3d (visited on 05/31/2022).

[88] I. Hacihaliloglu, "3D ultrasound for orthopedic interventions", in *Intelligent Orthopedics*, G. Zheng, W. Tian, and X. Zhuang, Eds., 1st ed., vol. 1093, Springer Singapore, 2018, ch. 10, pp. 113–129, ISBN: 9789811313967. DOI: 10.1007/978-981-13-1396-7_10.

[89] J. Kowal, C. Amstutz, F. Langlotz, H. Talib, and M. G. Ballester, "Automated bone contour detection in ultrasound B-mode images for minimally invasive registration in computer-assisted surgery - an in vitro evaluation", *The international journal of medical robotics and computer assisted surgery*, vol. 3, no. April, pp. 341–348, 2007. DOI: 10.1002/rcs.

[90] D. Nam, E. A. Cody, J. T. Nguyen, M. P. Figgie, and D. J. Mayman, "Extramedullary guides versus portable, accelerometer-based navigation for tibial alignment in total knee arthroplasty: A randomized, controlled trial: Winner of the 2013 HAP PAUL award", *Journal of Arthroplasty*, vol. 29, no. 2, pp. 288–294, Feb. 2014, ISSN: 08835403. DOI: 10.1016/j.arth.2013.06.006.

[91] M. A. Masum, M. R. Pickering, A. J. Lambert, J. M. Scarvell, and P. N. Smith, "Multislice ultrasound image calibration of an intelligent skin-marker for soft tissue artefact compensation", *Journal of Biomechanics*, vol. 62, pp. 165–171, 2017, ISSN: 18732380. DOI: 10.1016/j.jbiomech.2016.12.030. [Online]. Available: http://dx.doi.org/10.1016/j.jbiomech.2016.12.030.

[92] M. N. Wang and Z. J. Song, "Classification and analysis of the errors in neuronavigation", *Neurosurgery*, vol. 68, no. 4, pp. 1131–1143, 2011, ISSN: 0148396X. DOI: 10.1227/NEU.0b013e318209cc45.

[93] A. Sorriento, M. B. Porfido, S. Mazzoleni, *et al.*, "Optical and Electromagnetic Tracking Systems for Biomedical Applications: A Critical Review on Potentialities and Limitations", *IEEE Reviews in Biomedical Engineering*, vol. 13, no. c, pp. 212–232, 2019, ISSN: 19411189. DOI: 10.1109/RBME.2019.2939091.

[94] M. Wang, D. Li, and J. Wang, "A review of computer-assisted orthopaedic surgery systems", *The international journal of medical robotics and computer assisted surgery*, vol. 16, no. e2218, pp. 1–28, 2020. DOI: 10.1002/rcs.2118.

[95] T. Uslu, E. Gezgin, S. Özbek, D. Güzin, F. C. Can, and L. Çetin, "Utilization of low cost motion capture cameras for virtual navigation Procedures: Performance evaluation for surgical navigation", *Measurement: Journal of the International Measurement Confederation*, vol. 181, no. April, 2021, ISSN: 02632241. DOI: 10.1016/j.measurement.2021.109624.

[96] G. Cui, H. Zhang, D. Zhang, and F. Xu, "Analysis of the kinematic accuracy reliability of a 3-DOF parallel robot manipulator", *International Journal of Advanced Robotic Systems*, vol. 12, pp. 1–11, 2015, ISSN: 17298814. DOI: 10.5772/60056.

[97] R. Simões, C. Raposo, J. P. Barreto, P. Edwards, and D. Stoyanov, "Visual Tracking vs Optical Tracking in Computer-Assisted Intervention", Tech. Rep., 2018, pp. 1–10.

[98] C. Wang, X. Chen, L. Wang, *et al.*, "Bioadhesive ultrasound for long-term continuous imaging of diverse organs", *Science*, vol. 523, no. July, pp. 517–523, 2022.

[99] C. Batailler and S. Parratte, *The future of robotic TKA surgery - a critical review but positive outlook*, 2021.

[100] D. Legland, *intersectLineMesh3d*, 2011. [Online]. Available: http://matgeom.sourceforge.net/doc/api/matGeom/meshes3d/intersectLineMesh3d.html (visited on 05/01/2022).

[101] J. H. Friedman, J. Bentley, and R. Finkel, "An Algorithm fQr Finding Best Matches in Logarithmic Expected Time", *ACM Transactions on Mathematical Software*, vol. 3, no. 3, pp. 209–226, 1977.

[102] A. Saïed, K. Raum, I. Leguerney, and P. Laugier, "Spatial distribution of anisotropic acoustic impedance assessed by time-resolved 50-MHz scanning acoustic microscopy and its relation to porosity in human cortical bone", *Bone*, vol. 43, no. 1, pp. 187–194, 2008, ISSN: 87563282. DOI: 10.1016/j.bone.2008.02.015.

Appendices

Appendix A

Substantiation of ultrasound choice

In total, six registration techniques were evaluated, and nine requirements were identified that were seen as important. A weighing (first column) was given to each requirement indicating their importance. The six identified techniques were subdivided into four categories:

1. **Acoustic techniques** were based on identification via sound waves.
    - **Ultrasound imaging**
2. **Optic techniques**: identification based on using (hyper)spectral imaging
    - **Infrared imaging**
    - **Visual imaging**
    - **Fiber tracking**
3. **Magnetic techniques**: use the disruption of a magnetic field to identify a sensor's position and orientation
    - **Electromagnetic tracking**
4. **Accerometers** use the difference in acceleration to determine a sensor's position and orientation
    - **Inertial Measurement Units (IMUs)**
5. **Mechanic techniques**: use a rigid fixation to determine the position and orientation of the end-effector (and attached objects)
    - Rigid fixation

Table A.1: Table showing a scoring of each of the investigated registration techniques for the identified important parameters.

		Weight	Acoustic	Optic			Magnetic	Accelerometer	Mechanic
			US	IR	Visual	Fiber tracking	EM	IMU	Fixation
Technical requirements	Accuracy & precision: <0.5 mm	4	0	2	0	1	2	0	2
	Robustness: loose tracking <100 ms	3	2	1	1	2	0	1	2
User requirements	(semi-) independent system usage	1	2	1	2	2	1	1	2
	Intuitiveness of system usage	3	1	1	1	1	1	1	2
	System compatibility	1	0	1	2	2	1	2	2
	Time consumption registration process	2	0	1	2	1	1	2	2
	Wear of system (markers)	1	2	1	2	1	2	1	2
	Movability of surgeons around patient during system usage	3	2	1	1	2	2	2	2
	Costs	1	1	1	2	1	1	2	2
Functional requirements	Evaluation of limb movement	4	2	2	2	2	2	2	0
	System invasiveness	2	2	1	2	2	1	2	1
	Computational expensiveness	2	0	2	1	2	2	1	2
	Technical support and proof of concept trial possible	5	2	1	1	0	2	2	1
	Innovative	5	2	0	2	1	0	1	0
Total score			52	42	50	48	48	51	49

Appendix B

Proposal for the implementation of Kalman filtering for a more accurate registration

The developed sensor model in chapter 4 of this thesis enables predicting how accurate a registration with US sensors can be made and what the covariance is of multiple sources of inaccuracies that contribute to the total accuracy of the system. The influence of the factors that have been investigated in this thesis (number of sensors, A-or B-mode sensor, positioning, and orientation of the sensors) are not extensively researched. More research is needed to gain more insight into the interplay between multiple sources of inaccuracy. An overview of the relationship between different sources of error within a more elaborate sensor model is shown in Figure B.1.

A more elaborate sensor model can be used to make the overall registration algorithm more accurate. For example, the prediction of the sensor model can be used as input for a Kalman filter, that estimates the bone location based on the estimated accuracy of the incoming measurements and the estimated accuracy of the sensor model. The updated 3D bone positions from the Kalman filter can be used as input for the (improved) registration algorithm. The updated 3D bone locations will probably be more accurate than the bone locations purely estimated from the measurement data since in the sensor model the information of all previous measurements is taken into account. Hence, the covariance of the sensor model decreases over time when more measurements are made. Figure B.1 provides an overview of how an US sensor model can be used in combination with Kalman filtering.

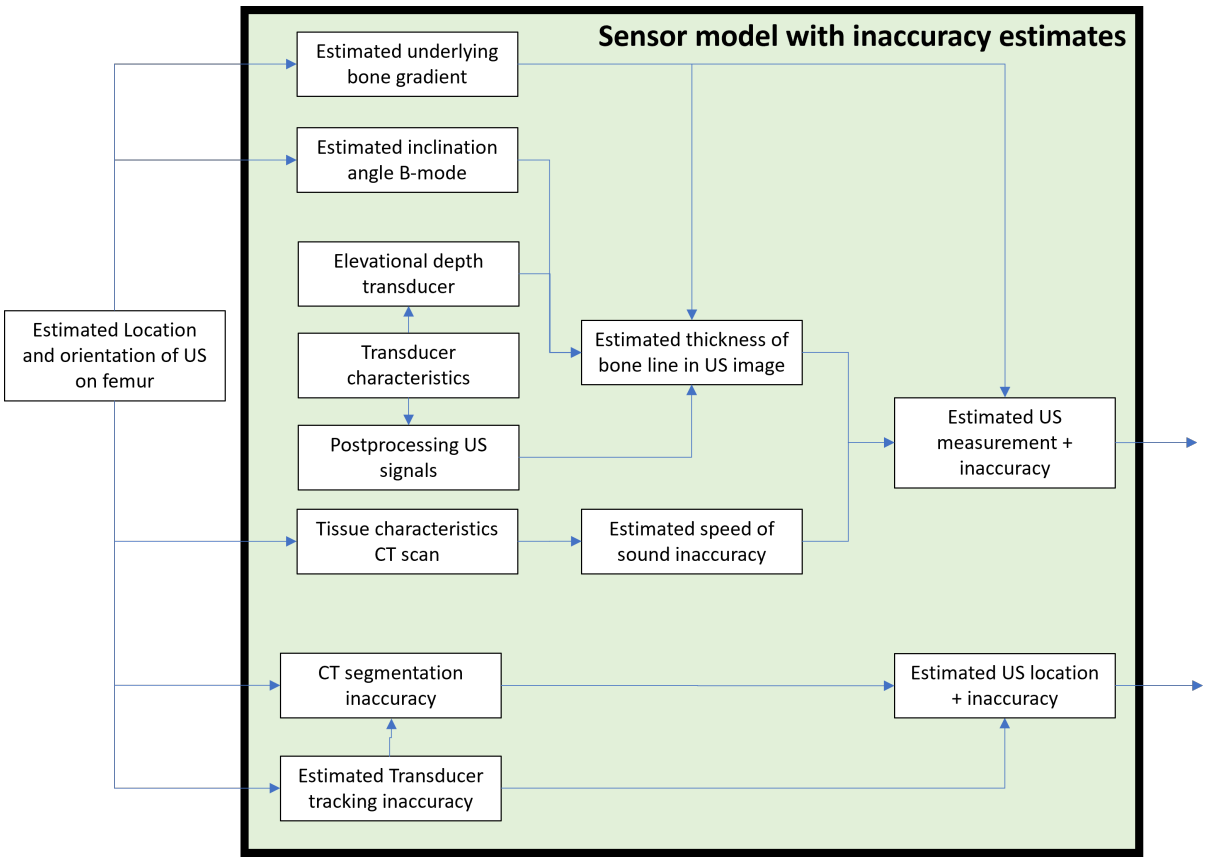

Figure B.1: Detailed overview of parameters needed to model the sensor accurately

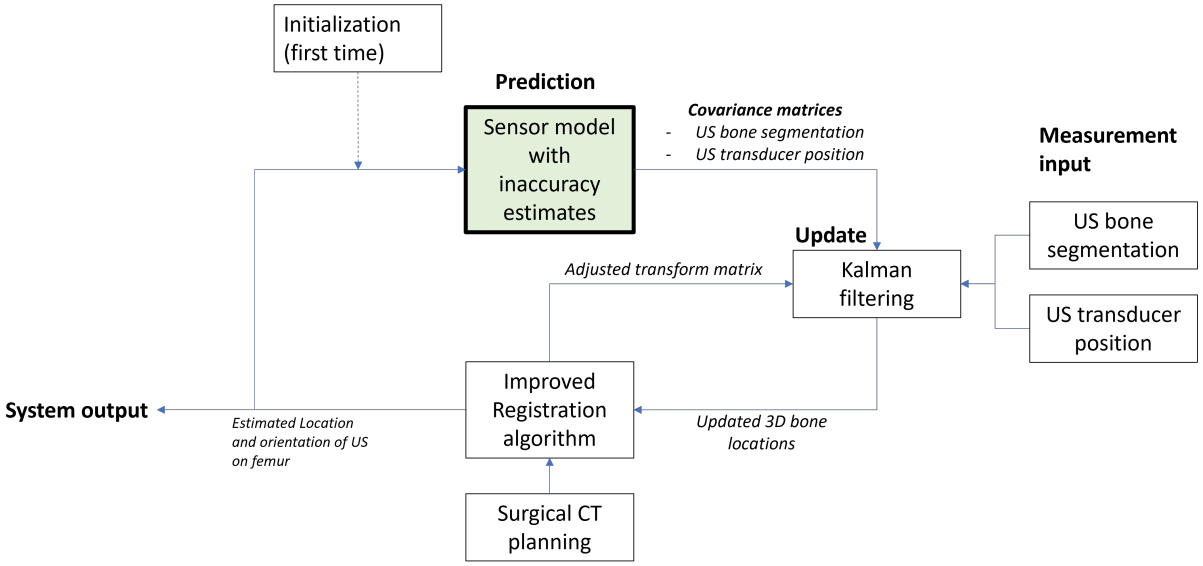

Figure B.2: Overview of using the sensor model in a Kalman filtering-based manner

Appendix C

Additional information for chapter 4

In chapter 4, the US registration procedure was modeled by creating virtual US bone measurements and registering them to a femoral bone model extracted from a CT scan. These simulations consisted of three main steps. First, models of the femoral bone and the US sensors were made and US measurements were modeled using these created models. Second, a virtual registration between these measurements and the original femoral bone was performed. Third, the accuracy of the total registration was evaluated. In the following sections, the first two steps will be explained in more detail and used formulas and algorithms are given.

NB: The superscripts ^{g} and ^{l} mean that the parameter is related to the global or local reference frame, respectively. If this is not explicitly mentioned, the parameter is expressed in the global reference frame.

C.1 Virtual models and measurement selection

Virtual models of the femoral bone and the US sensors were created, and an algorithm was created to select the US measurements. Both the models and the measurement selection are explained in the following sections.

C.1.1 Femoral bone model

A bone model of the femur was made that contained all the areas of the femur that could theoretically be imaged with an US sensor. Therefore, the femoral head, the distal part of the condyles, and the posterior region in between the condyles were excluded from this model.

MATLAB was used for all calculations. A manual CT bone segmentation of a complete femur was used to create a femur mesh. This femur mesh $\mathbf{M}_{femur}$ contained N vertices or points (with x, y , and z coordinates); this point cloud will be referred to as $\mathbf{P}_{femur}$ hereafter. The mesh was shifted such that the origin of the femur mesh was positioned at (0,0,0):

$$\mathbf{P}_{femur0} = \mathbf{P}_{femur} - \frac{\sum_{i=1}^{N} \mathbf{P}_{femur}}{N}$$

The femoral head, the distal condyle region, and the region in between the condyles of the femur were excluded from the mesh because of their inaccessibility with US. Therefore, these regions were selected from the mesh using three spheres with different origins $\mathbf{S}_{origin}$ and radii $\mathbf{S}_{radius}$. These origins and radii were chosen such that the created spheres included the above-mentioned areas. The points of $\mathbf{P}_{femur}$ positioned within the radius $\mathbf{s}_{radius}$ were excluded from

the femoral bone model. In this way, two models were created: the femoral bone point cloud accessible with ultrasound $\mathbf{P}_{accessible}$, and a point cloud with inaccessible locations $\mathbf{P}_{inaccessible}$:

$$\mathbf{P}_{femur0} = \begin{cases} \mathbf{P}_{accessible}, & \text{if } \mathbf{s}_{origin} - \mathbf{P}_{femur0} \geq \mathbf{s}_{radius} \\ \mathbf{P}_{inaccessible}, & \text{otherwise} \end{cases}$$

The complete femur mesh with the created spheres with origins $\mathbf{s}_{origin}$ and radii $\mathbf{s}_{radius}$ are shown as blue spheres in Figure C.1.

C.1.2 A-mode model

For the A-mode model, it was assumed that an A-mode sensor could only measure a *3D bone point*. Therefore, it was assumed that one A-mode sensor could measure one of the points within the accessible femur point cloud $\mathbf{P}_{accessible}$. Measurements with different A-mode sensors resulted in a set of measured points $\mathbf{P}_A$.

Measurement inaccuracy for A-mode was modeled as additive uniformly distributed noise $\mathbf{n}_A$ with a mean of 0 and a standard deviation of 0 mm (no measurement inaccuracy), 1 mm, or 2 mm. This three degrees-of-freedom noise was added to the original measurement location. For one A-mode sensor, this looked as follows:

$$\mathbf{p}_A = \begin{bmatrix} p_{A_x} \\ p_{A_y} \\ p_{A_z} \end{bmatrix} \in \mathbf{P}_{accessible}$$

$$\mathbf{n}_{noise} = \begin{bmatrix} n_{noise_x} \\ n_{noise_y} \\ n_{noise_z} \end{bmatrix}$$

$$\mathbf{p}_{A,noise} = \mathbf{p}_A + \mathbf{n}_{noise}$$

C.1.3 B-mode model

The following assumptions were implemented in the B-mode model. It was assumed that a B-mode sensor could see a *3D bone line*, therefore the B-mode US transducer was modeled as a square with a width of 56.1 mm (in azimuth direction). This square was constructed of lines $\mathbf{L}_B$, as Figure 4.4 shows. These lines had a mutual spacing of 0.5 mm. The measurement points of the B-mode sensor were found by finding the intersection between these constructed lines $\mathbf{L}_B$ and accessible femur mesh $\mathbf{M}_{accessible}$. This was done by using the MATLAB function `intersectLineMesh3d` by David Legland [100]. For each line $\mathbf{l}_B$, this function first calculates the face of the accessible femur mesh where this line intersects. This is done by comparing the line orientation of $\mathbf{l}_B$ to the line orientations of all lines between all vertices and the origin of line point $\mathbf{l}_B$. Then, the intersection distance between the origin of line point $\mathbf{l}_B$ and the face is calculated. Finally, it is checked whether this intersection point lies within the selected face.

In addition, it was checked whether the found intersection points on the femur mesh surface formed one line and not multiple lines (in case of intersection between the $\mathbf{L}_B$ and another part of $\mathbf{M}_{accessible}$. This was done by checking whether the Euclidean distance difference between adjacent line points was beyond a certain threshold of 15 mm. For adjacent points of the line, this distance was usually smaller than 1 mm, therefore a threshold of 15 mm was chosen.

Measurement inaccuracy of B-mode was modeled as two sources: a three degree-of-freedom position error of the B-mode transducer position (similar to $\mathbf{n}_{noise}$), and an in-plane B-mode

error The in-plane B-mode error is shown in Figure 4.4 as measurement noise in the x-direction of the displayed coordinate system. Both sources were assumed to be additive. The in-plane B-mode error was modeled as additive Gaussian noise with a mean of 0 mm and a standard deviation of 1 mm in chapter 4 and a mean of -0.47 mm and standard deviation of 0.90 mm was used in chapter 5.

$$ {}^{l}\mathbf{n}_{in-plane} = \begin{bmatrix} p_{b_x} \\ 0 \\ 0 \end{bmatrix} $$

$$ {}^{g}\mathbf{P}_{B,noise} = {}^{g}\mathbf{P}_{B} + {}^{g}\mathbf{n}_{noise} + {}^{g}_{l}\mathbf{R} \cdot {}^{l}\mathbf{n}_{in-plane} $$

C.1.4 Measurement selection

The selection of measurements consisted of two parts: the generation of six A-mode measurements needed for the global registration, and the generation of additional A- or B-mode measurements.

Global A-mode registration measurements
Two A-mode measurements measured at the greater trochanter, the lateral and medial condyle (the coarse registration areas) were used for the global overlay between the measurements and the femur bone model during the coarse registration. These coarse registration areas ($\mathbf{P}_{coarse}$) were created similarly with spheres as the inaccessible areas, and are shown in Figure C.1.

In total, six A-mode measurements were selected from these coarse registration areas:

$$ \mathbf{P}_{A,coarse} \in \mathbf{P}_{coarse} $$

Measurement inaccuracy was added to these points the same way as for the A-mode model.

Additional A-mode measurements
In addition, zero to 34 additional A-mode measurements were modeled by selecting random points $\mathbf{P}_{A,additional}$ from $\mathbf{P}_{accessible}$.

Additional B-mode measurements
In case of additional B-mode measurements, one to seven additional B-mode measurements were modeled. For the positioning of the B-mode sensor, a point from $\mathbf{P}_{accessible}$ was randomly selected. The center of the B-mode image plane was positioned perpendicular to this selected 3D point $\mathbf{p}_{B,center}$. This means that the x-axis of Figure 4.4 was positioned parallel to the normal vector of the selected 3D point). The rotation of the image plane around the x-axis of Figure 4.4 was randomly chosen.

When multiple B-mode transducer measurements were simulated, the mutual distance between all $\mathbf{P}_{B,center}$ was at least 30 mm. Moreover, the mutual rotation of the image plane around the x-axis of Figure 4.4 for the transducers was chosen such that the orientations of the transducers differed as much as possible. Thus, if n transducers were included, the mutual difference between the orientation angle of each transducer was equal to:

$$ \frac{180^\circ}{n} $$

In total, the modeled US measurements $\mathbf{P}_{US}$ consisted of either only A-mode or a combina-

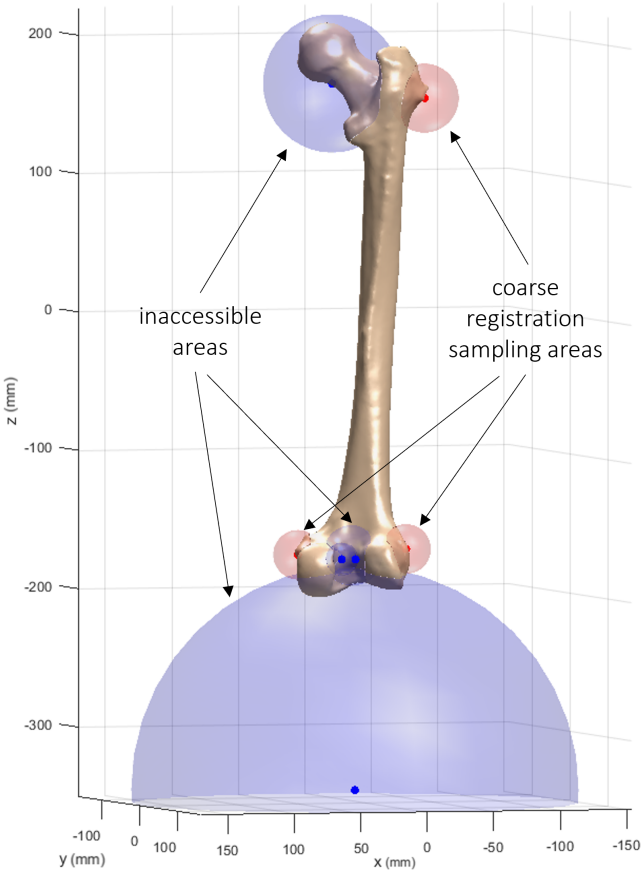

Figure C.1: Creation of the virtual bone measurement model. The bone surface areas that were not measurable by ultrasound (femoral head, distal part of the condyles, area between the femoral condyles) are marked here with blue 3D spheres. The bone surface areas corresponding to the coarse registration sampling areas (trochanter major, lateral and medial epicondyle) are indicated with red 3D spheres. The femoral bone mesh parts located within the blue and red spheres were seen as inaccessible areas and coarse registration areas, respectively.

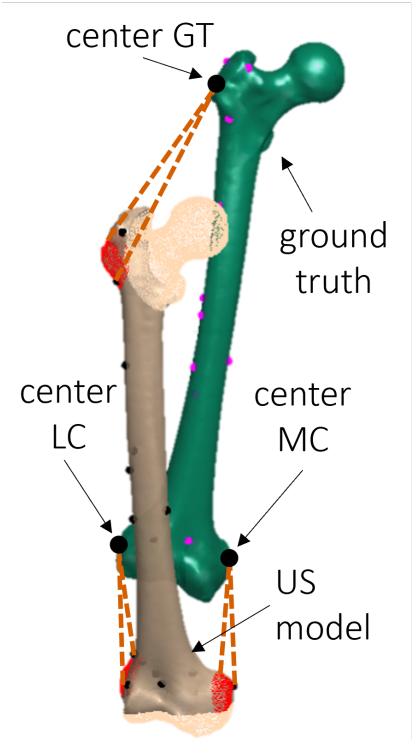

Figure C.2: Figure showing the registration principle. The dotted (orange) lines indicate how sampled points from the coarse registration areas $\mathbf{P}_{A,coarse}$ from the US point cloud are registered to the (black) centers of the coarse registration areas $\mathbf{P}_{coarse,centers}$ of the ground truth point cloud. Abbreviations: GT: greater trochanter, MC: medial condyle, LC: lateral condyle, US: ultrasound.

tion of A- and B-mode measurements:

$$\mathbf{P}_{US} = \begin{bmatrix} \mathbf{P}_{A,coarse} \\ \mathbf{P}_{additional} \end{bmatrix}$$

$$\mathbf{P}_{US} = \begin{cases} \begin{bmatrix} \mathbf{P}_{A,coarse} \\ \mathbf{P}_{A,noise} \end{bmatrix}, & \text{in case of A-mode selection} \\ \begin{bmatrix} \mathbf{P}_{A,coarse} \\ \mathbf{P}_{B,noise} \end{bmatrix}, & \text{in case of B-mode selection} \end{cases}$$

C.1.5 Registration

The registration existed of four steps, as Figure 4.5 shows. A more elaborate explanation of each of these steps is given below.

C.1.6 Initialization

First, an initial alignment difference between US measurements $\mathbf{P}_{US}$ and femur point cloud $\mathbf{P}_{femur}$ had to be made. Therefore, a random transformation matrix was generated. This matrix had a maximum rotation angle of $R_{max} = 45°$ and a maximum translation distance of $t_{max} = 100$ mm. To sample uniform rotation angles as much as possible, a random quaternion angle was generated:

$$\mathbf{q}_{tot} = \begin{bmatrix} q_0 & q_1 & q_2 & q_3 \end{bmatrix}$$

containing the scalar and vectorial part of the quadruple $\mathbf{q}$:

$$\mathbf{q}_{tot} = q_0 + q_1 i + q_2 j + q_3 k$$

The function `rotmat` in MATLAB turned this into rotation matrix $\mathbf{R}_{random}$ according to Rodriques formula:

$$\mathbf{R}_{random} = \begin{bmatrix} -2q_2^2 - 2q_3^2 + 1 & 2q_0q_3 + 2q_1q_2 & 2q_1q_3 - 2q_0q_2 \\ 2q_1q_2 - 2q_0q_3 & -2q_1^2 - 2q_3^2 + 1 & 2q_0q_1 + 2q_2q_3 \\ 2q_0q_2 + 2q_1q_3 & 2q_2q_3 - 2q_0q_1 & -2q_1^2 - 2q_2^2 + 1 \end{bmatrix}$$

A random transformation was determined by picking three random numbers with four decimals between 0 and 1 called $\mathbf{t}_{random01}$, and multiplying them via:

$$\mathbf{t}_{random} = 2 \cdot \mathbf{t}_{max} \cdot \mathbf{t}_{random01} - \mathbf{t}_{max}$$

The total random transform was:

$$\mathbf{T}_{random} = \begin{bmatrix} \mathbf{R}_{random} & \mathbf{t}_{random} \\ 0 \quad 0 \quad 0 & 1 \end{bmatrix}$$

This quaternion angle was transformed into an angle in degrees via the xyz and zyx decomposition. If both angles of the decomposition fell within the maximum rotation angle range, the transform $\mathbf{T}_{random}$ was used to transform $\mathbf{P}_{femur}$ into its so-called 'ground truth' orientation $\mathbf{P}_{femur,GT}$:

$$\mathbf{P}_{femur,GT} = \mathbf{T}_{random} \cdot \mathbf{P}_{femur}$$

C.1.7 Coarse registration step

The coarse registration was a rigid point-to-point registration. The registration was performed between the six coarse registration A-mode measurements $\mathbf{P}_{A,coarse}$ from the three coarse registration areas, and the three centers of these three areas $\mathbf{P}_{coarse,centers}$. The three centers of the three accessible areas were determined by calculating the center coordinates of each of the point cloud areas $\mathbf{P}_{coarse}$, and finding the closest point to these center coordinates using the KNN algorithm. This principle is shown in Figure C.2. The transformation matrix for this registration ${}^{GT}_{US}\mathbf{T}_{coarse}$ was calculated using Procrustes analysis and the Kabsch algorithm. The general form of the used algorithm is given below:

$$\mathbf{P}_{US,0} = \mathbf{P}_{US} - \frac{\sum_{m=1}^{M} \mathbf{P}_{US}}{M}$$

$$\mathbf{P}_{GT,0} = \mathbf{P}_{GT} - \frac{\sum_{k=1}^{K} \mathbf{P}_{GT}}{K}$$

$$\mathbf{C}_0 = \mathbf{P}_{US,0} \cdot \mathbf{P}_{GT,0}^{T}$$

$$\left[\mathbf{U}, \mathbf{V}\right] = \mathrm{SVD}(\mathbf{C}_0)$$

$${}^{GT}_{US}\mathbf{R}_{coarse} = \mathbf{V} \cdot \begin{bmatrix} 1 & 0 & 0 \\ 0 & 1 & 0 \\ 0 & 0 & \mathrm{sign}(\det(\mathbf{U} \cdot \mathbf{V}^T)) \end{bmatrix} \cdot \mathbf{U}^T$$

$${}^{GT}_{US}\mathbf{t}_{coarse} = \frac{\sum_{k=1}^{K} \mathbf{P}_{GT}}{K} - {}^{GT}_{US}\mathbf{R}_{coarse} \cdot \frac{\sum_{m=1}^{M} \mathbf{P}_{US}}{M}$$

$${}^{GT}_{US}\mathbf{T}_{coarse} = \begin{bmatrix} {}^{GT}_{US}\mathbf{R}_{coarse} & {}^{GT}_{US}\mathbf{t}_{coarse} \\ 0 \quad 0 \quad 0 & 1 \end{bmatrix}$$

During the coarse registration, $\mathbf{P}_{US}$ was substituted with $\mathbf{P}_{A,coarse}$, and $\mathbf{P}_{GT}$ was substituted with $\mathbf{P}_{coarse,centers}$.

C.1.8 ICP registration step

The ICP registration was performed next. This was a rigid point-to-point registration algorithm as well (similar to the Coarse registration). The only difference was that here the transformation matrix was calculated multiple times. This was done until the root-mean-square difference between the two point clouds was under a certain threshold (10^{-3}), or the maximum number of iterations (30) was reached.

For the ICP registration, $\mathbf{P}_{US}$ consisted of *all* US measurements. During every iteration, these points were matched to the then closest neighbor points of the ground truth femur model using the KNN algorithm [101]. $\mathbf{P}_{GT}$ consisted of these matched points. This means that during every iteration, the matched points could differ. Algorithm 1 shows the pseudocode of the ICP registration.

C.1.9 Perturbation and extra ICP registration step

For the last step in the registration, the measurement point cloud $\mathbf{P}_{US}$ was systematically rotated between -5 and 5° around the z axis (axis along the long axis of the femoral bone) and translated between -3 and 3 mm in z direction (up-down direction of the femur). The algorithm that was used to determine $\mathbf{T}_{perturbation}$ is shown in Algorithm 2.

The total transform $\mathbf{T}_{tot}$ was calculated by:

$${}^{GT}_{US}\mathbf{T}_{tot} = {}^{GT}_{US}\mathbf{T}_{perturbation} \cdot {}^{GT}_{US}\mathbf{T}_{ICP} \cdot {}^{GT}_{US}\mathbf{T}_{coarse}$$

Algorithm 1: ICP registration

Compute $\mathbf{P}_{US,0}$, $\mathbf{P}_{GT,0}$;
$\mathbf{P}_{US} = \mathbf{P}_{US,0}$;
$\mathbf{P}_{GT} = \mathbf{P}_{GT,0}$;

while *RMSE* $\geq 10^{-3} \vee$ *Number of iteration* > 30 **do**
  for *every* $\boldsymbol{p}_{US,i}$ *in* $\boldsymbol{P}_{US}$ **do**
    $\mathbf{p}_{GT,i}$ = nearest point $\left(\mathbf{p}_{US,i}, \mathbf{P}_{GT}\right)$;
  end for

  $${}^{GT}_{US}\mathbf{T}_{ICP} = \underbrace{\min_{\left({}^{GT}_{US}\mathbf{T}_{ICP}\right)} \mathbf{E}(\mathbf{T}_{ICP}) = \min_{\left({}^{GT}_{US}\mathbf{T}_{ICP}\right)} \sum_{i} \left\| \mathbf{p}_{GT,i} - {}^{GT}_{US}\mathbf{T}_{ICP}(\mathbf{p}_{US,i}) \right\|^2}_{\text{Procrustes analysis and Kabsch algorithm}} ;$$

  $\mathbf{P}_{US}$ = transform point cloud$\left(\mathbf{P}_{US}, {}^{GT}_{US}\mathbf{T}_{ICP}\right)$;

  $RMSE_{ICP}$ = root mean square error$\left(\mathbf{P}_{US}, \mathbf{P}_{GT}\right)$;
  number of iteration = number of iteration + 1;
end while

return ${}^{GT}_{US}\boldsymbol{T}_{ICP}$, $RMSE_{ICP}$

Algorithm 2: Perturbation and ICP registration

Degrees = {-5 -4 -3 -2 -1 0 1 2 3 4 5};
Translations = {-3 -2.5 -2 -1.5 -1.0 -0.5 0 0.5 1.0 1.5 2.0 2.5 3.0};

for *every i in Degrees* **do**
  $\mathbf{R}_{z,i}$ = create rotation matrix of j degrees around z axis ;

  for *every j in Translations* **do**
    $\mathbf{t}_{z,j}$ = create translation vector of j mm in z direction;
    $\mathbf{T}_{z,k}$ = make transform matrix$\big(\mathbf{R}_{z,i}, \mathbf{t}_{z,j}\big)$;
    $\mathbf{P}_{US}$ = transform point cloud$\big(\mathbf{P}_{US}, \mathbf{T}_{z,k}\big)$;

    for *every* $\boldsymbol{p}_{US,i}$ *in* $\boldsymbol{P}_{US}$ **do**
      $\mathbf{p}_{GT,i}$ = nearest point$\big(\mathbf{p}_{US,i}, \mathbf{P}_{GT}\big)$;
    end for

    $RMSE_{i,j}$ = root mean square error$\big(\mathbf{P}_{US}, \mathbf{P}_{GT}\big)$;

  end for
end for

$RMSE_{perturbation}$ = select combination of i and j with lowest $RMSE_{i,j}$;

if $RMSE_{perturbation} <$ $\underbrace{RMSE_{ICP}}_{\text{from Algorithm 1}}$ **then**
  $\big[{}^{GT}_{US}\mathbf{T}_{perturbation}, RMSE_{perturbation}\big] = \underbrace{\text{ICP registration } \big(\mathbf{P}_{US}, \mathbf{P}_{GT}\big)}_{\text{Algorithm 1}}$
else
  ${}^{GT}_{US}\mathbf{T}_{perturbation} = \mathbf{I}_4$;
  $RMSE_{perturbation} = RMSE_{ICP}$;
end if

return ${}^{GT}_{US}\boldsymbol{T}_{perturbation}$, $RMSE_{perturbation}$

Algorithm 3: Overview of Monte Carlo setup

standard deviation of noise = $\{0\ 1\ 2\}$;

number of additional sensors = $\begin{cases} \{1:1:34\}, & \text{in case of A-mode} \\ \{1:1:7\}, & \text{in case of B-mode} \end{cases}$

for *every* i *in* standard deviation of noise **do**
  for *every* j *in* number of additional sensors **do**
    for $k = 1:1000$ **do**
      $\mathbf{P}_{GT}$ = perform random transform$\big(\mathbf{P}_{femur}\big)$;
      $\big[\mathbf{P}_{coarse},\, \mathbf{P}_{accessible}\big]$ = create sample areas$\big(\mathbf{P}_{femur}\big)$;
      $\mathbf{P}_{A,\,coarse}$ = measurement selection$\big(\mathbf{P}_{coarse},\, 6\big)$;
      $\mathbf{P}_{US,\,additional}$ = measurement selection$\big(\mathbf{P}_{accessible},\, j\big)$;
      $\mathbf{P}_{US} = \begin{bmatrix} \mathbf{P}_{A,\,coarse} \\ \mathbf{P}_{US,\,additional} \end{bmatrix}$;
      $\mathbf{P}_{US,\,noise}$ = add noise$\big(\mathbf{P}_{US},\, i\big)$;
      $\big[{}^{GT}_{US}\mathbf{T}_{tot,ijk},\, RMSE_{tot,ijk}\big] = \underbrace{\text{perform registration}\big(\mathbf{P}_{US,\,noise}, \mathbf{P}_{GT}\big)}_{\text{Coarse registration, Algorithm 1 and 2}}$;
    end for
  end for
end for
return ${}^{GT}_{US}\boldsymbol{T}_{tot},\, RMSE_{tot}$

C.2 Additional results

Additional figures to chapter 4 are shown below.

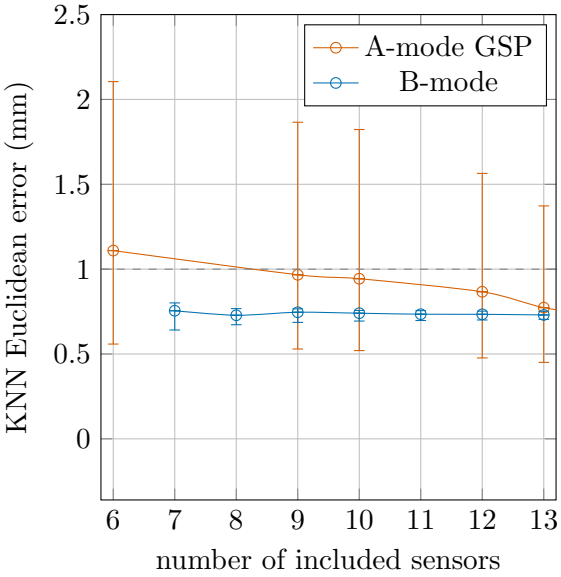

(a) KNN Euclidean error

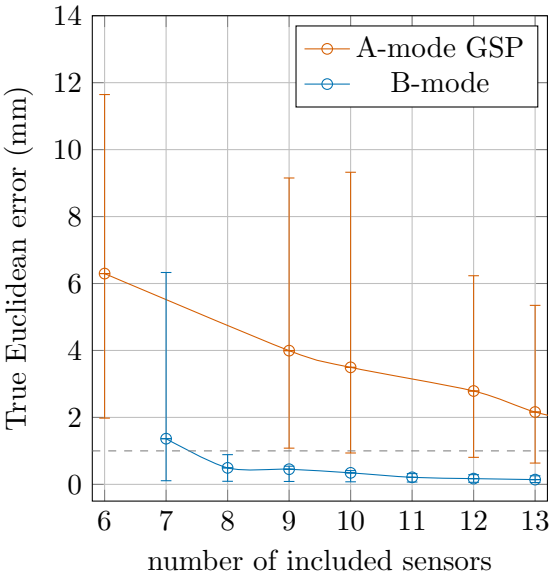

(b) True Euclidean error

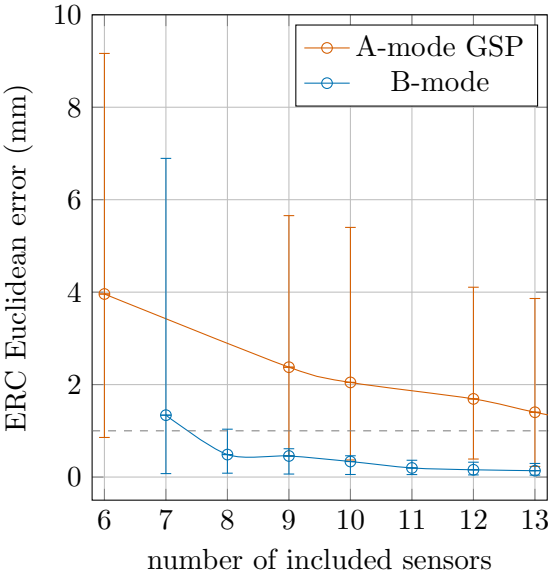

(c) ERC Euclidean error

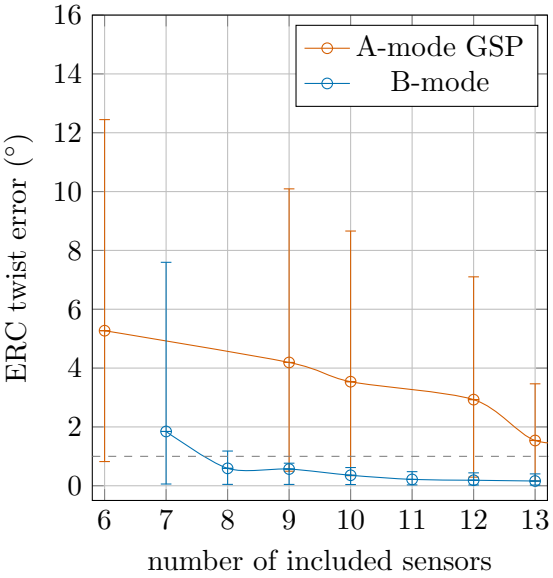

(d) ERC twist error

Figure C.3: Localization errors for A-mode placed according to GSP placement and a combination of A- and B-modes (six A-modes and one to seven B-mode sensors). The lines show the mean values of the localization error per number of included sensors, the colored areas contain 90% of the data. Here, no additional measurement inaccuracies were added.

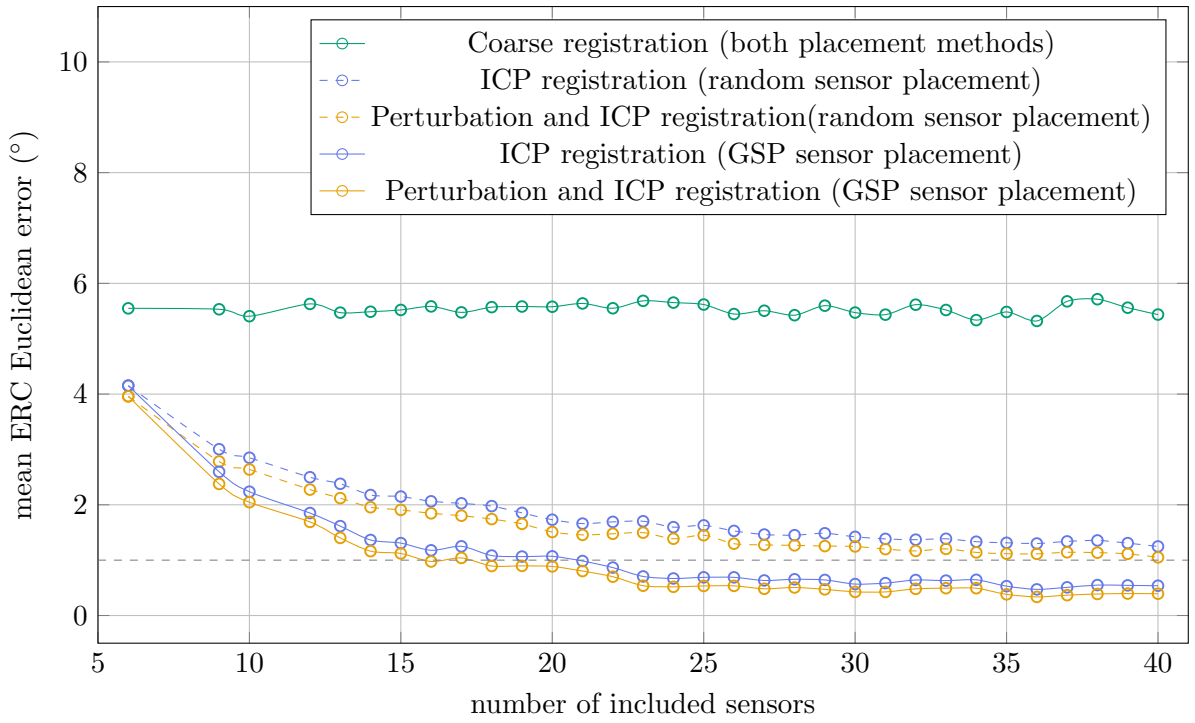

Figure C.4: Accuracy after every registration step as mentioned in Figure 4.5 for both random (dashed lines) and GSP (solid lines) sensor placement. Since for the coarse registration the same sensor positions and initial transform were used, no extra dashed line is shown there. It can be seen that during every registration phase the GSP sensor positioning has lower mean ERC Euclidean errors compared to random sensor positioning.

Appendix D

Additional information to chapter 5

D.1 Acoustic Impedance for different parts of bone

As chapter 5 describes, the amount of reflected ultrasound waves depends on the acoustic impedance of a certain tissue. The bone can be subdivided into two types of tissue: the periosteum or peripheral cortical layer(connective tissue around the bone) and the endosteum or internal cortical layer (the underlying bone). Saied et al. [102] found that the internal cortical layer had slightly higher acoustic impedance values compared to the peripheral cortical layers. They also saw that the acoustic impedance differed slightly between different bone areas, and between different specimens. Figure D.1 shows some of their results that were obtained with advanced equipment. These results underline that the difference between the periosteum and the underlying bone will most likely not be detectable by normal US sensors.

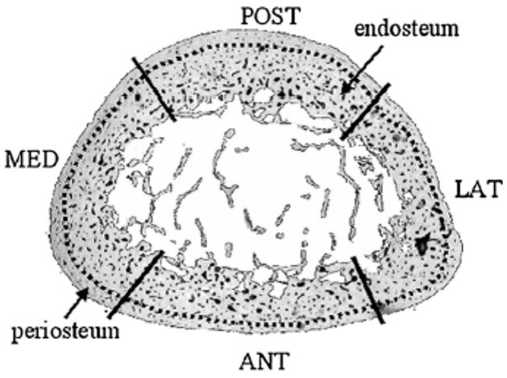

	Po (%)	N.Ca (mm^{-2})	Ca.Dm (μm)	Z (Mrayl)
POST PER	2.7±0.6	7.1±1.0	53.5±4.3	7.74±0.21
LAT PER	2.6±0.5	6.8±1.1	62.5±4.0	7.88±0.17
ANT PER	2.3±0.4	6.6±1.0	54.5±3.1	8.14±0.17
MED PER	2.4±0.5	6.4±1.0	56.4±4.2	7.95±0.22
POST END	9.1±1.0	11.2±1.0	74.5±3.4	8.12±0.16
LAT END	8.9±0.9	10.2±0.9	73.1±2.6	8.21±0.16
ANT END	8.5±0.9	9.4±0.85	78.6±3.8	8.27±0.16
MED END	8.2±0.7	8.5±0.7	79.8±4.2	8.15±0.22
ANT PER 90°[a]	–	–	–	6.63±0.09
ANT END 90°[a]	–	–	–	6.73±0.07

[a] ANT PER 90° and ANT END 90° are the external and internal layers of the anterior cortical portion of the longitudinal sections, respectively.

	Peripheral cortical layer			Internal cortical layer		
Specimen #	Z_3	Z_1	AR_Z	Z_3	Z_1	AR_Z
1	7.72±0.45	6.58±0.57	1.17	7.74±0.46	6.69±0.56	1.16
2	8.23±0.78	6.37±0.66	1.29	8.46±0.80	6.77±0.84	1.25
3	7.79±0.63	6.85±0.54	1.14	8.16±0.64	6.93±0.76	1.18
4	7.37±0.72	6.51±0.65	1.13	7.74±0.70	6.48±0.80	1.19
5	7.46±1.24	6.84±0.66	1.09	7.80±1.32	6.76±0.63	1.15

Figure D.1: Different measured values of acoustic impedance of the Periosteum and Endodosteum [102].

D.1.1 Correction for speed of sound

For the experiments, it was chosen not to correct the speed of sound. The constructed US images assumed a speed of sound v_{US} of 1540 m/s. In literature, often a correction is made for this velocity as it is only a rough estimate of the true speed of sound through human tissue. The speed of sound in fat and muscle is 1450 m/s and 1580 m/s, respectively [61].

The calculation in the discussion of chapter 5 for correction of the speed of sound was made as follows. Imagine the distance between the skin and bone s_{CT} is 30.47 mm according to the

CT scan. If US has a bias of -0.47 mm, the estimated distance measured with US s_{US} is 30 mm. To calculate the needed corrected speed of sound, the travel time t_{US} of the speed of sound wave has to be calculated first.

$$t_{US} = \frac{2 \cdot s_{US}}{v_{US}}$$
$$v_{US} = 1540\ m/s;\ s_{US} = 30\ \ mm$$
$$t_{US} = \frac{2 \cdot 30 \cdot 10^{-3}}{1540}\ m/s$$

Then, the corrected speed of sound $v_{US,corrected}$ should be:

$$v_{US,corrected} = \frac{2 \cdot s_{CT}}{t_{US}}$$
$$s_{CT} = 30 + 0.47\ \ mm$$
$$v_{US,corrected} = \frac{2 \cdot (30 + 0.47) \cdot 10^{-3}}{1} \cdot \frac{1540}{2 \cdot 30 \cdot 10^{-3}}\ m/s$$
$$v_{US,corrected} = 1564\ m/s$$

D.1.2 Ultrasound transducer fitting

As mentioned in the method section of chapter 5, a 3D mesh of the US transducer was used for the custom-made holder. This was done to ensure a tight and unique fitting between the holder and the transducer. Hence, it was important that this 3D mesh accurately represented the US transducer geometry. To check this, multiple 3D photos and 3D meshes were made. These 3D meshes were registered onto each other to check the mutual differences between these meshes. These results showed that the mean mutual differences between the 3D meshes were around 0.1 mm, with local peak differences of 0.8 mm. The comparison between two 3D meshes is shown in Figure D.2.

D.2 All measurement results

In the figures below, all measurement results are plotted. In these figures, the red line is the unfiltered CT bone surface segmentation, the blue line is the interpolated and smoothened CT bone surface segmentation, and the green line is the US bone surface segmentation. This is indicated in Figure D.3, but applies to all figures.

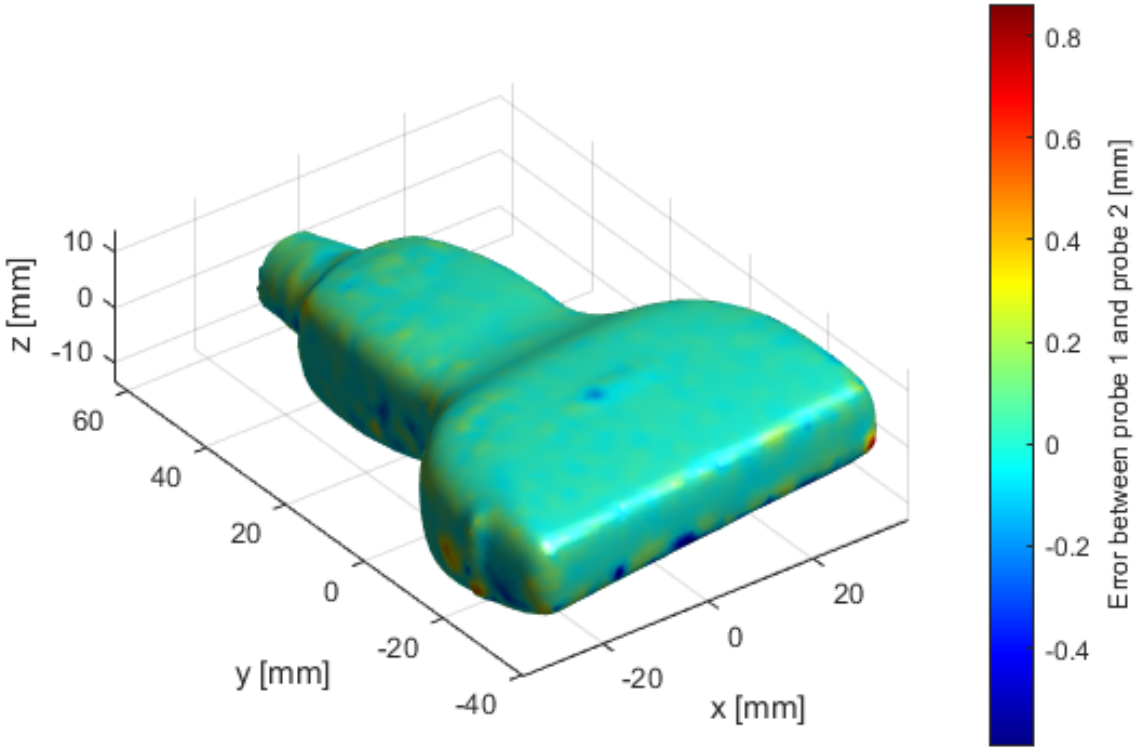

Figure D.2: Figure showing the accuracy of the mesh made from the US transducer. The perpendicular point-to-surface between the meshes is shown in this heatmap image.

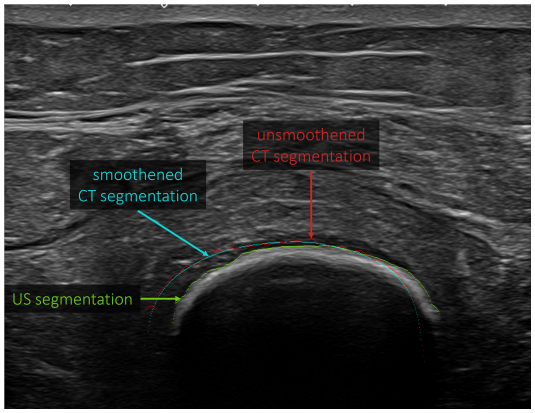

Figure D.3: Measurement 1

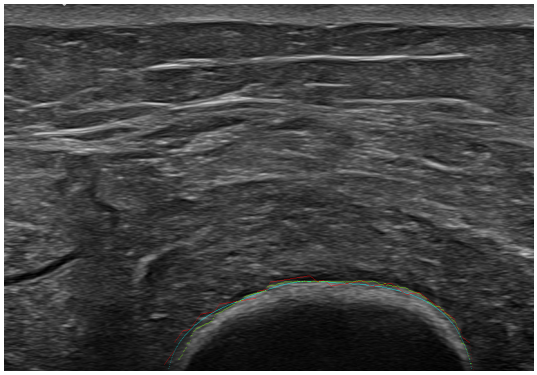

Figure D.4: Measurement 2

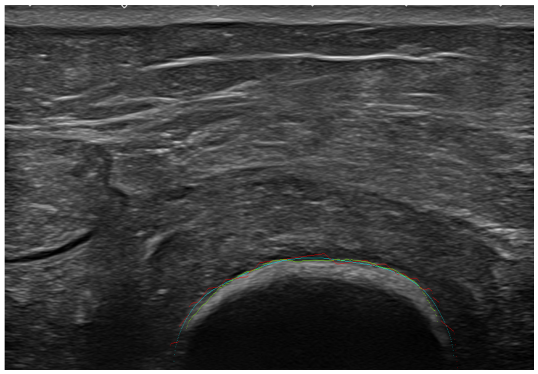

Figure D.5: Measurement 3

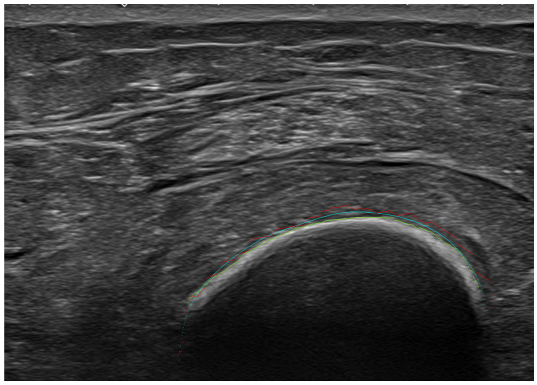

Figure D.6: Measurement 4

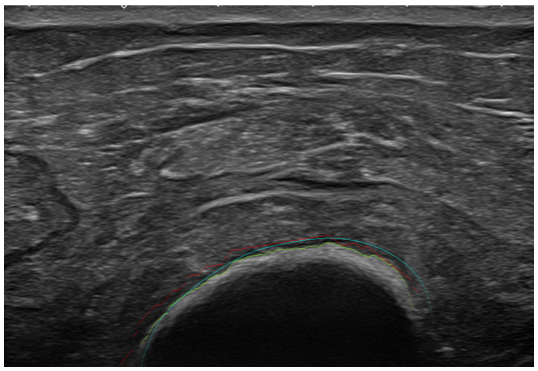

Figure D.7: Measurement 5

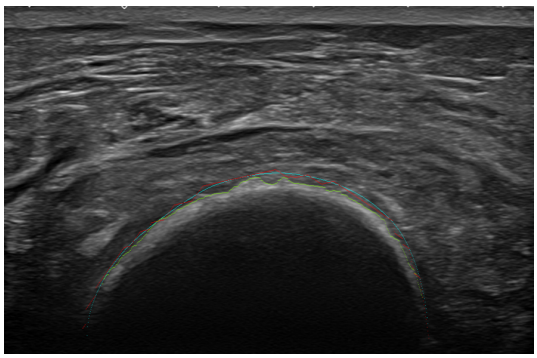

Figure D.8: Measurement 6

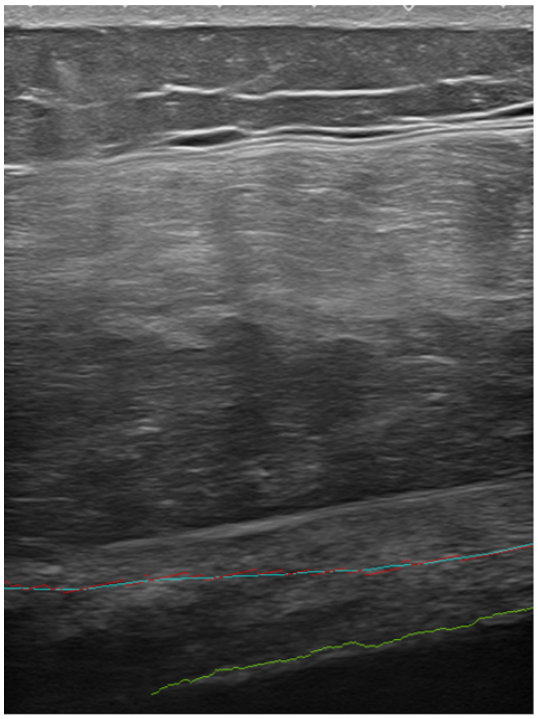

Figure D.9: Measurement 7

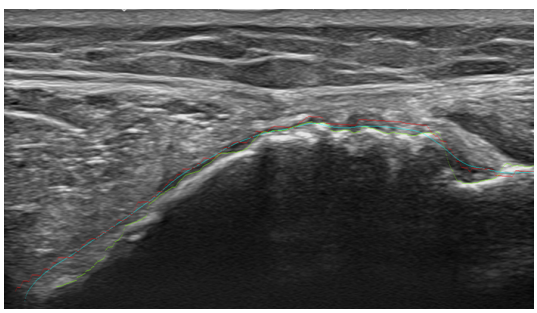

Figure D.10: Measurement 8

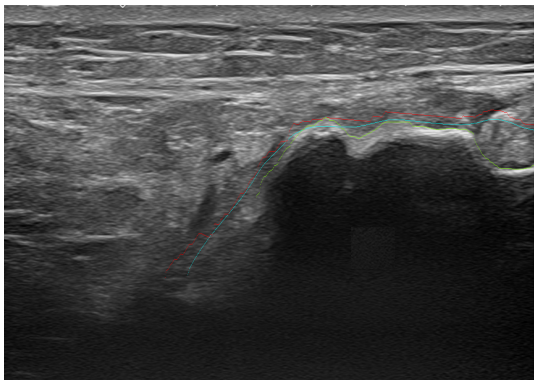

Figure D.11: Measurement 9

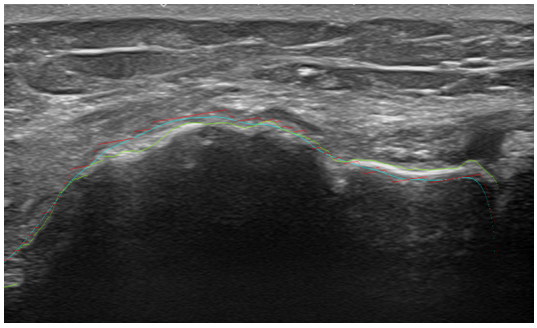

Figure D.12: Measurement 10

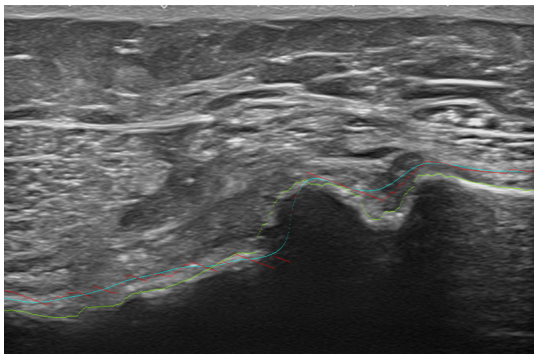

Figure D.13: Measurement 11